Annual Report for

Contract DE-FG36-08GO18192

Stanford Geothermal Program

September 2009 – September 2010

Table of Contents

1. FRACTURE CHARACTERIZATION USING PRODUCTION DATA

This research project is being conducted by Research Assistant Egill Juliusson, Senior Research Engineer Kewen Li and Professor Roland Horne. The objective of this project is to investigate ways to characterize fractures in geothermal reservoirs using production data.

1.1 SUMMARY

A summary of progress made in this project since September 2009 is presented in this report. The discussion is divided into three main sections.

First, we review a study using a finite-volume reservoir simulator, with discrete fracture meshing, to model combined fluid, solute and heat transport. This study provided us with insights into many important features governing the transport of each of these signals. The study also helped to develop better understanding of the challenges involved in this type of modeling.

The challenges encountered in finite-volume fracture simulation lead to the development of a semianalytical modeling technique for simulating pressure and tracer transport through a fracture network. The novelty of this method is that it can be used to model tracer transport through fracture networks with virtually no numerical dispersion. It represents an alternative to the particle tracking method, which is also free of numerical dispersion, but requires much computational power if smooth tracer return curves are to be computed for scenarios with continuous tracer injection.

The third section is on the implementation of a parametric method that could be used for multiwell deconvolution of tracer test data. The method was developed as an alternative to the nonparametric deconvolution methods presented in the quarterly report from summer 2009. Deconvolving such signals reveals the transfer function between each well pair. This transfer function is representative of the pore volume of the fracture paths between the wells, and the dispersivity induced by flowing through those paths.

1.2 INTRODUCTION

The main thought behind this research project has been to enhance current understanding of how field production data can be utilized to characterize fractured reservoirs. Data from geothermal fields indicates that flow is usually highly fracture dominated and that provided the motivation for this work. Examples of production data that are often measured are flow rates, pressure, temperature, enthalpy and tracer.

A number of previous studies have proposed that tracer breakthrough curves could be used to predict thermal breakthrough in fractured reservoirs. The topic was discussed e.g. by Bodvarsson and Pruess (1984), Urbino and Horne (1991), Sullera and Horne (2001) and Horne and Szucs (2007). This idea becomes particularly interesting with regards to optimization of reinjection scheduling, as discussed by Lovekin and Horne (1989). However, the tracer testing approach has some limitations because the returns from a tracer

test will vary with changes in the reinjection schedule. Moreover, Pruess and Bodvarsson (1984) showed that in vertically fractured reservoirs the tracer signal will not suffice to fully characterize the thermal characteristics of the flow path. They state that the flow path characteristics can be determined more accurately using a mixed numerical/semianalytical approach with the combined interpretation of pressure, temperature and tracer. These analyses show that understanding the combined transport of pressure, tracer and heat in fractured reservoirs is an essential but nontrivial task.

Numerical simulation of tracer transport in fractured reservoirs is also a particularly challenging problem. One reason is that for the most commonly used discretization schemes the computations will be adversely affected if a saturation front is allowed to travel more than one gridblock per time step. This obviously causes problems in models with saturations travelling fast through the extremely small gridblocks that represent the fractures. Intriguing advances have been made to solve this problem (partially), e.g. by Lange et al. (2005) and Wu et al. (2000, 2008), using flux-limiter methods. Finite-volume simulators that have these methods implemented and are equipped to handle fully unstructured grids are not available commercially, to the best of our knowledge.

The finite-volume simulation discussed here utilized the method of Karimi-Fard et al. (2003) to discretize the permeability on an unstructured two-dimensional grid. This way the transport physics in the fracture network are captured more accurately, especially in sparsely fractured rock such as might be encountered in Enhanced Geothermal Systems (EGS). This simulation method is also interesting because it allows clear visualization of the propagation of the simulated properties (pressure, temperature, tracer saturation etc.) in time. However, with more densely fractured rock, this method quickly becomes infeasible because of the lack in computational efficiency. In such cases, an upscaling method could provide a practical alternative (see e.g. Gong, 2007).

The downside of this fully-fledged simulation method was that, the rapid movement of the tracer front in the fractures caused the simulations to be very computational inefficient and numerical dispersion was large and hard to quantify accurately. Based on some of our subsequent experience with the flux-limiter methods, these would most likely also cause problems, which hinder realistic simulation of dispersion. This makes it difficult to use finite-volume simulations to understand the details of tracer transport through fractured reservoirs.

Tracer transport can be modeled using analytical solutions to the advection-dispersion equation. This was utilized to build a fast but simplified numerical modeling method for calculating flow through a discrete fracture network. So far the model has been developed based on the assumption of steady-state, incompressible single-phase flow, which made the flow problem analogous to analyzing a network of resistors. The single-phase incompressibility assumption should be a relatively good approximation for most EGS (Enhanced Geothermal Systems) and other single-phase geothermal systems.

The basic way the method works is to take an arbitrary network of fractures and break it into a set of nodes (fracture intersections) and edges (fracture segments) that connect the

nodes. The net inflow into each node is then used to set up a system of equations that describe the flow in the entire network. The system of equations can then be solved to find the flow rate in each fracture segment. Analytical solutions of the advection-dispersion equation are then used to propagate the tracer profiles along each path. At this point, some relatively efficient graph algorithms are employed to find all paths connecting any two wells. The travel time and flow rate attributable to each path can also be found, which means essentially that dispersion free tracer transport through the network has been computed. Being able to solve this problem without any numerical dispersion effects brought us a step closer to characterizing the effects of fracture networks on production data.

We illustrate how the effects of Taylor dispersion (molecular diffusion within each fracture) can be added to the computations. Our approach is based on successive convolutions of the one-dimensional advection-dispersion equation in Laplace space. Special attention is given to the time discretization in the convolution approach and selection of a numerical algorithm for the inverse Laplace transformation. The results indicate that Taylor dispersion can influence the tracer returns dramatically, and mask much of the dispersion caused by the variation of flow paths through the fracture network.

The third main section of the report complements a number of approaches developed earlier in this project for revealing well-to-well connectivity using tracer data. We present a parametric model based on a solution to the one-dimensional advection-dispersion equation, for a unit impulse injection of tracer, but that solution could easily be replaced by any other function.

1.3 FINITE-VOLUME DISCRETE FRACTURE MODELING

This section describes how the reservoir simulations were set up to simulate flow through a fractured medium.

The first step in setting up the model was to generate a fracture network. A number of software packages are available for creating these, e.g. FRACMAN from Golder and Associates and FRACA from Beicip-Franlab. However, in order to keep the study simple, a two-dimensional network was created in MATLAB with a code loosely based on the geomechanical process of fracture formation. Further discussion of the code can be found in the quarterly report for summer 2009.

After the fracture network had been generated, a suitable computational grid had to be formed. This was accomplished using the open-source mesh generator Triangle (Shewchuk, 1996). The program and all associated commands and files were well described on the Triangle website, http://www.cs.cmu.edu/~quake/triangle.html. Figure 1.1 shows a stochastic fracture network with a conforming triangular grid.

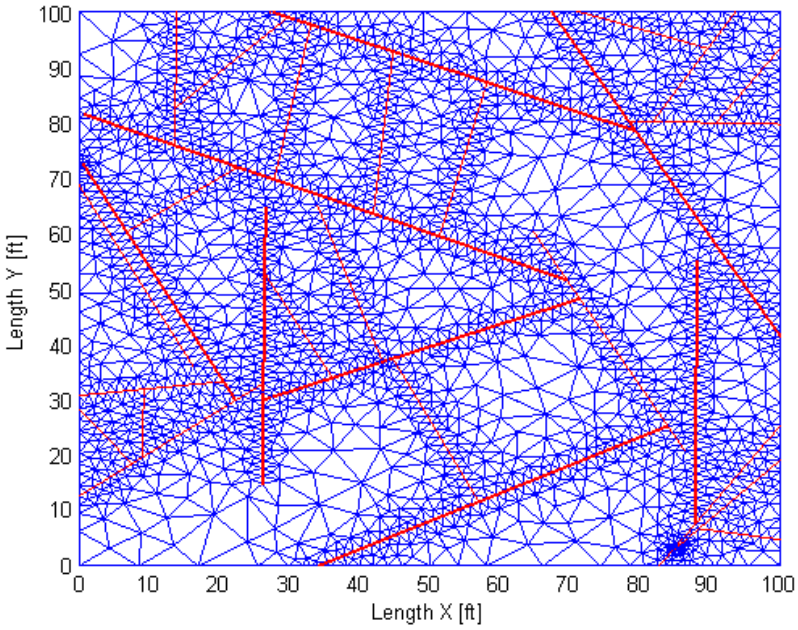

Figure 1.1: An example of a synthetic fracture network (red) and a mesh (blue) that conforms to the fractures. The width of the red lines is indicative of the width assigned to the fracture elements.

One of the major issues involved in modeling fractures explicitly in reservoir simulators relates to the intersection of the fractures. Handling this intersection in the "usual" manner leads to very small gridblocks (Figure 1.2) which can adversely affect the numerical stability and computational efficiency of the simulation.

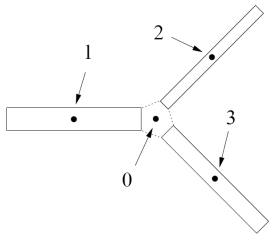

Figure 1.2: A very small gridblock (labeled 0) is formed at the intersection of fractures, on a computational grid where fractures are modeled discretely. Figure taken from Karimi-Fard et al. (2003).

By using the discretization scheme introduced by Karimi-Fard et al. (2003) the small gridblocks formed at fracture intersections were eliminated. The key element in their approach was to apply the star-delta transformation, which is more commonly used to solve problems in electrical engineering (Figure 1.3).

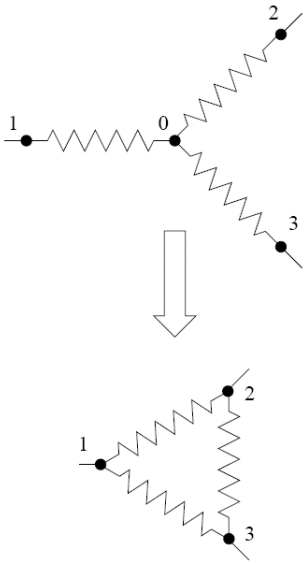

Figure 1.3: Intersections of multiple fractures can be converted to simpler connections using the star-delta transformation. Figure taken from Karimi-Fard et al. (2003).

From the star-delta transformation transmissibility between each connecting fracture element could be computed, using the formulation:

$$T_{ij} = \frac{\alpha_i \alpha_j}{\sum_{k=1}^{n} \alpha_k} \tag{2.1}$$

where:

$$\alpha_i = \frac{A_i k_i}{D_i} \tag{2.2}$$

and k denotes permeability, A is the cross sectional area at the fracture intersection and D is the distance from the centroid of the fracture block to the center of the fracture intersection.

Each fracture was assigned a width, w, and the corresponding permeability was determined by:

$$k = \frac{w^2}{24} \tag{2.3}$$

For single-phase flow, the transmissibility values are related to the flow between two adjoining elements, i and j, by:

$$Q_{ij} = \frac{T_{ij}}{\mu_{ij}}(p_j - p_i) \tag{2.4}$$

where Q is the flow rate, T is the transmissibility, μ is dynamic viscosity and p is the pressure in the corresponding gridblock.

Our initial plan was to use the TOUGH2 code to carry out the required simulation work. However, TOUGH2 was not equipped to handle transmissibility terms as input data for individual connections. To account for that, the TOUGH2 code was modified such that it could take permeability values as input through the connection list (CONNE). To be exact, the last column of the connection list (which is meant to contain data for radiative heat transfer, SIGX) was used as the input column for connection-wise permeability values. These permeability values were calculated using the transmissibility formulation given by equation (1.1), and then dividing by a similar number but calculated with $k = 1$, i.e.:

$$k_{ij} = \frac{\alpha_i \alpha_j}{\sum_{k=1}^{n} \alpha_k} \Bigg/ \frac{\beta_i \beta_j}{\sum_{k=1}^{n} \beta_k} \tag{2.5}$$

where:

$$\beta_i = \frac{A_i}{D_i} \tag{2.6}$$

Then the values D and A could be supplied in the usual way through the connection list and the transmissibility was recalculated internally in TOUGH2. Note that the permeability values supplied in the ROCKS section and/or ELEME section of the TOUGH2 input file were all set to one, such that they would not interfere with the values supplied through the connection list (CONNE).

The modified version of TOUGH2 seemed to work well, in the sense that it yielded physically realistic output for the tracer returns. However, we ran into trouble when running the code for longer simulation times which would be required to observe thermal breakthrough times. We believe that the problem was related to the time stepping algorithm and/or simply the fact that the set of equations involved were too hard to solve for the solvers used by TOUGH2.

As an alternative it was decided to use the Stanford General Purpose Reservoir Simulator (GPRS) (Cao, 2002; Voskov, 2006). All simulations with GPRS were run using the black-oil thermal module, where water was injected into a fully "oil" saturated reservoir, where the "oil" phase had all the equivalent properties of water. Capillary pressure was set to zero and X-curve relative permeability was used such that the two phases would interact as if there was only one phase. The pressure and temperature were set such that the reservoir fluid always remained as single-phase liquid.

1.3.1 Governing Equations

Before looking into simulations of specific fracture formations it was useful to review the governing equations of mass and energy rates for a unit volume, and see how much could be understood from employing some simplifying assumptions.

For single-phase flow of κ components the mass equation could be written as (see notation in Table 1.1):

$$\frac{\partial}{\partial t}(\varphi\rho^{\kappa}X^{\kappa}) = -\nabla\left(\frac{k\rho^{\kappa}\nabla p}{\mu^{\kappa}}X^{\kappa} + \varphi\rho^{\kappa}d_{mol}^{\kappa}\nabla X^{\kappa}\right) + q^{\kappa} \tag{2.7}$$

The energy equation was formulated as:

$$\frac{\partial}{\partial t}\left(\varphi\rho^{\kappa}X^{\kappa}u^{\kappa} + (1-\varphi)\rho_{R}u_{R}\right) = -\nabla\left(\frac{k\rho^{\kappa}\nabla p}{\mu^{\kappa}}X^{\kappa}h^{\kappa} + \lambda\nabla T\right) + w^{\kappa} \tag{2.8}$$

Table 1.1: Notation used for governing equations.

φ	Porosity
ρ	Density (kg/m3)
X	Mass fraction of component
κ	Superscript that denotes component (water or tracer)
t	Time (sec)
k	Absolute permeability (m2)
p	Pressure (Pa)
μ	Dynamic viscosity (Pa-s)
d	Molecular diffusion coefficient (m2/s)
q	Mass source/sink (kg/s-m3)
u	Specific internal energy (J/kg)
R	Subscript that denotes rock
T	Temperature (C)
h	Specific enthalpy (J/kg)
λ	Thermal conductivity (W/m-C)
w	Energy source/sink (W/m3)
y	Distance (m)
c	Specific heat capacity (J/kg-C)
V	Subscript referring to volume

In most of the cases we considered the matrix permeability was much smaller than that of the fracture, and therefore the derivative along the fracture (here y direction) would dominate. Given that molecular diffusion is on the order of 10^{-10} for liquid tracers, we assumed that this could be discarded. For the temperature/pressure range observed, the density changes could be considered negligible over incremental distances in time and space. Therefore the mass balance equation could practically be reduced to:

$$\varphi \frac{\partial}{\partial t}(X^\kappa) = -\frac{d}{dy}\left(\frac{kX^\kappa}{\mu^\kappa}\frac{dp}{dy}\right) + \frac{q^\kappa}{\rho^\kappa} \tag{2.9}$$

To further simplify the energy equation, the enthalpy and internal energy were written in terms of specific heat capacities, and these were assumed not to change much incrementally. This gave:

$$\varphi \frac{\partial}{\partial t}\left(X^\kappa T + \frac{(1-\varphi)\rho_R c_R}{\varphi \rho^\kappa c_V^\kappa} T\right) = -\frac{d}{dy}\left(\frac{kX^\kappa c_p^\kappa T}{\mu^\kappa c_V^\kappa}\frac{dp}{dy}\right) - \frac{\lambda}{\rho^\kappa c_V^\kappa}\nabla^2 T + \frac{w^\kappa}{\rho^\kappa} \tag{2.10}$$

The thermal diffusion coefficient, $\lambda / c_V^\kappa \rho^\kappa$, was on the order of 10^{-3} m^2/s. Also the quantity:

$$v = -\frac{k}{\mu}\frac{dp}{dy} \tag{2.11}$$

is the Darcy velocity. In many of the single fracture studies this velocity remained approximately constant (at around 10^{-3} m/s). Therefore Equations (2.9) and (2.10) would further simplify to:

$$\varphi \frac{\partial}{\partial t}(X^\kappa) = v\frac{d}{dy}\left(X^\kappa\right) + \frac{q^\kappa}{\rho^\kappa} \tag{2.12}$$

and

$$\varphi \frac{\partial}{\partial t}\left(X^\kappa T + \frac{(1-\varphi)\rho_R c_R}{\varphi \rho^\kappa c_V^\kappa} T\right) = -v\frac{d}{dy}\left(\frac{c_p^\kappa}{c_V^\kappa} X^\kappa T\right) - \frac{\lambda}{\rho^\kappa c_V^\kappa}\nabla^2 T + \frac{w^\kappa}{\rho^\kappa} \tag{2.13}$$

The flow velocity was generally on the order of 10^{-3} m/s and the ratio of specific heat capacities was close to one. Finally, assuming that the density and heat capacities do not change much with time, and that $X^\kappa \approx 1$, leads to:

$$\varphi R \frac{\partial T}{\partial t} = -v\frac{c_p^\kappa}{c_v^\kappa}\frac{\partial T}{\partial y} + \frac{\lambda}{\rho^\kappa c_V^\kappa}\nabla^2 T + \frac{w^\kappa}{\rho^\kappa} \tag{2.14}$$

where R is a retardation factor:

$$R = 1 + \frac{(1-\varphi)\rho_R c_R}{\varphi \rho^\kappa c^\kappa} \tag{2.15}$$

From this we see that the solute transport would travel almost only by convection if it were not for hydraulic dispersion induced fractures and velocity profiles within the fractures (Taylor dispersion).

The simple analysis of the thermal transport shows that diffusion along the fracture should not be ignored, nor should the retardation caused by interaction with the surrounding rock.

1.3.2 Simulation Results

A number of studies were performed with a single finely gridded fracture going through a matrix block (Figure 1.4). The effects of varying fracture aperture, flow velocity, distance to the boundary and several other parameters were investigated. These observations suggested that the thermal return curves were highly dependent on the flow rate through the fracture and the distance to the matrix boundary. A more detailed recount of these studies is in Juliusson and Horne (2010).

The high sensitivity to the distance to the matrix boundary, which could be understood as the fracture density, motivated the next experiment. The experiment involved two cases with multiple fractures, one with a sparsely fractured reservoir and another where a large number of smaller fractures had been added. The fracture apertures were linearly related to the fracture lengths, such that they spanned a range of about 0.1 to 10 mm. The size of the reservoir was also set to 100x100x100 meters and the matrix was given permeability 1 md. The injection rate was fixed at 10 kg/s. The sparse and dense fracture networks (with around 40 and 300 fractures, respectively) are shown in Figure 1.5.

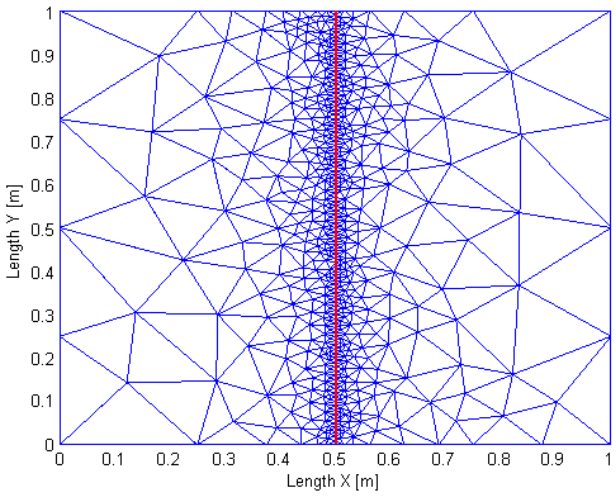

Figure 1.4: Computational grid for a single fracture, broken lengthwise into 100 segments.

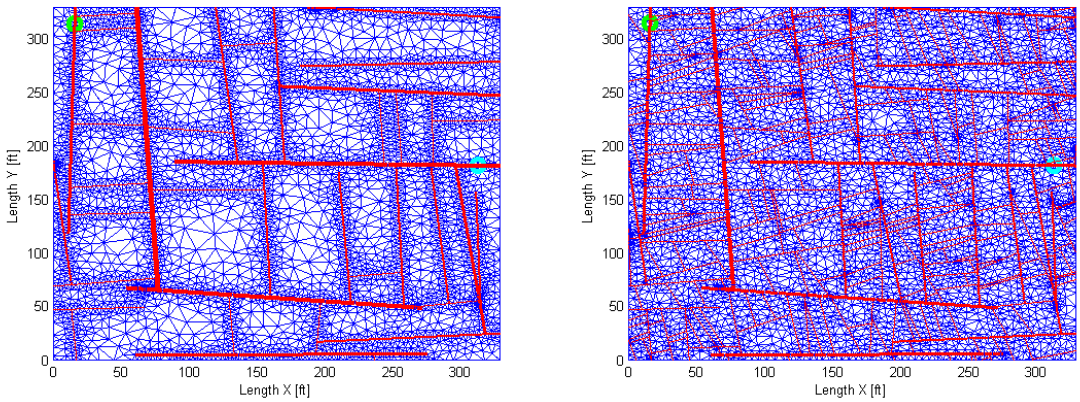

Figure 1.5: Sparse network of 40 fractures (above) and dense network of 300 fractures (below). The injector and producer are denoted by green and cyan circles, respectively. The width of the fracture lines (red) is indicative of the aperture.

1.3.2.1 Spatial Property Propagation

The propagation of pressure, temperature and tracer could be visualized and compared for the two cases. The following figures are snapshots of these property distributions after 12 hours of injection.

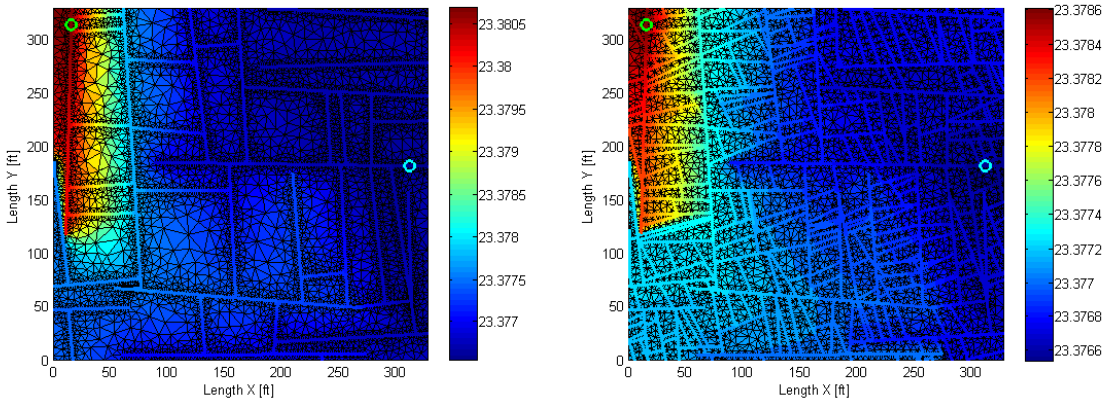

Figure 1.6: Pressure distribution after 12 hours of injection for the two fracture networks studied.

As Figure 1.6 shows, the pressure propagated in a diffusive nature as expected due to the elliptical character of the pressure equation. The pressure gradient spread considerably into the matrix in both cases, but in the denser network the pressure change spread further into the reservoir.

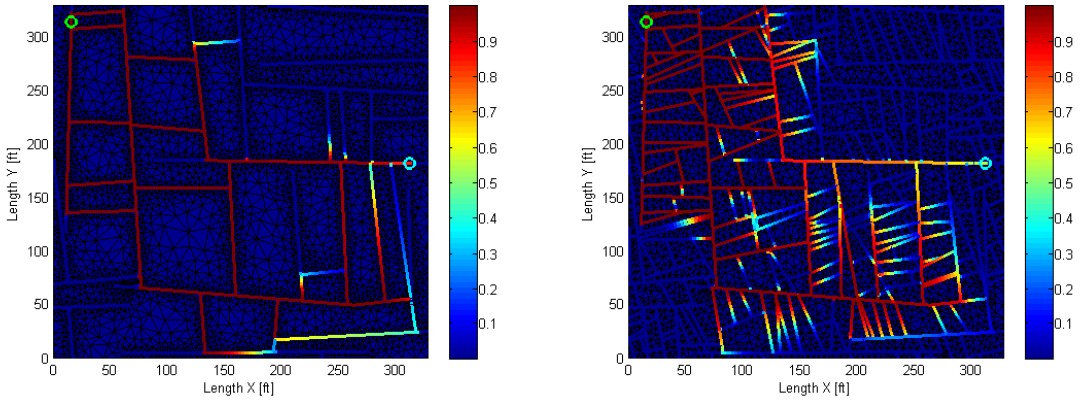

Figure 1.7: Tracer distribution after 12 hours of injection for the two fracture networks studied.

The tracer distribution in the reservoir is shown in Figure 1.7. The tracer propagation was dominated by convection (in fact diffusion effects were not modeled so the dispersion seen in the fractures is all numerical) and therefore the tracer flowed almost exclusively through the fractures. The flow through the denser network is clearly much more dispersive, which indicates that more effective heat extraction would be achieved.

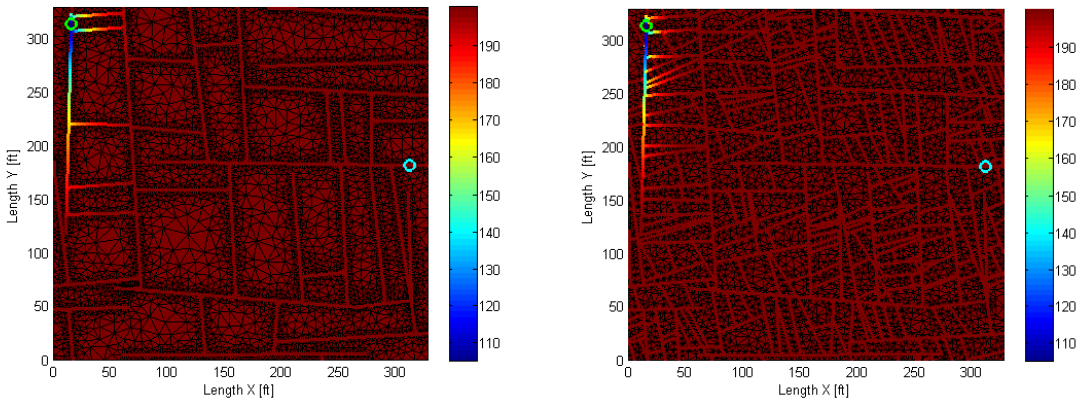

Figure 1.8: Thermal distribution after 12 hours of injection for the two fracture networks studied.

Figure 1.8 illustrates the temperature distribution after 12 hours of injection. At this time the thermal front seemed to be traveling mostly through the fractures. However, the front would not propagate much unless the surrounding matrix blocks had started cooling. This retardation effect is perhaps better seen in Figure 1.9 which shows the thermal distribution after 280 days. This illustrates well how the thermal front traveled in a mixed convective/diffusive manner.

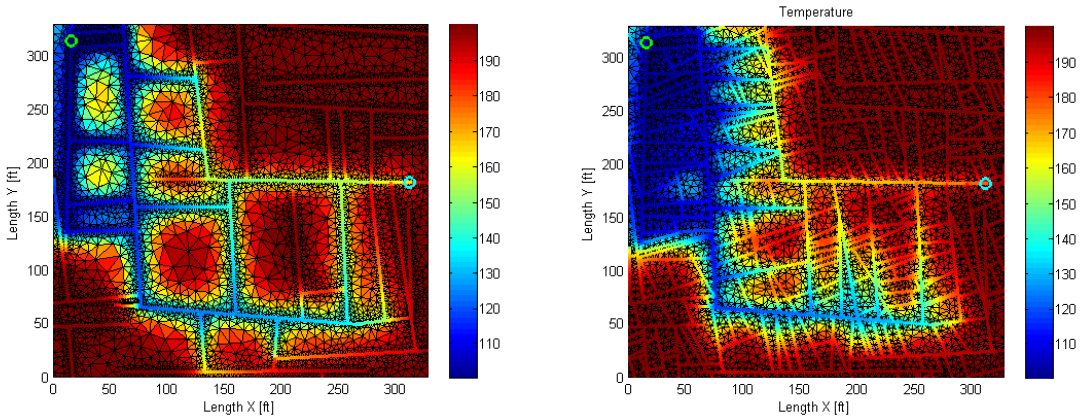

Figure 1.9: Thermal distribution after approx. 280 days of injection for the two fracture networks studied.

1.3.2.2 Return Profile Comparison

The main characteristics of the return profiles for the two simulation scenarios, i.e. mean travel time and dispersion, were computed. The results are summarized in Table 1.2.

Table 1.2: Characteristics of return profiles for the two simulation cases studied. Time is in days, dispersion is in m^2/sec

	$\bar{t}_{tr}$	D_{tr}	$\bar{t}_T$	D_T
Sparse	0.30	$4.8\text{x}10^{-2}$	425	$3.1\text{x}10^{-4}$
Dense	0.47	$6.1\text{x}10^{-2}$	546	$1.0\text{x}10^{-4}$

The denser network gave a longer mean return time for both the tracer and temperature. However the change in the dispersion coefficient was small, and for the temperature the dispersion coefficient was lower in the dense fracture network case. For the tracer this indicated that the density of the fracture network did not have as much effect on the dispersion coefficient as did numerical dispersion (or physically, Taylor dispersion, which would be similar in magnitude to the numerical dispersion). The fact that the thermal dispersion coefficient was smaller for the dense fracture network indicated that a more uniform front swept the reservoir.

The corresponding return curves from each of the simulation cases were compared on a quantile plot. This plot compares the times at which a certain quantile of the injection value is obtained on the production side. In Figure 1.10 the quantiles for the tracer return curves are compared. The fact that the quantile values all fell on the left of the 45 degree line meant that the tracer return time tended to be larger for the dense fracture case, and this difference got larger at later times.

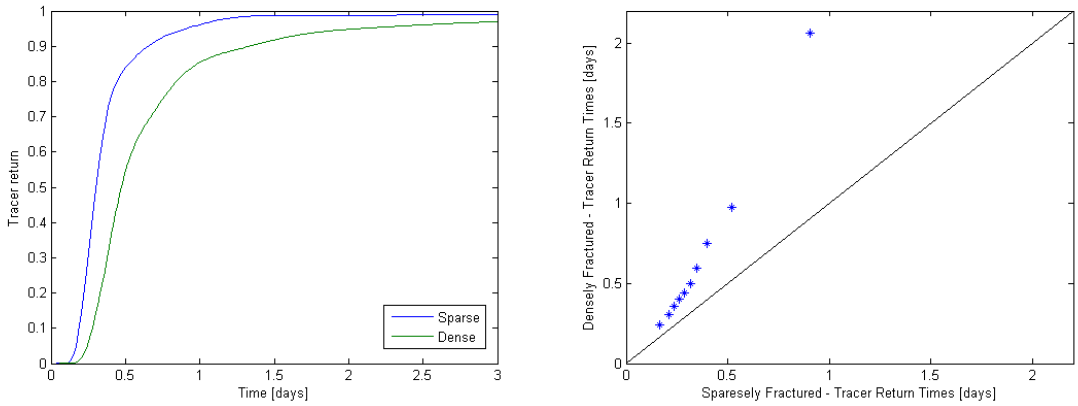

Figure 1.10: Comparison of the tracer return profiles for the sparse and dense fracture networks. The graph on the left is the return profile. The graph on the right is a quantile plot comparing the two return distributions.

Figure 1.11 compares the two temperature return curves. These two return curves were clearly much more similar which was well conveyed on the quantile plot. For the dense fracture case the initial return quantiles were larger than those for the sparse case, but at later times the trend reversed. This pointed to a better thermal sweep in the dense fracture case. In other words, residual thermal energy was being swept from the reservoir for a slightly longer time in the sparse fracture case, and the bulk of the cooling came earlier.

As a final note of interest we mention that the tracer return profiles showed some "large scale" changes in the slope (Figure 1.10), which we believed to be strongly related to the fracture distribution. The thermal return showed more smooth variations (Figure 1.11) because of the strong interaction with the matrix blocks.

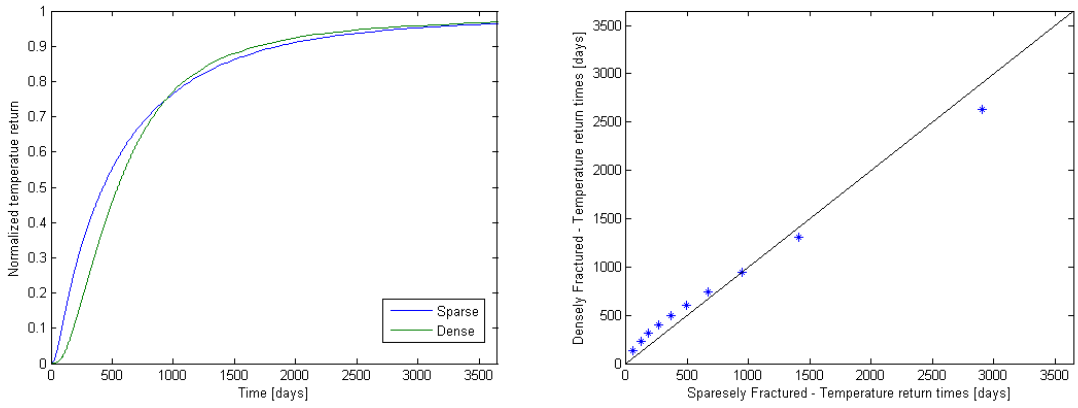

Figure 1.11: Comparison of the normalized temperature return profiles for the sparse and dense fracture networks. The graph above is the derivative of the return profile. The graph below is a quantile plot comparing the two return distributions.

1.4 SEMIANALYTICAL DISCRETE FRACTURE NETWORK MODEL

In this section the development of a simplified method for characterizing fracture networks is described. The workflow roughly involved creating a stochastic fracture network, simplifying that network into a set of connected nodes (fracture intersections) and edges (fracture segments), and computing the flow, travel time, transmissibility, etc., in each fracture segment. Finally the total travel time, effective transmissibility, effective flow rate and tracer return profile along every path was computed.

1.4.1 Setting up the network graph

The first step in setting up the model was to generate a fracture network (Figure 1.12). Each fracture was given a constant height (H), aperture (b) and permeability (k). In this particular instance the height was assumed to be constant but the aperture was assumed to be proportional to the fracture length and the permeability was assumed to be proportional to the square of the aperture (Takahashi et al. 1995; Watanabe and Takahashi 1995).

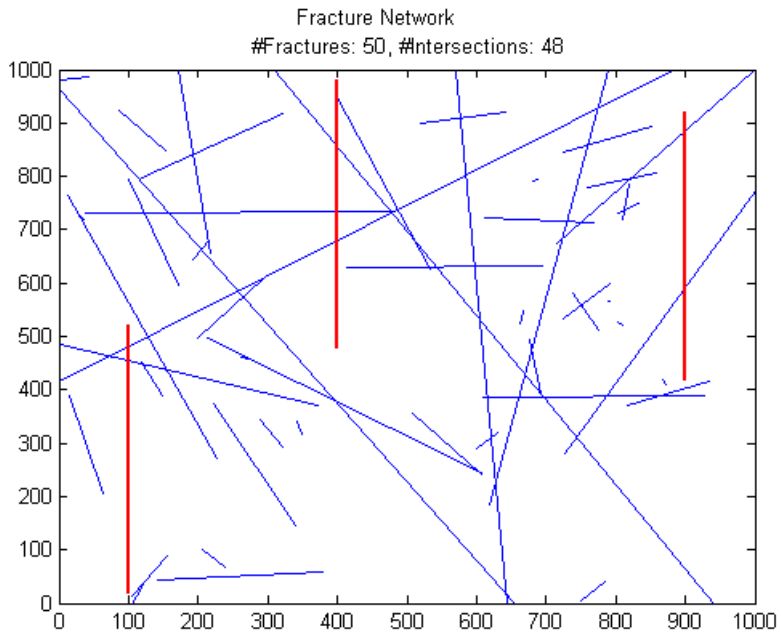

Figure 1.12: A two-dimensional stochastic fracture network with three wells. The fractures are the blue lines and the wells are the thicker red lines.

The first step with the simplified method was to find the flow rate in each path connecting any of the two wells and then to compute the time it would take to travel along each path. Note that two paths were defined as different if (and only if) they traversed one or more different fracture segments (edges) from point *a* to point *b*. Figure 1.12 illustrates clearly that some fractures did not connect any of the wells and could therefore be eliminated from further analysis. This cleanup process was performed using a recursive graph traversal algorithm (depth first search). The standard way in which it was implemented is not optimal in terms of memory allocation, which limited the number of fractures that could be handled. Some improvement will be required at later stages; however, the algorithm

worked quite well for a modest number of fractures (say 50). The results of the clean up process are illustrated in Figure 1.13.

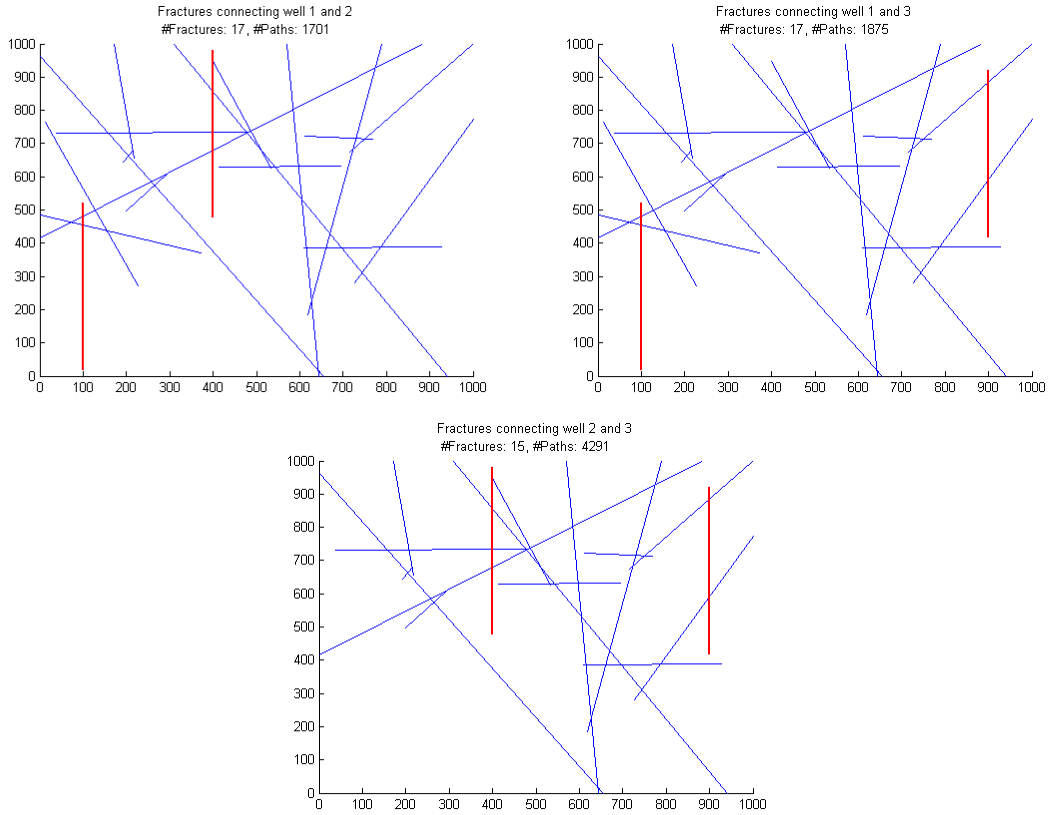

Figure 1.13: Remaining fractures on paths connecting each pair of wells. At this stage, all paths are assumed to be undirected, i.e. flow could go either way along each fracture segment.

Now each of the remaining fractures was broken into fracture segments (edges) and fracture intersections (nodes). An edge was only created for those fracture segments which would be on a path from one well to the other, so all fracture end segments were removed (Figure 1.14). Each fracture segment was given the same height, aperture and permeability as the corresponding fracture had. The length (L) was determined by the segment length. Then the segment transmissibility (T) was calculated as:

$$T = \frac{kbH}{\mu L} \tag{2.16}$$

Here μ represents the dynamic viscosity of the fluid which was assumed to be constant at 10^{-3} Pa-s. The viscosity is generally not included in the transmissibility but it was included in this case just to simplify the equations a bit.

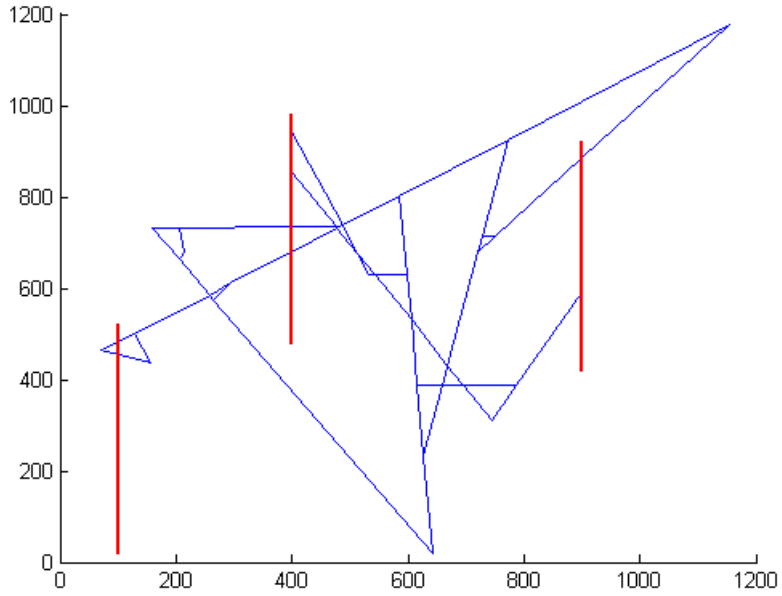

Figure 1.14: All fracture segments on connecting paths between well pairs.

1.4.2 Computing flow directions in the fracture network

After each of the nodes and edges had been defined the fracture system could be viewed as a resistor network and solved via nodal analysis. That is, given the assumption of incompressible, single-phase flow the net amount of flow into each node should sum up to zero. This led to a set of equations which could be set up in the following matrix form,

$$Jp = r \tag{2.17}.$$

The elements of the matrix J were defined as:

$$J_{ij} = \begin{cases} \sum_k T_k & \text{if} \quad i = j \text{ and edge } k \text{ connects to node } i \\ T_k & \text{if} \quad i \neq j \text{ and edge } k \text{ connects nodes } i \text{ and } j \\ 0 & \text{otherwise} \end{cases} \tag{2.18}$$

The vector p denoted the unknown nodal pressures and the right hand side vector was:

$$r_i = \begin{cases} \sum_k T_k p_j & \text{if edge } k \text{ connects node } i \text{ and known pressure node } j \\ 0 & \text{otherwise} \end{cases} \tag{2.19}$$

The know pressure nodes referred to in Equation (1.19) would be the (measured) pressure nodes where the fracture intersects the well.

Having solved for the pressure, the flow directions in each segment were computed as:

$$q_k = T_k(p_i - p_j) \qquad (2.20),$$

where it is implied that fracture segment k connects nodes i and j. The flow velocity and travel time along each segment could also be calculated based on the area and length of the fracture segment. Figure 1.15 shows the flow direction computed along each of the fracture segments given a set of pressures in each well.

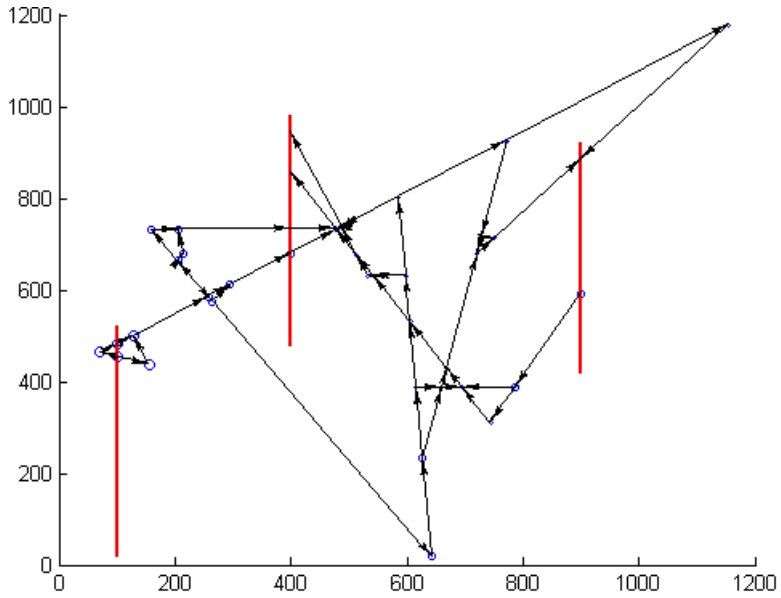

Figure 1.15: All directed paths in the fracture network for a given set of pressures in the wells. The black arrows show the flow direction. The sizes of the blue circles at each node represent the pressure.

Clearly, the flow patterns can become very complex. For example the fluid can move in opposite directions in the same fracture, and some paths will start and end in the same well. Table 1.3 summarizes the number of paths connecting each well pair for the particular case illustrated in Figure 1.15.

Table 1.3: A summary of the number of paths connecting well pairs. The well numbers from 1 to 3 correspond to the order in which they are located in Figure 1.15, from left to right.

End well / Start well	Well 1	Well 2	Well 3
Well 1	1	309	57
Well 2	0	2	0
Well 3	0	38	8

1.4.3 Path properties

To further characterize the fracture network, a number of path dependent properties were computed. Aside from the path length, the path travel time was perhaps the simplest to compute. Once the travel time in each fracture segment had been found, the total travel time along each path K, was computed as the sum of the travel times along each segment;

$$t_K = \sum_k^N t_k \tag{2.21}$$

where k runs over each of the segments on path K.

The effective flow rate along each path, in other words the flow rate attributable to each path connecting two points, was also of interest. The seemingly most straight forward way of computing this quantity was to propagate the proportion of flow going along each path as a weighted average of the flow exiting each node. The example network shown in Figure 1.16 will be used to illustrate this.

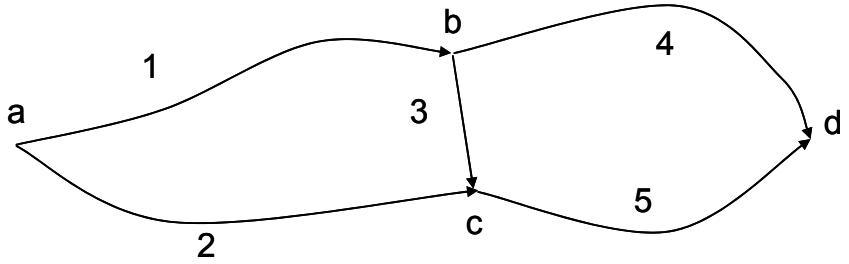

Figure 1.16: Fracture network used for an illustrative example. Nodes are labeled as a-d and edges 1-5. Arrows denote flow direction.

The flow rate in each segment was found from Equation (1.20) (as shown by arrows). Three different paths lead from *a* to *d*, i.e. {1,4}, {1,3,5} and {2,5}. At each node the stream is separated into one or more substreams, thus the flow rate (q) along each path could be computed as

$$\begin{aligned}
q_{14} &= q_{tot}\frac{q_1}{q_1+q_2}\frac{q_4}{q_3+q_4} && \text{arrives at} \quad t_1+t_4 \\
q_{135} &= q_{tot}\frac{q_1}{q_1+q_2}\frac{q_3}{q_3+q_4}\frac{q_5}{q_5} && \text{arrives at} \quad t_1+t_3+t_5 \\
q_{25} &= q_{tot}\frac{q_2}{q_1+q_2}\frac{q_5}{q_5} && \text{arrives at} \quad t_2+t_5
\end{aligned} \tag{2.22}$$

Note that the sum of the three path streams equals $q_{tot}=q_1+q_2$. The general formulation is that the flow rate along each path, K, is:

$$q_K = q_{tot} \prod_k \frac{q_k}{\sum_l q_l} \tag{2.23}$$

where k runs over all edges on path K, and l runs over all edges with outflow from the node which edge k has flow out of.

The effective transmissibility of each path, specific to the computed flow field, was computed as:

$$T_K^* = \frac{q_K}{p_i - p_f} \tag{2.24}$$

where the subscripts i and f refer to the pressure at the initial and final node on path K.

Continuing the example shown in Figure 1.16 we could find each of the fastest, most transmissible and largest flow paths connecting any well pair. These are shown in Figure 1.17 along with each of the paths connecting well 1 to well 2, well 1 to well 3 and well 3 to well 2. Note that there were no connections in the reverse direction (e.g. from well 2 to well 1). Also, as noted in Table 1.3, each of the wells had a few paths leading back into the well itself.

A stem plot of the flow rate versus the arrival time along each path connecting wells 1 and 3 is shown in Figure 1.18. The figure also contains the cumulative flow rate vs. arrival time. The two plots are analogous to the impulse and step response to tracer injection if no molecular diffusion or numerical dispersion were present. It is quite interesting to see that although there are over 50 paths connecting the two wells, only three of them carry any significant portion of the flow, and the travel times for these larger paths are relatively dispersed.

A correspondence between large flow rates and small travel times was more commonly observed as was the case for flow from well 1 to well 2 (Figure 1.19) and from well 3 to well 2 (Figure 1.20). Notice also from the absolute values of the flow rates computed for each case, that by far the largest flow connection was between wells 1 and 2; this connection was attributable to a single large fracture connecting the two wells.

1.4.4 Taylor dispersion by successive convolution

The molecular dispersion of tracer along the flow paths was implemented and reported in the quarterly report from spring 2010. The implementation was explained using the fracture network shown in Figure 1.21, thus we will use that example here as an alternative to continuing with the example shown in Figure 1.12.

The pressure in the two wells to the left (the injectors) was set to 200 bar while the right most wells (the producers) had a constant pressure of 198 bar. The network was then simplified and the flow through it was computed via nodal analysis. The flow directions are shown in Figure 1.22.

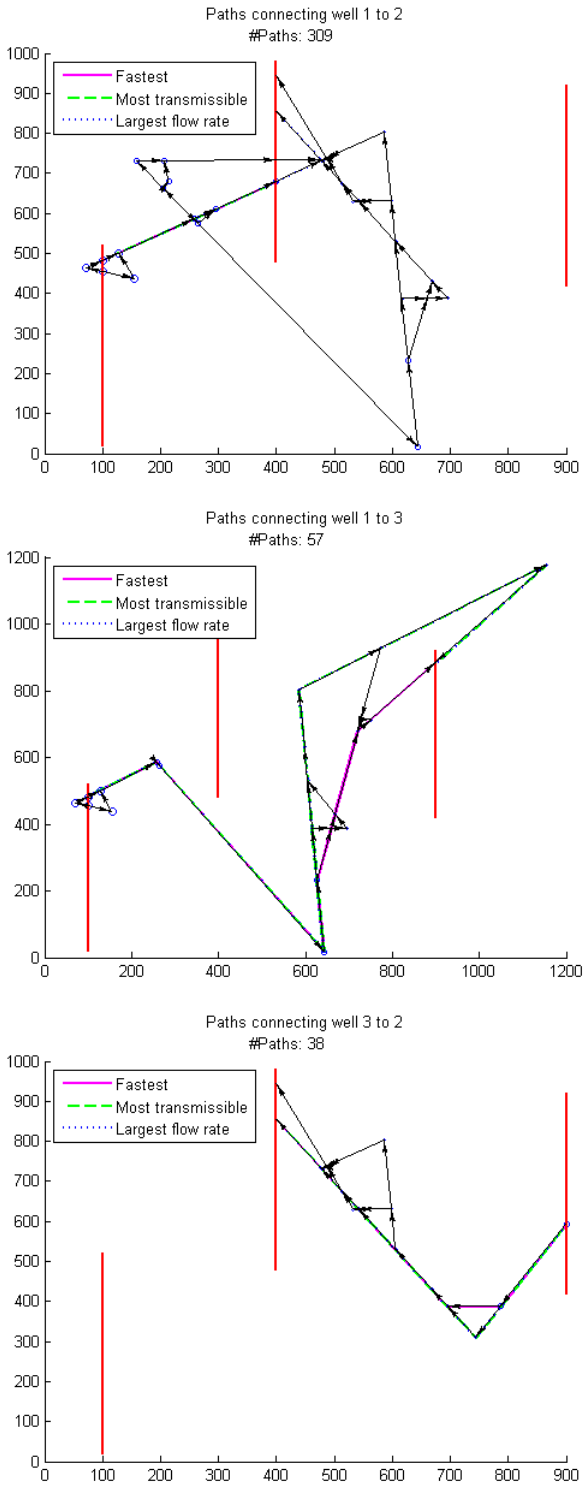

Figure 1.17: The ensemble of connecting paths for a few well pairs. Note that the fastest path, the most transmissible path and the path which carries the most flow are not necessarily the same.

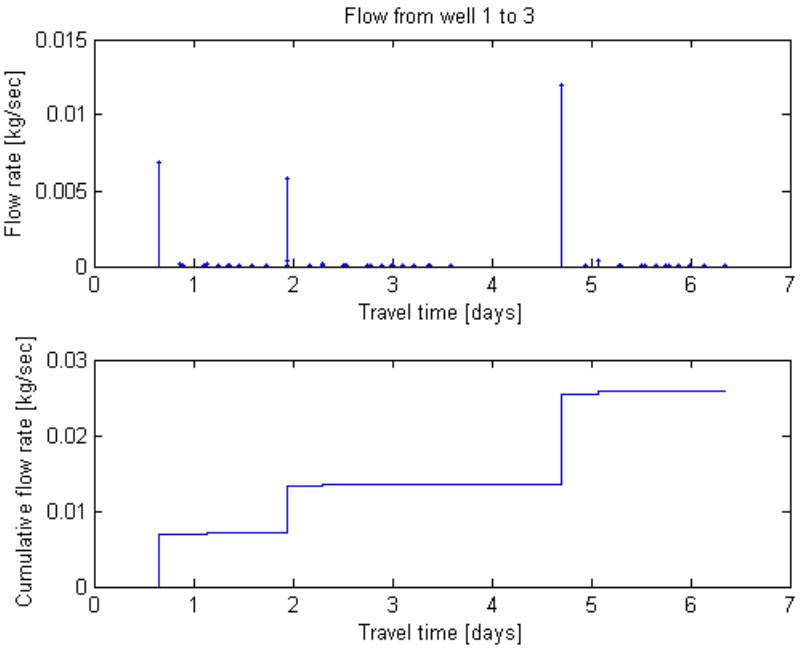

Figure 1.18: Flow rate vs. Travel time and Cumulative flow rate vs. Travel time for paths connecting well 1 to well 3.

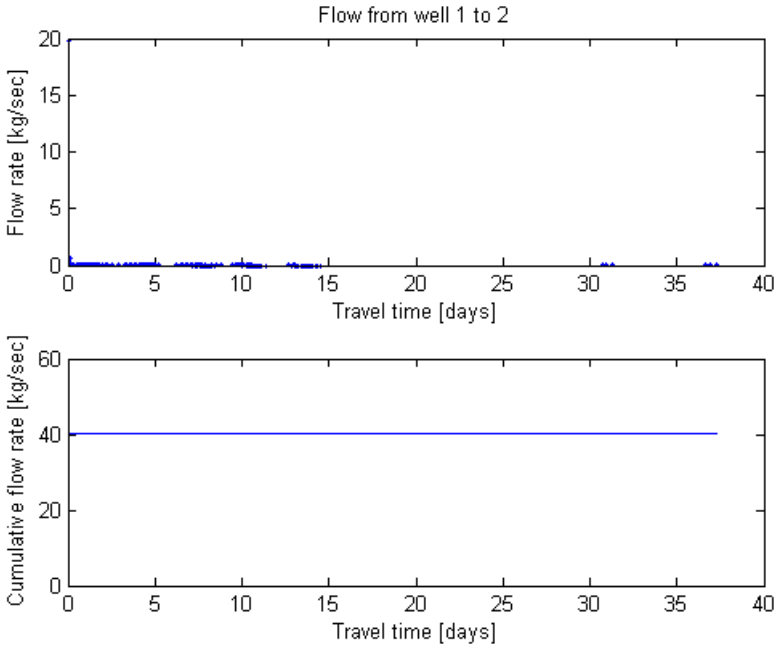

Figure 1.19: Flow rate vs. Travel time and Cumulative flow rate vs. Travel time for paths connecting well 1 to well 2.

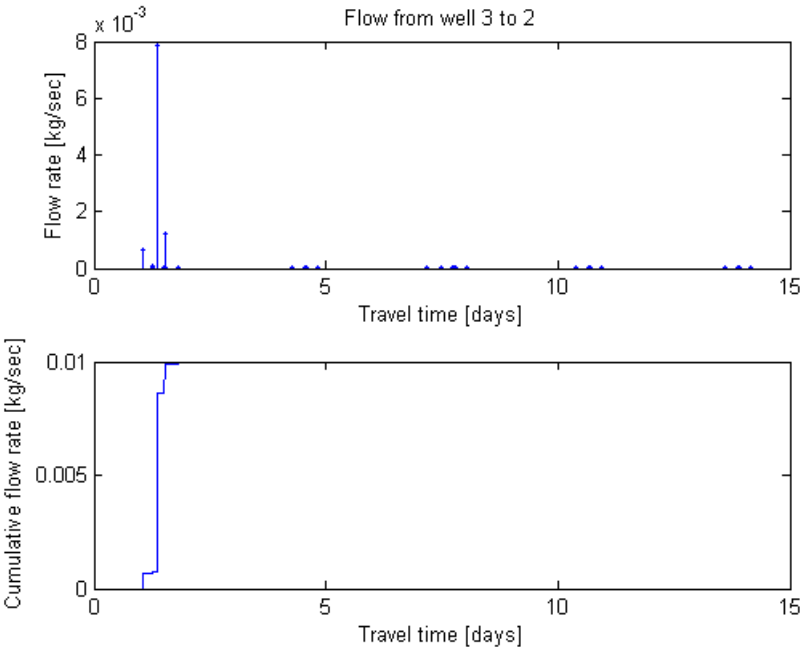

Figure 1.20: Flow rate vs. Travel time and Cumulative flow rate vs. Travel time for paths connecting well 3 to well 2.

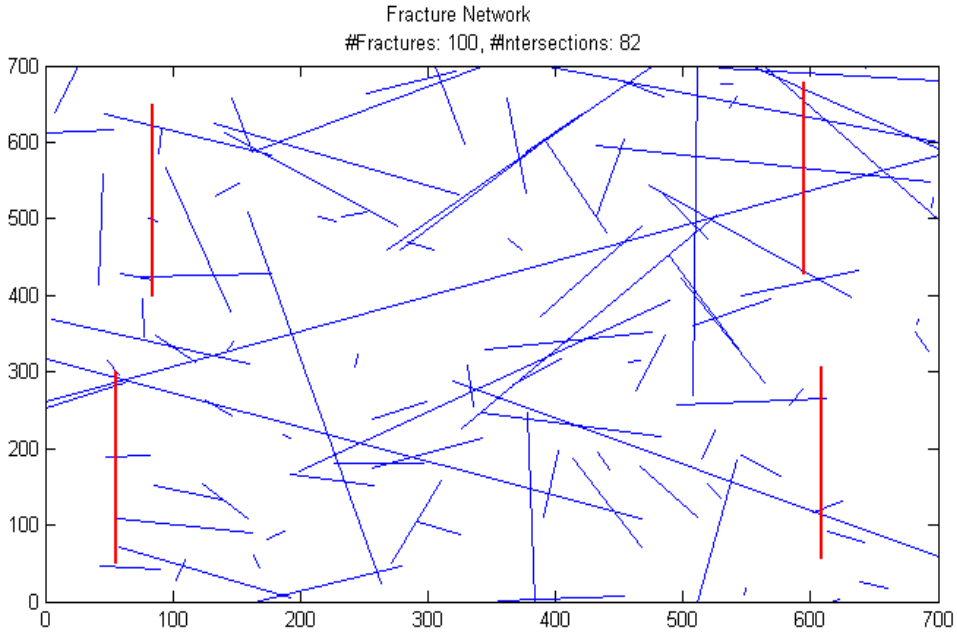

Figure 1.21: An example fracture network with two injection wells (red lines to the left) and two production wells (red lines to the right).

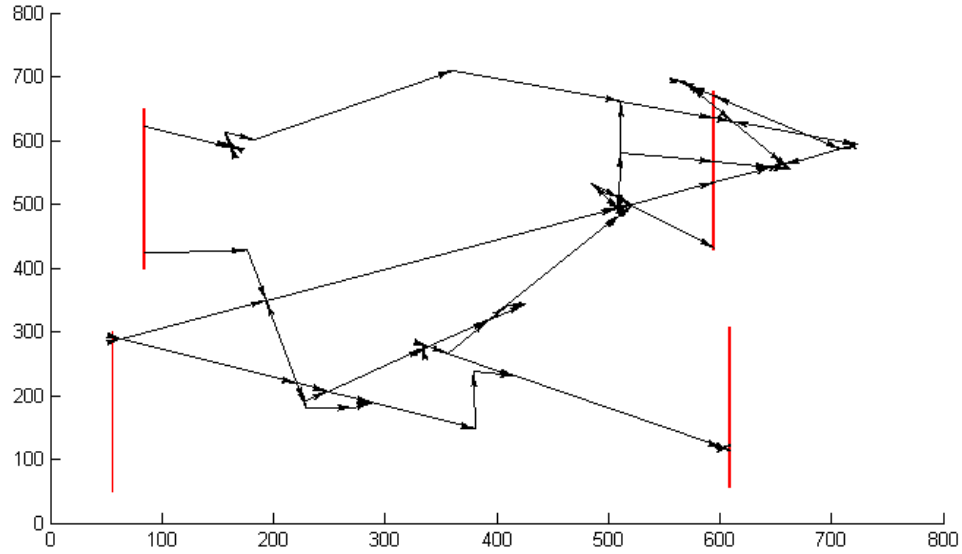

Figure 1.22: Flow paths and directions of flow through the fracture network presented in Figure 1.21.

The dispersion attributable to the fracture network was generated by collecting the arrival time and flow amount along each path. This is shown in Figure 1.23 (top) along with the cumulative amount of flow recovered (bottom).

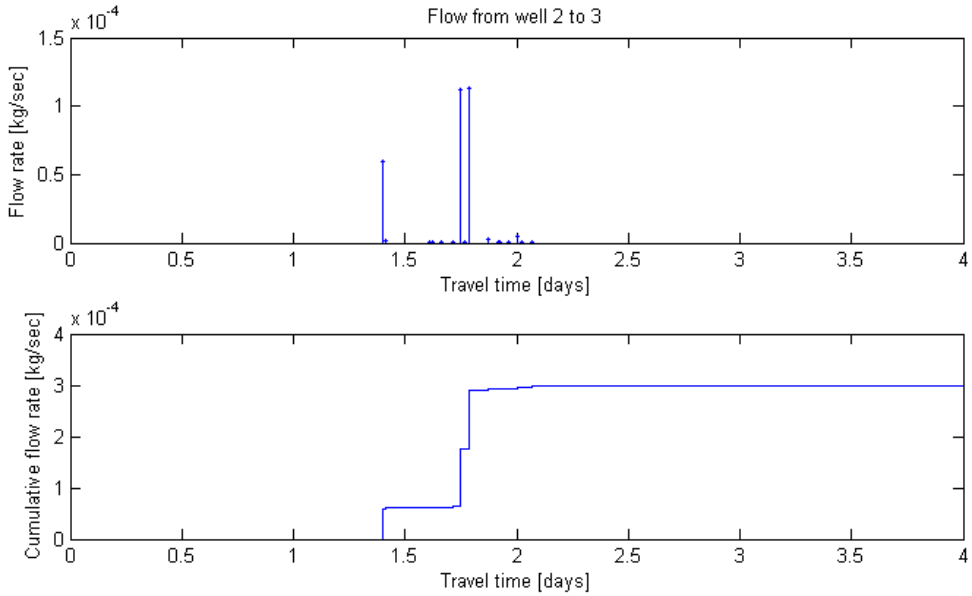

Figure 1.23: These plots illustrate the arrival time versus the amount of flow travelling along each path from well 2 (upper left) to well 3 (upper right).

Note that from these graphs we can see that three flow paths transmit the bulk of the flow from well 2 to well 3. Figure 1.24 illustrates the paths and labels the largest (in terms of flow), the most transmissible and the fastest.

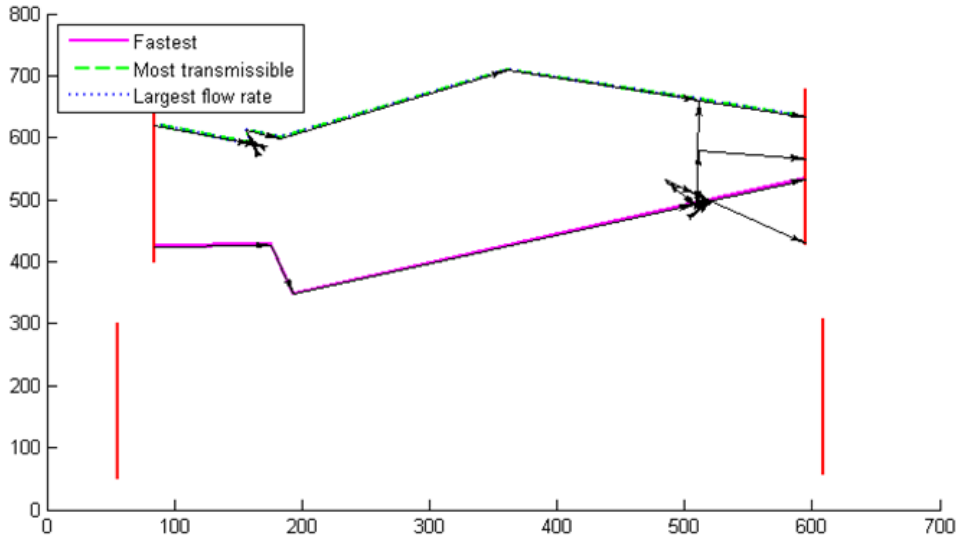

Figure 1.24: Flow paths from well 2 to well 3. Note that the fastest flow path is different from the most transmissible and largest flow path.

All but fracture induced dispersion effects (most importantly numerical dispersion) are circumvented in these calculations. That also means that some physically realistic dispersion effects need to be added, such as Taylor dispersion (Horne and Rodriguez, 1983), which is a significant effect generated by the interplay between molecular diffusion and the development of a velocity profile in laminar flow. It is important to understand the relative contribution of this effect as compared to the dispersion effects induced by the multiple flow paths through the fracture network to be able to understand whether it is plausible to extract information about individual fractures (or fracture paths) explicitly from tracer data. As discussed in the quarterly report from Fall 2009, this type of comparison is not easily done using traditional finite-volume reservoir models because of numerical dispersion effects.

An analytical solution to the one-dimensional advection-dispersion equation was used to compute the Taylor dispersion effects. The unit impulse kernel for this equation is defined as:

$$\begin{aligned}\kappa(t) &= \frac{u}{\sqrt{4\pi Dt}}\exp\left[-\frac{(L-ut)^2}{4Dt}\right] \\ &= \frac{1}{\sqrt{4\pi t_d t}}\exp\left[-\frac{(t_a-t)^2}{4t_d t}\right]\end{aligned} \tag{2.25}$$

where L is the length of the fracture segment, u is the flow velocity and D is the dispersion coefficient. The time values t_a and t_d are the advective and dispersive time scales, defined as:

$$t_a = L / u \tag{2.26}$$

and

$$t_d = D / u^2 \tag{2.27}$$

If a tracer slug of concentration c_o released at location $x=0$ over a (small) time interval Δt, the response seen at distance L_1 would be as described by following the convolution equation:

$$c_1(L_1,t) = \int_0^t c_o \Delta t \delta(t-\tau)\kappa_1(\tau)d\tau = \frac{c_o \Delta t u_1}{2\sqrt{\pi D_1 t}} \exp\left[-\frac{(L_1 - u_1 t)^2}{4D_1 t}\right] \tag{2.28}.$$

Here the subscript *1* refers to the properties of fracture segment 1 (edge 1, linking nodes 1 and 2). Similarly, the response at the next node (node 3, which we assume to be linked to node 2 via edge 2) could be computed by the convolution of $c_1(t)$ and the unit impulse kernel for edge 2.

$$c_2(L_2,t) = \int_0^t c_1(L_1, t-\tau)\kappa_2(\tau)d\tau \tag{2.29}.$$

Considering the fact that node 2 could branch out to more than one edge (say edges 3 and 4) the response at node 3 could be computed as:

$$c_2(L_2,t) = \frac{q_2}{q_2 + q_3 + q_4} \int_0^t c_1(L_1, t-\tau)\kappa_2(\tau)d\tau \tag{2.30}.$$

Continuing in this manner all the way to the final node gives the effective dispersive response along each path. Taylor dispersion was modeled by using Equation (1.31) to compute the dispersion coefficient in each fracture segment (Horne and Rodriguez, 1983).

$$D_{Taylor} \approx \frac{2}{105}\frac{u^2 b^2}{D_{mol}} \tag{2.31}.$$

The molecular diffusion coefficient, D_{mol}, was set to 10^{-10} m^2/s.

In general, the response for each path, K, was computed as:

$$c_K(t) = c_o \Delta t q_{tot} \prod_k \frac{q_k}{\sum_l q_l} \coprod_k \kappa_k(t) \tag{2.32}$$

where k runs over all edges on path K, and l runs over all edges with outflow from the node which edge k has flow out of. The symbol $\coprod$ denotes the successive convolution of all the kernels on path K.

In performing these successive convolutions numerically one must pay special attention to the time discretization used for the kernels. The operation can be viewed as generating two vectors, κ_1 and κ_2, with equal time discretization and taking the inner product between the first and the second, by incrementally shifting the second and padding nonoverlapping parts with zeros. This is better illustrated by the following example. Suppose:

$\kappa_1 = [\ 1\ \ 2\ \ 3];\quad \kappa_2 = [0\ \ -1\ \ 4]$

Then the convolution of the two would be computed by the taking the following inner products

```
        1   2   3
4  –1   0                    →          0

        1   2   3
    4  -1   0                 →          -1

        1   2   3
        4  –1   0             →          2

        1   2   3
            4  –1   0         →          5

        1   2   3
                4  –1   0     →          12
```

Note that here it is implied that the discretization interval is $d\tau$=1 and more importantly it must be the same for each κ such that the inner products make sense in view of them approximating the convolution integral. This method is relatively quick and simple when convolving only a few vectors with relatively few values. The outcome of convolving two vectors of size n and m will be of size n+m-1. Therefore, the length of one of the vectors used for each successive convolution will increase rapidly making this method computationally inefficient. Note that the size of $d\tau$ would often be quite small since it must be small enough to capture the sharp peaks in some of the kernel functions. This in turn made the length of the κ vectors large.

Successive convolutions are more easily dealt with in Laplace space, since convolution turns into multiplication under the Laplace transform. Taking the Laplace transform of Equation (1.32) gives:

$$\begin{aligned} L[c_K(t)] &= L[c_o \Delta t q_{tot} \prod_k \frac{q_k}{\sum_l q_l} \coprod_k \kappa_k(t)] \\ &= c_o \Delta t q_{tot} \prod_k \frac{q_k}{\sum_l q_l} L[\coprod_k \kappa_k(t)] \\ &= c_o \Delta t q_{tot} \prod_k \frac{q_k}{\sum_l q_l} \prod_k \tilde{\kappa}_k(s) \end{aligned} \tag{2.33}.$$

The Laplace transform of the kernel function for the one-dimensional advection-dispersion equation is:

$$\begin{aligned} \tilde{\kappa}_k(s) &= \frac{u_k}{\sqrt{4D_k s + u_k^2}} \exp\left[\frac{u_k - \sqrt{4D_k s + u_k^2}}{2D_k} L_k \right] \\ &= \frac{1}{\sqrt{4t_{d,k} s + 1}} \exp\left[\frac{t_{a,k}\left(1 - \sqrt{4t_{d,k} s + 1}\right)}{2t_{d,k}} \right] \end{aligned} \tag{2.34}.$$

Given this form of $\tilde{\kappa}_k(s)$ in Laplace space the path kernel can be computed quickly as:

$$\tilde{\kappa}_K(s) = \prod_k \tilde{\kappa}_k(s) \tag{2.35}$$

Then $\tilde{\kappa}_K(s)$ can be transformed numerically back to the time domain at well chosen time values, using a suitable numerical inversion method.

We tried working with two numerical inversion methods, the Stehfest method (Stehfest, 1970) and the Den Iseger method (Den Iseger, 2005). Each of the two methods computed function values in real space, at user supplied time values, given the functional form in Laplace space. The Stehfest algorithm was advantageous in the fact that it worked with any set of time values, while the Den Iseger algorithm was designed to return values at evenly spaced time intervals. Both algorithms were relatively easy to implement, although the Den Iseger method did require complex number arithmetic. The Stehfest algorithm ran faster, but it was less accurate, especially when it came to inverting functions that have a lot of variability at late times. That is, in cases where sharp responses at late times needed to be inverted, the Stehfest algorithm would fail while the Den Iseger method worked very well, as illustrated in Figure 1.25.

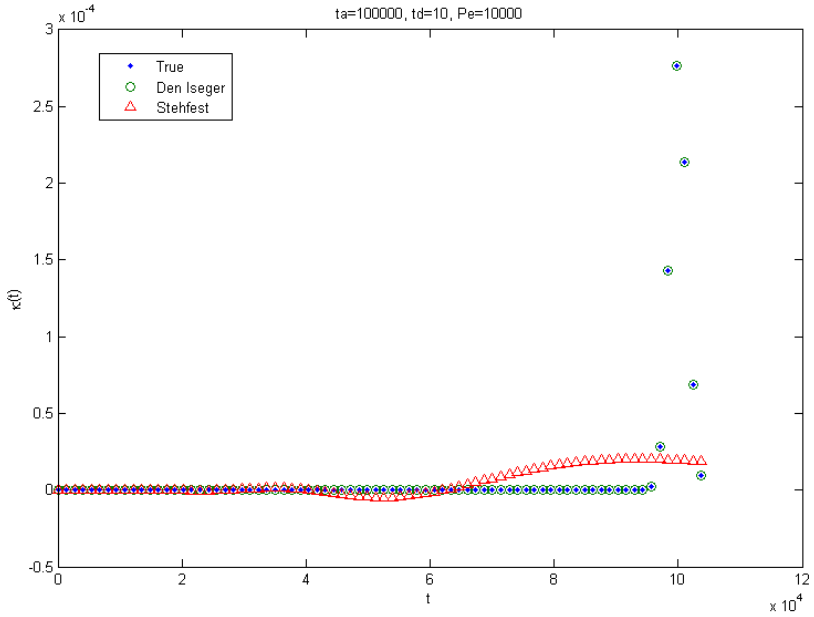

Figure 1.25: Inverting kernels with high Peclet numbers worked well with the Den Iseger method while the Stehfest algorithm would fail.

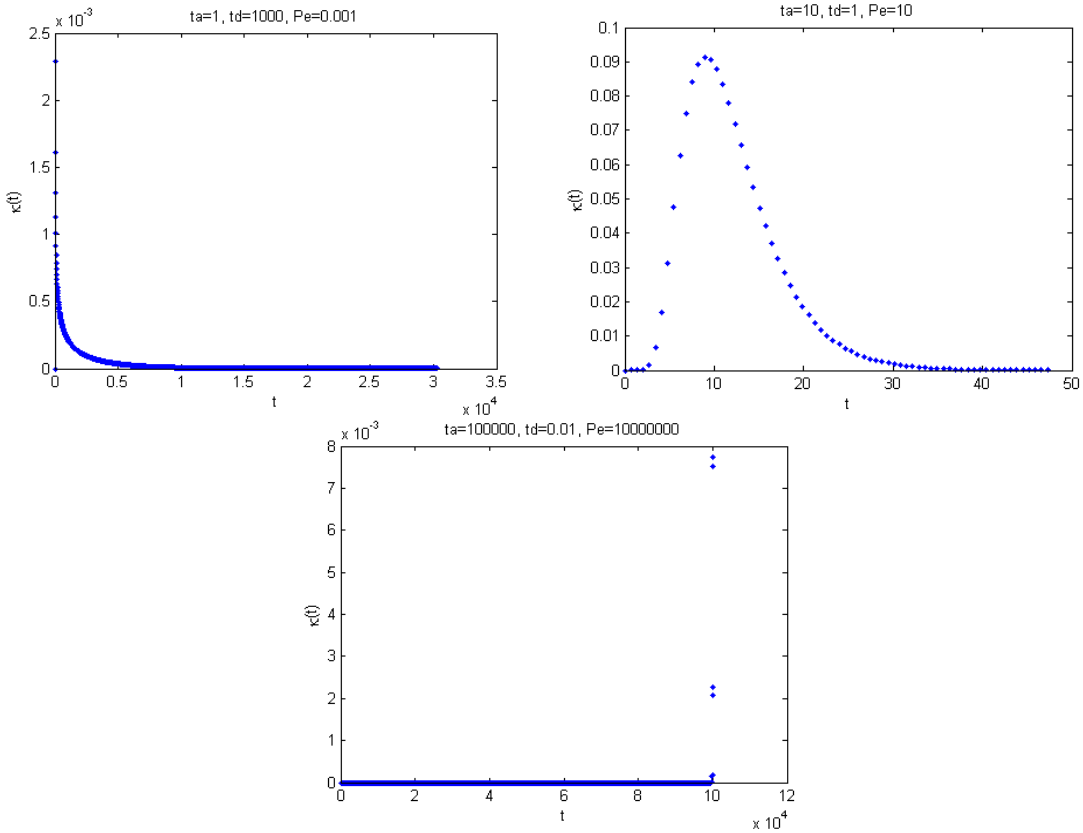

Figure 1.26: Kernels with Peclet numbers 10^{-3} (top left), 10 (top right) and 10^{7} (bottom).

Another important part of being able to invert the tracer kernels successfully was to make sure that an appropriate time discretization was selected. The kernels could take on various shapes as shown in Figure 1.26

In general, the kernels with low Peclet numbers ($uL/D = t_a/t_d$) have a sharp peak at early times and kernels with high Peclet numbers have a sharp peak at late times. To be able to capture these peaks properly with an even time discretization, we had to make sure that the time interval used was fine enough. To make this possible we computed the time location of the peak, t_{peak}, and the time at which the integral of the kernel reaches a certain small fraction, $t_{take\ off}$.

$$t_{peak} = \sqrt{t_a^2 + t_d^2} - t_d \tag{2.36}$$

$$t_{take\,off} \approx 2t_d erfc^{-1}(2\varepsilon) - 2\sqrt{t_d^2\left(erfc^{-1}(2\varepsilon)\right)^2 + t_a t_d erfc^{-1}(2\varepsilon)} + t_a \tag{2.37}$$

where, ε, is a small fraction, e.g. 10^{-3}. These time values bracket the transient part of the rise in concentration of the tracer slug. We decided that ten numerical values should suffice to capture this transient and thus chose the discretization time interval:

$$dt = \frac{t_{peak} - t_{take\,off}}{10} \tag{2.38}$$

Then, to determine the final value in the discretization we used a an approximation similar to Equation (1.37), that is:

$$t_{final} \approx 2t_d erfc^{-1}(2\sqrt{1-\varepsilon}) + 2\sqrt{t_d^2\left(erfc^{-1}(2\sqrt{1-\varepsilon})\right)^2 + t_a t_d erfc^{-1}(2\sqrt{1-\varepsilon})} + t_a \tag{2.39}$$

So the final discretization would be from *0* to t_{final} with spacing *dt*, but to remain practical in the computational effort we capped the number of discretization values at *2000* points.

The inversion and discretization were tested for a wide range of t_a and t_d values. One of the most meaningful ways of testing the quality of the results was to numerically evaluate the integral of the kernels, but this integral should equal 1. It turned out that results of identical quality were obtained as long as the ratio t_a/t_d remained the same. This ratio is the Peclet number. Figure 1.27 shows the integral of the kernel function versus the Peclet number for the kernel, with the kernel computed from the true equation in real space, and inverted from Laplace space using the Den Iseger and the Stehfest method. Since the discretization was finite, there were some errors in then numerical integration even when the true equation was used. This was most evident for Peclet numbers less than 1 and more than 10^7, but that error could be reduced by allowing a larger number of discretization points. Moreover, it was clear that the Den Iseger method was highly accurate for the entire range of values tested and the quality of the kernels computed by the Den Iseger method were entirely controlled by the quality of the time discretization. The Stehfest method, on the

other hand, would only work for Peclet numbers less than or equal to ~10. This is why the Den Iseger method was the preferred candidate for inverting the successive convolutions back to real space.

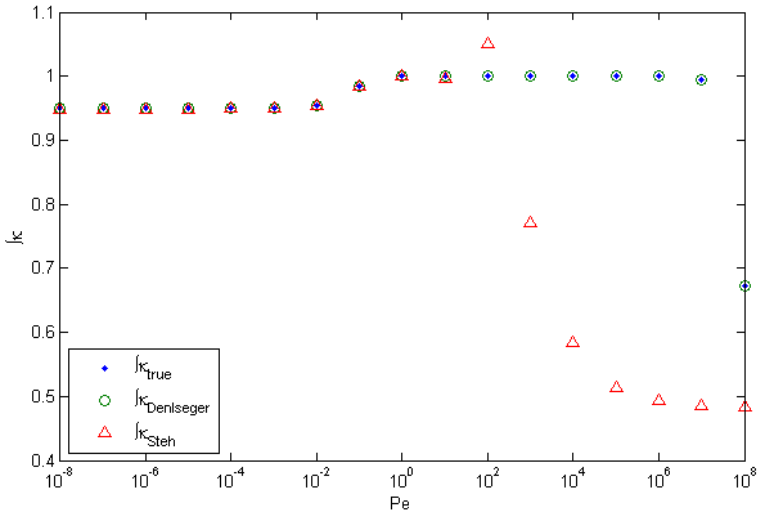

Figure 1.27: A comparison of the numerical integral of the discrete kernel function as computed analytically in real space (true) or analytically in Laplace space and then inverted to real space by the Den Iseger method or the Stehfest method. The comparison is made over a range of Peclet numbers. The ideal result should always equal one.

The time discretization discussed in Equations (1.36) to (1.39) was based on a single kernel. When dealing with the inversion of a kernel composed of successive convolutions, the time discretization was modified such that, instead of taking *dt* as described in (1.38), we used:

$$dt_K = \frac{\sum_k t_{peak} - \sum_k t_{take\ off}}{10} \tag{2.40}$$

where k goes over all the edges (fracture segments) on path K. And then

$$t_{final,K} = \sum_k t_{final,k} \tag{2.41}$$

The justification for this is that each kernel can be viewed as a probability distribution for a random number, say X_k. The successive convolution of those distributions is equivalent to finding the probability distribution for the sum $Y=\Sigma_k X_k$. This means that the extreme values (analogous to $t_{take\ off}$ and t_{final}) should sum up to even more extreme values for Y. For skewed distributions, the individual peak values will not sum up to the peak of the

combined distribution, but this effect did not seem to matter much for the numerous cases we tested.

By solving the problem of successive convolutions we were able to compute and compare the effects of Taylor dispersion to the effects of fracture induced dispersion on tracer returns. Figure 1.28 (top) shows the tracer return from well 2 flowing to well 3 if Taylor dispersion is included. The lower part of the figure shows the returns coming from individual flow paths. These return profiles indicate that at least two of the three main flow paths could be identified. Note that these computations were based on the same scenario as shown in Figure 1.24.

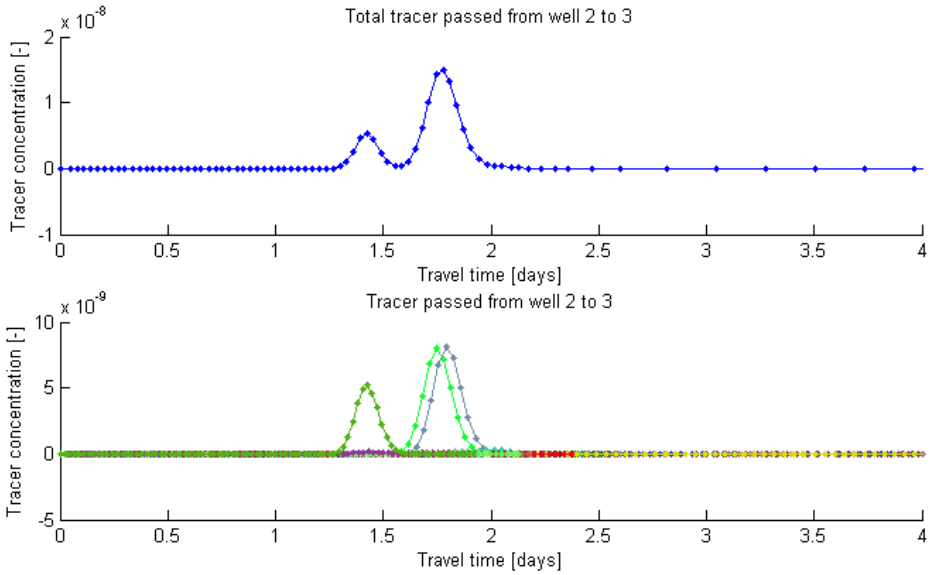

Figure 1.28: Tracer return curves of tracer from well 2 to well 3 including Taylor dispersion. The top plot has the total tracer return, while the lower plot shows the returns coming from each individual path. The largest slugs have a relatively high Peclet number, i.e. little dispersion.

The cumulative returns were compared to the cumulative returns computed without dispersion, as shown in Figure 1.29.

Figure 1.29 shows that in this case the fracture induced dispersion is significant and thereby one might hope to gain some information about the properties of the most significant flow paths between the wells. On the other hand, this result was very sensitive to the way the relationship between fracture length, L, and aperture, b, was defined. Models of the type $b=aL^s$ are referred to in the literature (Watanabe and Takahashi, 1995), where a and s are constants. For the case presented in Figures 1.22-1.24 and 1.28-1.29 we used

$$b = 1.5\times10^{-5} L^{0.6} \tag{2.42}$$

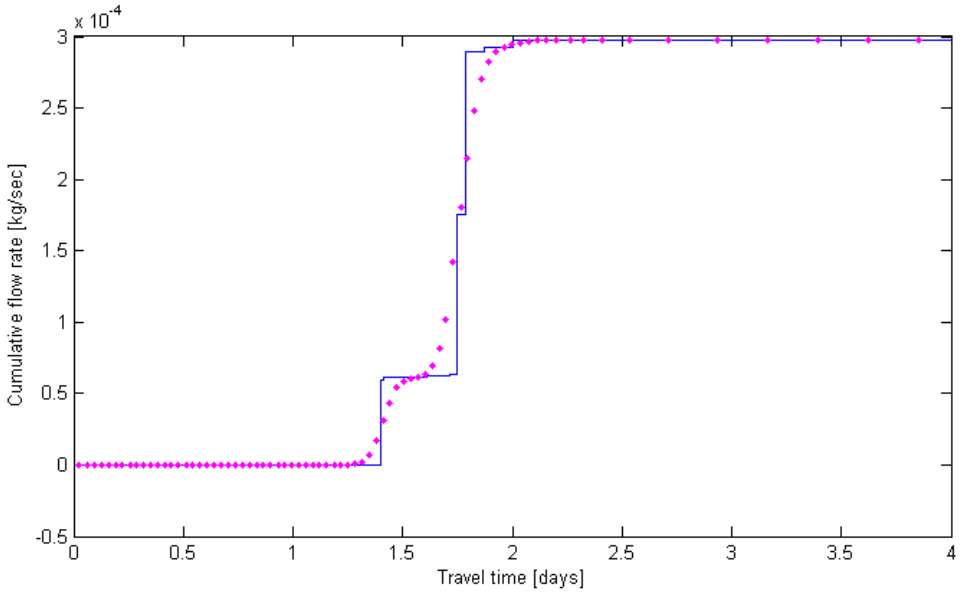

Figure 1.29: A comparison of the cumulative tracer returns (assuming 100% tracer injection) with (magenta dots) and without (blue line) Taylor dispersion. It seems fair to say that that the fracture induced dispersion is significant in this case, since it clearly affects the shape of the return curve.

The fracture lengths were initially drawn from a lognormal distribution and therefore *b* was also log normally distributed with values ranging from about 0.1 to 1 mm.

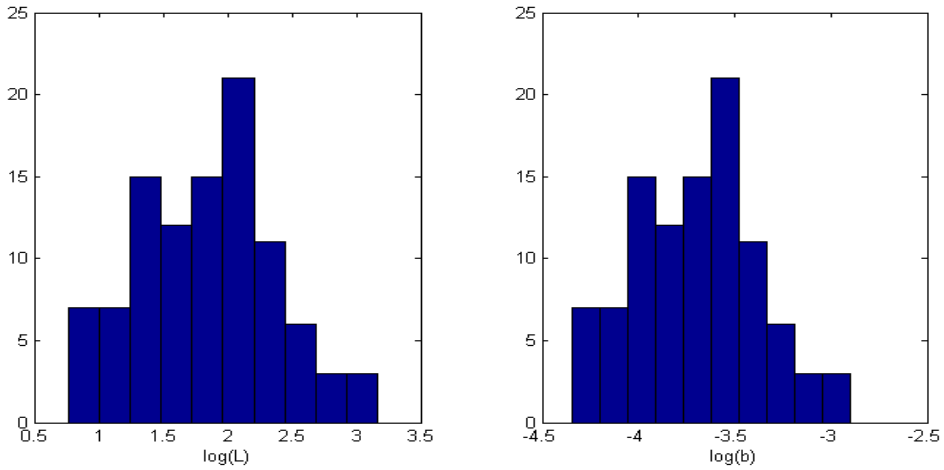

Figure 1.30: Distribution of the log of fracture lengths and aperture values.

Now we tried a slight change in way the apertures were modeled, by taking:

$$b = 3\times10^{-5} L^{0.6} \tag{2.43}$$

Now the apertures ranged from approximately 0.2 to 2 mm. A computation of the tracer returns for the same scenario as referred to in Figure 1.28 and Figure 1.29 gave the results seen in Figure 1.31 and Figure 1.32.

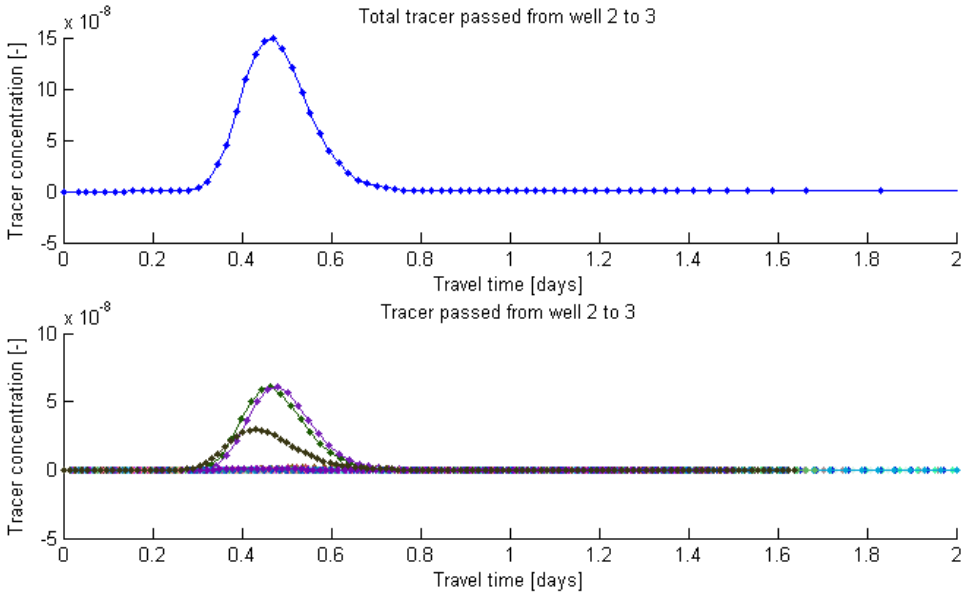

Figure 1.31: Tracer return curves of tracer from well 2 to well 3 including Taylor dispersion. The top plot has the total tracer return, while the lower plot shows the returns coming from each individual path. The largest slugs have a relatively low Peclet number, i.e. high dispersion.

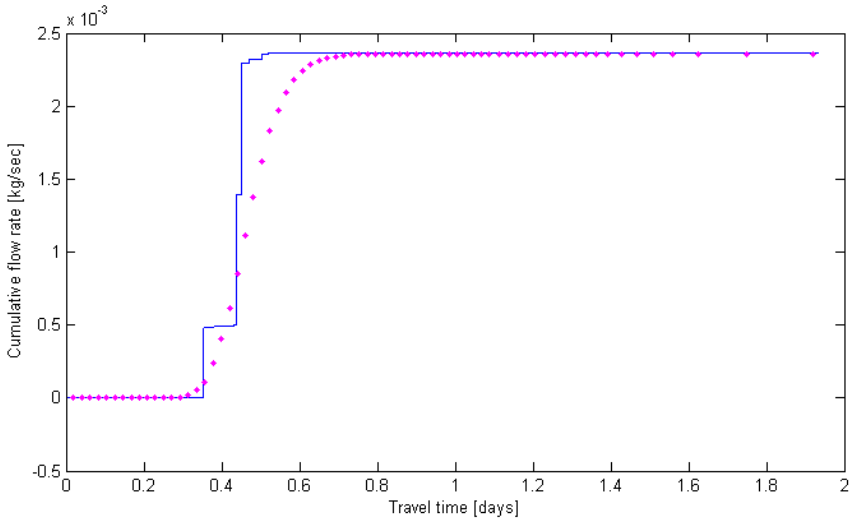

Figure 1.32: A comparison of the cumulative tracer returns (assuming 100% tracer injection) with and without Taylor dispersion. Here Taylor dispersion has become large enough to mask the contribution from individual fractures.

Note that the seemingly small change in the way the fracture apertures were modeled had a significant effect on the tracer returns. The three flow paths were now indistinguishable, because of the Taylor dispersion, which was in turn proportional to the square of the aperture. In other words, large apertures caused the low Peclet numbers, which made it harder to identify individual flow paths from tracer returns. From the definitions of Taylor dispersion and the Peclet number:

$$Pe = \frac{uL}{D_{Taylor}} = \frac{uL}{\frac{2}{105}\frac{u^2b^2}{D_{mol}}} = \frac{105}{2}\frac{D_{mol}L}{b^2}\frac{Hb}{q} \tag{2.44}$$

This shows that the Peclet number was approximately proportional to the inverse of the aperture and the inverse of the flow rate (and $q \sim k \sim b^2$). This meant the tracer returns from the largest flow paths would tend to have the lowest Peclet numbers (i.e. be most dispersed), and therefore these would tend to mask the returns coming from smaller flow paths. This effect is unfortunate since it could eliminate the possibility of identifying the number of dominant flow paths between two wells. It is important to understand that this may well be a common phenomenon, and that should be kept in mind in the interpretation of tracer tests.

1.5 INFERRING WELL-TO-WELL CONNECTIVITY

The quarterly reports from winter, spring and summer 2009 discussed a number of ways to infer well-to-well connectivity based on tracer data. A simple yet effective way was to compute the correlation between the time-shifted injection histories and the production history. A similar approach with time-shifted injection histories was used in conjunction with the ACE algorithm to find the optimal, smooth, transformations between the injection and production data. The strength of the ACE algorithm is that it quantifies the variability in the production data due to each injection data series, without a predefined relationship between the two. A slightly more restrictive approach to the problem was taken by using a nonparametric deconvolution technique to quantify the transfer function (i.e. tracer kernel) between well pairs. This technique does not demand a specific functional form for the kernel, other than requiring some degree of smoothness. The main restriction is that the data used to solve the problem must be obtained at steady state flow conditions, with only the tracer concentration varying. This is perhaps both the strength and weakness of the approach. The strength is that the well-to-well connections are specific to a specific combination of input flow rates, and therefore the input flow rates could be varied until an optimal set of connections is found. The main weakness is that obtaining enough data to find the connections at each set of input flow rates may take several months or years.

In the report for fall quarter of 2009 we discussed two additional deconvolution methods for inferring well-to-well connectivity. The first did not turn out to be useful, and was therefore left out of this annual report. It was, however, documented in the fall 2009 quarterly report, for completeness. The proposed method was based on a nonparametric deconvolution approach where the problem was transferred to Laplace space to investigate the possibility of using a regularization constraint derived from the functional form of the tracer kernel in Laplace space. The second method was a parametric deconvolution

approach. It is more restrictive than the nonparametric approach, in that a specific functional form for the kernel was assumed, and we inverted to find the parameters controlling that functional form. The following section describes the details of the method.

1.5.1 Deconvolution based on an analytical tracer return model

This section describes a parametric approach to solving the multiwell deconvolution problem. Although this approach is not very flexible, it gives a more complete picture of the methods that could be used, and complements the work we have done so far using nonparametric methods.

The problem involved finding the best estimate of the kernel functions $\kappa_k(t)$, which solve Equation (1.19).

$$c_p(t) = \sum_{k=1}^{N_r} \int_0^t c_{r,k}(t-\tau)\kappa_k(\tau)d\tau \tag{2.45}$$

where c_p is the produced tracer concentration, c_r is the injected tracer concentration and N_r is the number of injectors.

This convolution integral can be approximated as a matrix vector multiplication, $C_{r,k}\kappa_k$. Then the solution to (1.45) can be found by solving the least squares minimization problem (1.46). The kernels were restricted to the functional form of Equation (1.48). The objective was to find the values of the parameters, $t_{a,k}$, $t_{d,k}$ and f_k, which gave the best fit of the model to the production data.

$$\begin{aligned} &\underset{\vec{\alpha}}{\text{minimize}} \quad F(\vec{\alpha}) = \frac{1}{2}\left(\vec{c}_p - \sum_{k=1}^{N_r} C_{r,k}\vec{\kappa}\right)^T \left(\vec{c}_p - \sum_{k=1}^{N_r} C_{r,k}\vec{\kappa}\right) \\ &\text{subject to} \quad \vec{\alpha} \geq 0 \end{aligned} \tag{2.46}$$

Here the kernel and production data time series are represented as vectors, $\vec{\kappa}$ and $\vec{c}_p$ and the injection data are now included in the matrix $C_{r,k}$ which represents the convolution (approximated by the trapezoidal rule).

$$C_{r,k} = \begin{bmatrix} 0 & & \cdots & & 0 \\ (\tau_2-\tau_1)c_{r,k}(t_2-\tau_1) & (\tau_2-\tau_1)c_{r,k}(t_2-\tau_2) & 0 & \cdots & 0 \\ (\tau_2-\tau_1)c_{r,k}(t_3-\tau_1) & (\tau_3-\tau_1)c_{r,k}(t_3-\tau_2) & (\tau_3-\tau_2)c_{r,k}(t_3-\tau_3) & & \vdots \\ \vdots & \vdots & \vdots & \ddots & 0 \\ (\tau_2-\tau_1)c_{r,k}(t_N-\tau_1) & (\tau_3-\tau_1)c_{r,k}(t_N-\tau_2) & (\tau_4-\tau_2)c_{r,k}(t_N-\tau_3) & \cdots & (\tau_N-\tau_{N-1})c_{r,k}(t_N-\tau_N) \end{bmatrix} \tag{2.47}$$

The vector, $\vec{\alpha} = \left[t_{a,1}, t_{d,1}, f_1, \ldots, t_{a,N_r}, t_{d,N_r}, f_{N_r}\right]^T$ holds the parameters with respect to which the problem should be minimized. The kernel being considered was of the form:

$$\kappa_k(t) = \frac{f_k}{\sqrt{4\pi t_{d,k} t}} \exp\left[-\frac{(t_{a,k} - t)^2}{4 t_{d,k} t} \right] \tag{2.48}$$

Equation (1.46) describes a nonlinear least squares minimization problem. To solve it efficiently we computed the gradient and the Hessian. The gradient was computed as:

$$\frac{\partial F(\vec{\alpha})}{\partial \vec{\alpha}} = \begin{bmatrix} \left(C_{r,1} \frac{\partial \kappa_1}{\partial \alpha_1} \right)^T \\ \left(C_{r,1} \frac{\partial \kappa_1}{\partial \alpha_2} \right)^T \\ \vdots \\ \left(C_{r,N_r} \frac{\partial \kappa_{N_r}}{\partial \alpha_{3N_r}} \right)^T \end{bmatrix} \left(\vec{c}_p - \sum_{k=1}^{N_r} C_{r,k} \vec{\kappa}_k \right) = V^T \Delta \vec{c}_p \tag{2.49}$$

Similarly, the Hessian was computed as:

$$\begin{aligned} \frac{\partial^2 F(\vec{\alpha})}{\partial \vec{\alpha}^2} = & \begin{bmatrix} \left(C_{r,1} \frac{\partial^2 \kappa_1}{\partial \alpha_1^2} \right)^T & \left(C_{r,1} \frac{\partial^2 \kappa_1}{\partial \alpha_1 \partial \alpha_2} \right)^T & \left(C_{r,1} \frac{\partial^2 \kappa_1}{\partial \alpha_1 \partial \alpha_3} \right)^T & \vec{0}^T & \cdots & \vec{0}^T \\ \left(C_{r,1} \frac{\partial^2 \kappa_1}{\partial \alpha_2 \partial \alpha_1} \right)^T & \left(C_{r,1} \frac{\partial^2 \kappa_1}{\partial \alpha_2^2} \right)^T & \left(C_{r,1} \frac{\partial^2 \kappa_1}{\partial \alpha_2 \partial \alpha_3} \right)^T & \vec{0}^T & \cdots & \vdots \\ \left(C_{r,1} \frac{\partial^2 \kappa_1}{\partial \alpha_3 \partial \alpha_1} \right)^T & \left(C_{r,1} \frac{\partial^2 \kappa_1}{\partial \alpha_3 \partial \alpha_2} \right)^T & \left(C_{r,1} \frac{\partial^2 \kappa_1}{\partial \alpha_3^2} \right)^T & \vec{0}^T & \cdots & \\ \vec{0}^T & \vec{0}^T & \vec{0}^T & \ddots & & \left(C_{r,N_r} \frac{\partial^2 \kappa_{N_r}}{\partial \alpha_{3N_r-1} \partial \alpha_{3N_r}} \right)^T \\ \vec{0}^T & \cdots & & \left(C_{r,N_r} \frac{\partial^2 \kappa_{N_r}}{\partial \alpha_{3N_r} \partial \alpha_{3N_r-1}} \right)^T & & \left(C_{r,N_r} \frac{\partial^2 \kappa_{N_r}}{\partial \alpha_{3N_r}^2} \right)^T \end{bmatrix} \otimes \left(\vec{c}_p - \sum_{k=1}^{N_r} C_{r,k} \vec{\kappa}_k \right) \\ & + \begin{bmatrix} \left(C_{r,1} \frac{\partial \kappa_1}{\partial \alpha_1} \right)^T \\ \left(C_{r,1} \frac{\partial \kappa_1}{\partial \alpha_2} \right)^T \\ \vdots \\ \left(C_{r,N_r} \frac{\partial \kappa_{N_r}}{\partial \alpha_{3N_r}} \right)^T \end{bmatrix} \begin{bmatrix} C_{r,1} \frac{\partial \kappa_1}{\partial \alpha_1} & C_{r,1} \frac{\partial \kappa_1}{\partial \alpha_2} & \cdots & C_{r,N_r} \frac{\partial \kappa_{N_r}}{\partial \alpha_{3N_r}} \end{bmatrix} \\ & = H_2 \otimes \Delta \vec{c}_p + V^T V \end{aligned} \tag{2.50}$$

To accelerate convergence, the matrix H_2 was set to zero (i.e. Gauss-Newton method). The derivatives of the kernel functions with respect to α_i, were computed automatically using the Symbolic Toolbox in MATLAB. The MATLAB function fmincon was then used to

solve problem (1.46), using the trust region reflective algorithm. The objective function had a number of local minima and therefore it was necessary to try a few different initial guesses to get convergence to the known "true" solution. An example with five injectors and one producer is shown in Figure 1.33. As before we used somewhat idealized injection histories to make the problem better posed.

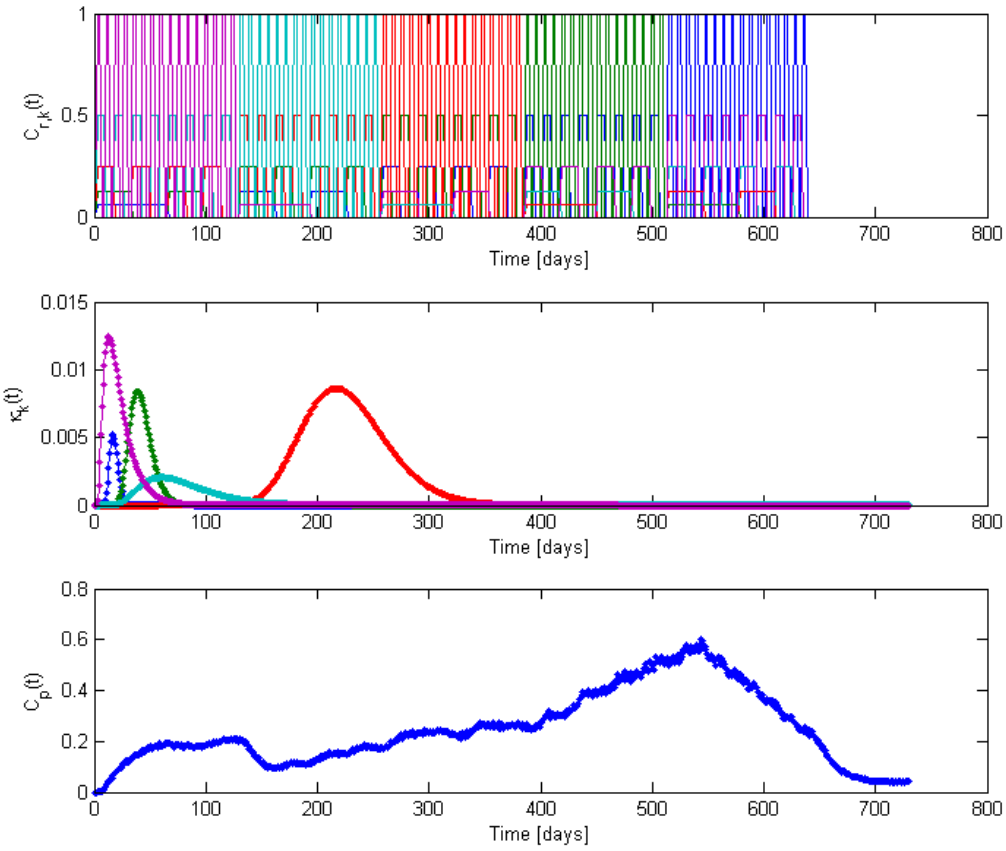

Figure 1.33: Injection history, random kernels and corresponding production history for five injectors and one producer.

Convergence to the "true" minimum was achieved after 16 trials with random initial guesses for $\vec{\alpha}$. Each trial computation took only a few seconds (~10-30 sec) to run in MATLAB. A comparison between the true kernels and the estimated kernels is shown in the top part of Figure 1.34 and the fit to the production data is shown on the lower graph. Table 1.1 shows the parameter estimates and the true parameters used.

Table 1.4: Summary of parametric estimates for fit shown in Figure 1.34.

	$t_{a,true}$	$t_{a,est}$	$t_{d,true}$	$t_{d,est}$	f_{true}	f_{est}
κ_1	17.1	16.9	0.43	0.56	0.05	0.06
κ_2	40.0	40.5	1.14	1.05	0.20	0.20
κ_3	220.0	219.4	3.14	3.18	0.80	0.80
κ_4	66.7	67.1	6.67	6.22	0.15	0.15
κ_5	16.0	15.9	3.20	3.14	0.30	0.30

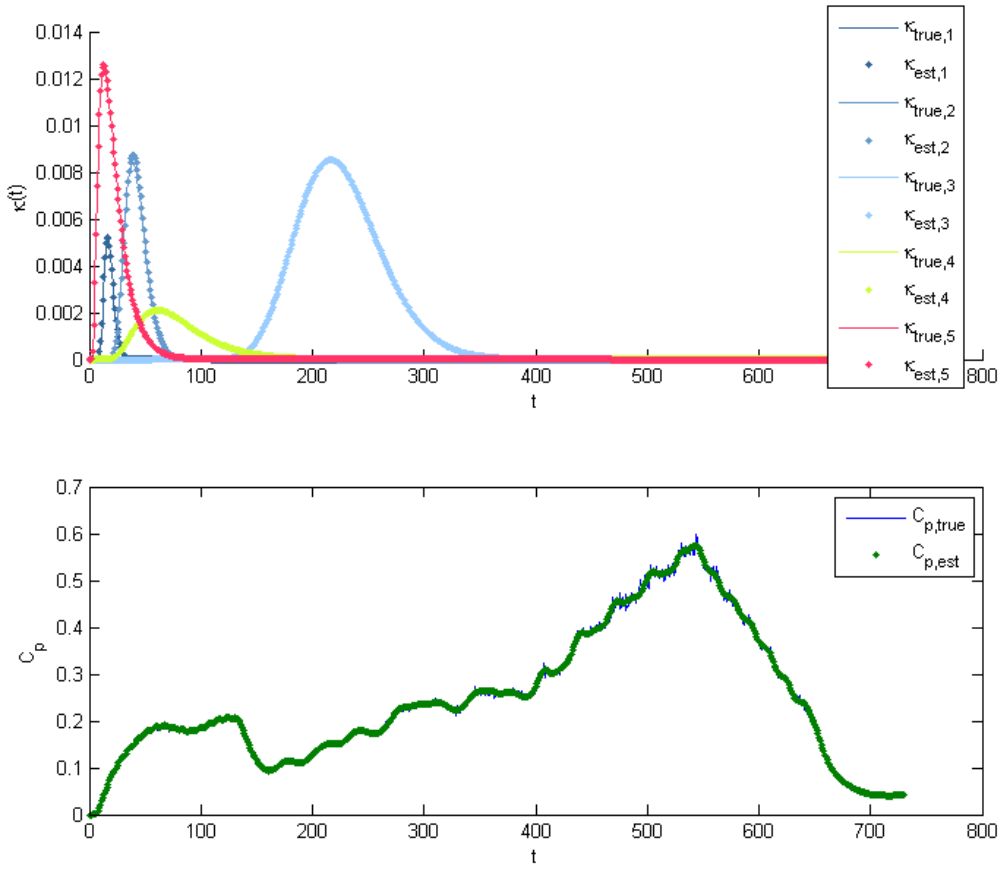

Figure 1.34: The estimation of five kernels and the fit to production data after deconvolution with a good initial guess.

The case shown here did yield an unrealistically good fit because the production history was generated with the same model as we were trying to fit to the data. In reality the kernels could be more like the ones shown in Figures 1.28 or 1.31, and therefore kernel models with sums of two (or even three) simple kernels might be more appropriate. That is, instead of considering kernels of the form (1.48) one might want to use:

$$\kappa_k(t) = \frac{f_{1,k}}{\sqrt{4\pi t_{d1,k} t}} \exp\left[-\frac{(t_{a1,k} - t)^2}{4 t_{d1,k} t} \right] + \frac{f_{2,k}}{\sqrt{4\pi t_{d2,k} t}} \exp\left[-\frac{(t_{a2,k} - t)^2}{4 t_{d2,k} t} \right] \tag{2.51}$$

When poor initial guesses to the solution were made the minimization algorithm would converge to a local minimum with results such as those shown in Figure 1.35.

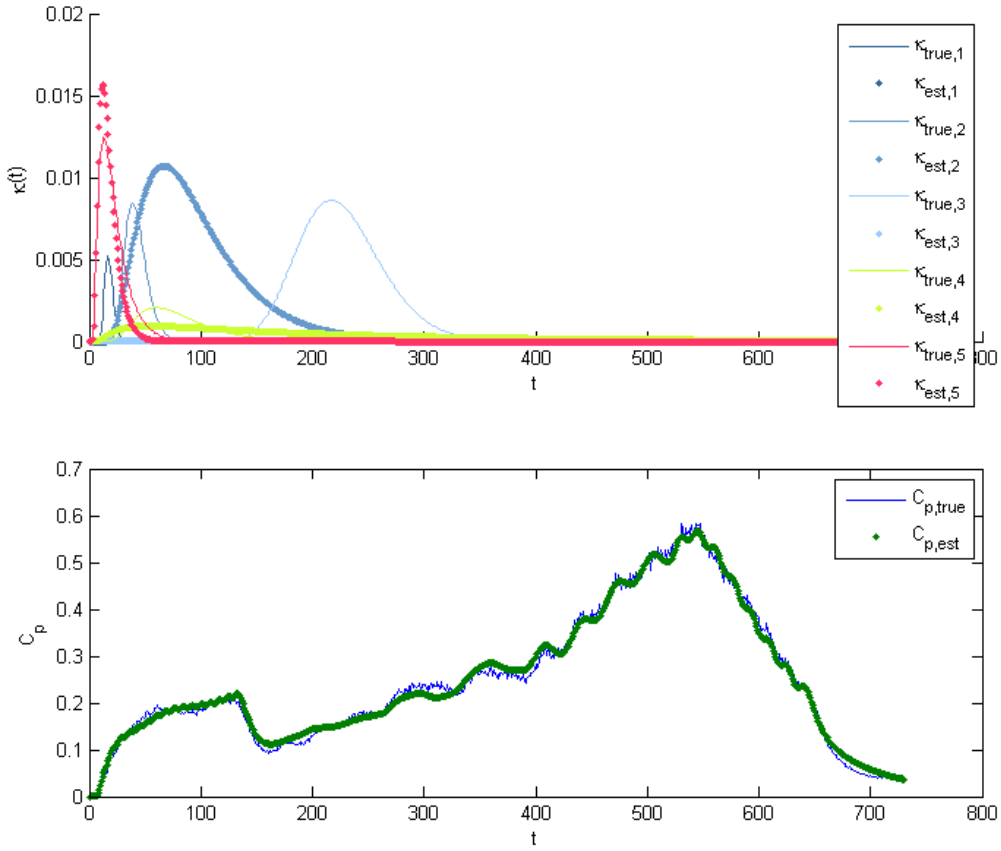

Figure 1.35: Results showing a solution of problem (1.46) with convergence to a local minimum. Even though the fit to the production data might seem quite good, the kernel estimates could be quite far off.

The problem of needing a good initial guess could be combated in a few different ways. Transformations of the parameter space might be helpful, e.g. by searching for *log(α)* in cases where α is believed to be lognormally distributed; or by modifying problem (1.46) to a total least squares problem, where the combination of the distances in t and c_p are being minimized. We played a bit with the idea of a logarithmic transformation of the parameter space for t_a and t_d with no obvious improvements, but the testing was not very rigorous. The total least squares approach would require more work, but for many practical purposes, trying a few initial guesses would be a satisfactory approach.

1.6 FUTURE WORK

1.6.1 Finite-volume discrete fracture models

Limited additional work is planned with discrete fracture models based on finite-volume method, in this specific research project. Any further uses will most likely be merely to produce synthetic data for testing inversion methods. However, based on our experience these simulations, we will mention that it might be of interest to use an appropriate upscaling algorithm (e.g. Gong, 2007) and compare the results obtained to the discrete fracture method used here. This would be useful since the computational time for the dense fracture network was on the margin of being feasible. Another way to make these computations more efficient might be use a total variation diminishing scheme (Lange, Bousian, and Bourbiaux, 2005, Wu and Forsyth, 2008). Moreover, it seems like adding a formulation of Taylor dispersion should be possible if the explicit fracture discretization of Karimi-Fard et al. (2003) is used.

Finally, the task of combining these simulation methods with more realistic fracture network models should be addressed. As an example, the FRACMAN software is built around an integrated analysis of various data sources ranging from conceptual geological models to seismic, and pressure transient data analysis. Much of the workflow is based on stochastic fracture generation, which in combination with appropriate geostatistical methods could lead to novel history matching algorithms. The similarity distance and dimensionality reduction methods being developed at the Stanford Center for Reservoir Forcasting (SCRF) seem particularly appealing.

1.6.2 Semianalytical discrete fracture network model

We believe that the simplified discrete fracture network (DFN) method can still be improved. One of the more promising possibilities is to remove the steady state assumption. We believe that by viewing analytical solutions of the advection-dispersion equation in terms of cumulative flow rate (instead of time), the return profiles could be computed efficiently. Three-dimensional simulations based on the channeling concept discussed by Tsang and Neretnieks (1998) could also be supported given a three-dimensional model of channel dominated fractures.

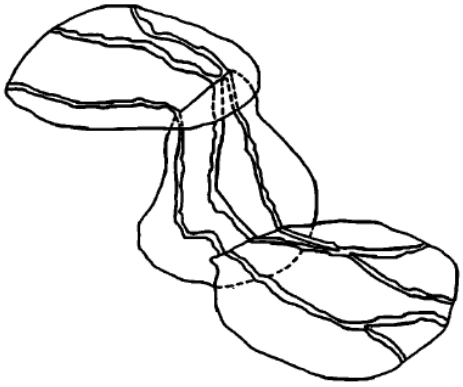

Figure 1.36: A conceptual channeling model of three intersecting fractures taken from Tsang and Neretnieks (1998).

Accoring to Tsang and Neretnieks (1998), the channeling models tend to yield tracer return curves with long tails. This should be confirmed by our model and could perhaps be explained analytically through further analysis of successive convolutions.

1.6.2.1 Thermal dispersion

Adding thermal dispersion effects to the simple DFN method seems to be a bit more challenging than adding tracer dispersion effects. The main reason for this is that the propagation of the thermal front depends much more strongly on the matrix surrounding the fractures and to some extent the interaction between the various flow paths through the matrix. An analytical solution (Lauwerier 1955) has been identified which can be used to describe the propagation of a thermal front in a planar fracture surrounded by two infinite slabs of impermeable rock. The equation is as follows:

$$\mathrm{T}_n(x,t) = \frac{\mathrm{T}_o - \mathrm{T}(x,t)}{\mathrm{T}_o - \mathrm{T}_{inj}} = erfc\left\{\left[\frac{(\rho_w C_w)^2}{K_r \rho_r C_r}\left(\frac{qH}{Ax}\right)^2\left(t - \frac{\phi\rho_w C_w + (1-\phi)\rho_r C_r}{\rho_w C_w}\frac{Ax}{q}\right)\right]^{-1/2}\right\} \qquad (2.52)$$

where now T denotes the temperature, ρ is density, C is specific heat capacity, K is thermal conductivity, ϕ is porosity and A is the cross sectional area of the fracture (normal to the flow direction). The subscript o refers to the initial state, r refers to the rock and w to the water.

Equation (1.52) should work well when only one major flow path dominates the flow in the reservoir or if the major flow paths are few and far apart. If however, there are multiple large flow paths cooling down the reservoir at similar time scales, these flow paths will interact with each other through the matrix. To account for that, it might be possible to use an equation similar to Equation (1.52), but with less restrictive boundary conditions (e.g. with surrounding rock matrix slabs of finite dimension, or even a specific shape). This would presumably make it easier to implement semianalytical approximations to what the thermal arrival profile might look like, even when there are several major flow paths

interacting through the matrix. One such equation was presented by Gringarten et al. (1975):

$$T_n(x,t) = \frac{T_o - T(x,t)}{T_o - T_{inj}} = L^{-1}\left\{\frac{1}{s}\exp\left(-\frac{x}{L}s^{1/2}\tanh\left(\frac{\rho_w C_w q b_m/(b+b_m)}{2K_r H}s^{1/2}\right)\right)\right\} \quad (2.53)$$

Note that the solution is presented in Laplace space ($L^{-1}\{.\}$ denotes inverse Laplace transform). There is also a dependence on the length of the fracture, L, and the distance from the fracture wall to the closed boundary, b_m.

1.6.2.2 Characterizing and screening an ensemble of DFNs

The simple DFN method is in a way a proxy model for discrete fracture networks. Proxy models are commonly employed when an approximate, quick solution is sought, e.g. in history matching work flows (Suzuki, Caumon, and Caers 2008; Suzuki and Caers 2008). The tracer response for a given set of well pressures can be quickly approximated using the simple DFN method. Therefore, if tracer data is available, the method should be a good screening tool for accepting or rejecting plausible models from an ensemble of stochastically generated DFNs.

The applicability of doing this type of screening could be tested by generating an ensemble of fracture networks and taking one of those as the "true" reservoir. The tracer response of each of the other models would then be computed and compared to the "true" model response with some sort of acceptance criterion. Thereafter, the ensemble of accepted fracture networks would be compared to the initial ensemble created to get a sense of how much the tracer history match reduced the uncertainty in the fracture distribution. The "true" model could also be used to compute the tracer response at another set of well pressures. The new set of pressures would then be used for all the other models created and the range of uncertainty about the tracer response (and thermal response) could be compared using the entire initial ensemble, and the history matched ensemble.

1.6.3 Inferring well-to-well connectivity

Future work on well-to-well connectivity will be directed towards estimating tracer transfer functions under variable flow rate conditions. The principal concern in that matter is to understand the interplay between solute flow rate, volumetric flow rate and fluctuations in concentration. We will start by analyzing some simple discrete fracture models and continue to increase the complexity depending on how well the estimation methods work. This could be accomplished by evaluating the tracer kernels at several different injection rates and from that trying to guess what the kernels would look like at other intermediate injection rates, or by finding a non-dimensional representation of the kernel function, that applies at all flow conditions. Alternative approaches might also be considered such as attempting find the injection rates that minimize the variability in the tracer production signal. The ACE algorithm, discussed in the quarterly report from winter 2009 may lend itself well to this type of analysis. Neural networks might also be a useful tool for this problem.

Tracer and thermal transport is inextricably linked to pressure and flow rate in the reservoir. To further our understanding of pressure and flow rate signals, we have begun reviewing signal processing methods for such data. For example, nonparametric multiwell deconvolution of pressure signals have been discussed by Levitan (2006) and von Schroeter and Gringarten (2007). Knowing both the tracer kernel and the pressure kernel for well-to-well connections could then be used to optimize injection schedules where the objective would be to provide maximal pressure support for production at the same time as the possibility of premature breakthrough would be minimized.

For interpretation of pressure or rate signals it is important to have variable pressure (injection rates) to be able to decompose the signal. On the other hand, deconvolution of tracer data with variable flow rates might turn out to be infeasible. Therefore, in practice, it might be necessary to have a variable injection rate test performed first to get a rough idea of which wells might be well connected from the pressure transients, and then use that information to improve the design of the tracer injection tests.

1.7 CONCLUSIONS

Characterization of fractures in the subsurface using production data is a fairly general topic. Early in the year we looked into traditional reservoir simulation with discrete fractures, to gain better understanding of how the various measureable properties propagate through fractured reservoirs. These traditional simulations provided valuable insights into aspects of the transport mechanisms for pressure, temperature and tracer. On the other hand, the simulations were quite computationally inefficient and were incapable of capturing a number of important physical attributes of tracer transport.

The limitations of traditional simulators led to the development of a semianalytical simulation method. The method is focused on capturing the dispersion induced by the fracture network and combining that with molecular diffusion effects driven by the velocity profile within the fractures themselves. This simulation method is free of numerical dispersion and has given valuable insight into how the shape of tracer return curves is defined by fractures. Future work in this field includes developing methods to compute tracer return curves with transient flow rates through the reservoir.

Work on revealing well-to-well interaction data based on tracer tests was also extended. Our efforts have been most successful when assuming that the flow rates are constant but the injected tracer concentrations are transient. That type of data is not generally available from the field and therefore we have only been able to validate our method using synthetic data. We are currently investigating the possibility of lifting the constant flow rate restriction, to reveal well-to-well transfer functions between wells, that are not significantly affected by flow rates.

2. FRACTURE CHARACTERIZATION USING NANOPARTICLES

This research project is being conducted by Research Associates Mohammed Alaskar, Morgan Ames and Chong Liu, Senior Research Engineer Kewen Li and Professor Roland Horne. The objective of this study is to develop in-situ multifunction nanosensors for the characterization of Enhanced Geothermal Systems (EGS).

2.1 SUMMARY

Several types of nanoparticle were synthesized. These included spherical silicon dioxide, silver, and tin-bismuth alloy nanoparticles as well as nonspherical iron oxide nanoparticles. The synthesis, characterization and injection of these nanoparticles were completed.

The silicon dioxide nanoparticles were injected into a 1,000 cm long tube packed with sand. It was found that the silicon dioxide nanoparticles can be transported and recovered through a long flow path.

The iron oxide nanoparticle injection experiments were carried out using Berea sandstone. Iron oxide nanoparticles were not identified in effluent collected during the injection. The iron oxide nanoparticles were, however, observed within the pores at the inlet side of the core. To test the iron oxide nanoparticle transport mechanism in the absence of core materials, the nanoparticles were also injected into a slim tube packed with glass beads. The iron oxide exhibited very low mobility during injection through the slim tube packed with glass beads. To better understand the relationship between particle geometry and transport, the iron oxide was coated with SiO_2 and the surfactants TEA and PVP. The iron oxide coated with surfactant (PVP) was injected into a slim tube packed with glass beads. The coated iron oxide nanoparticles were not detected in the collected effluent.

As preliminary testing of transporting metal nanoparticles within the pores of porous media, silver nanoparticle injection into Berea sandstone was conducted. The concentration of silver nanoparticles in the effluent samples was measured using UV-visible spectrophotometry by measuring the nanoparticles absorption and relating it to particle concentration using a calibration curve. The return curve of the silver nanoparticle production was determined.

Finally, the Sn-Bi alloy nanoparticles were subjected to a heating test to investigate their melting behavior. This heated sample was characterized using dynamic light scattering (DLS) and scanning electron microscopy (SEM) imaging. For the heated sample, the DLS results showed a wider particle size distribution that included larger particles. SEM images showed agreement with the DLS results as well as visual clues that melting had occurred. However, due to the wide distribution of sizes in both the original and heated samples, rigorous analysis of size change due to melting could not be achieved based on the SEM images.

This report describes the synthesis and characterization of nanoparticles used during flow experiments. The results of the flow experiments are discussed in details. This report also

describes the construction of the slim tubes, the calibration of transducers, and the permeability and porosity measurements and calculations.

2.2 INTRODUCTION

Measurements made in geothermal systems are generally limited to those made in wells, however the performance of the reservoir is governed strongly by properties and behaviors in the interwell fractures. A better understanding of reservoir performance requires new methods of interwell measurement. The extraordinary properties of materials made at nanoscale could provide these requirements. Therefore, it is proposed to explore the possibility of utilizing nanoparticles as sensors to characterize fracture systems. The main idea is based on the fact that certain types of nanosensors have the ability to record data such as pressure and temperature within the reservoir. Actually, temperature-sensitive nanomaterials have been already used in biomedical industry for drug delivery to particular types of body cell. For geothermal field applications, it is envisioned that the nanoparticles of different sizes and shapes can accompany the injected fluids at one well and be recovered from another well within the same reservoir. The nanoparticles that made their way to the producing well will be analyzed and correlated with the fracture properties.

In the development of enhanced geothermal systems, the characterization of the size, shape and conductivity of fractures is crucial. Hydraulic stimulation of fractures is the primary means of creating functional geothermal reservoirs at such sites to allow economical heat recovery. The energy extraction rate is significantly dependent on the creation of fractured area within the targeted hot rock volume. Mapping fractured area is of equal importance. However, existing fracture characterization tools and analysis approaches are inadequate. Pressure and temperature are measured only at the wellbore, and it is not possible to determine the conditions out in the reservoir. There are no effective means to measure such properties far in the rock formations. Thus, the objectives of this research are to provide a new tool (nanosensors) and to develop reservoir engineering approaches to estimate reservoir parameters and characterize fracture networks based on the measurements from these tools.

In order to investigate the feasibility of utilizing nanosensors in illuminating reservoir properties in general and fracture network properties in particular, it was essential to verify their transport mechanism through typical formation rock core samples. Initial testing with nanoparticles was also required to develop the understanding of their optimum injection procedures, sampling strategies and characterization techniques. Accordingly, various laboratory-scaled core-flooding experiments with inert nanoparticle suspensions were conducted. Specifically, spherical nanoparticle suspensions were injected into Berea sandstones as well as slim tubes packed with sand or glass beads. Following the injection of spherically shaped nanoparticles, an investigation was initiated to assess the practicability of transporting wire-like nanoparticles through the pores of multiple porous media. These nanoparticles serve as precursor for the injection of functional nanosensors such as pressure- and temperature-sensitive nanotracers.

During this year, the design of slim tubes packed with sand or glass beads was completed. In particular, two 2,500 cm stainless steel and a 1,000 cm polypropylene slim tubes packed with sand were constructed. Standard measurements on the 1,000 cm polypropylene slim tube and Berea sandstone were performed, including the gas and liquid permeability, porosity and pore volume measurements.

The synthesis, characterization and injection of spherical silicon dioxide, silver, tin-bismuth alloy nanoparticles as well as nonspherical iron oxide nanoparticles were completed. The silicon dioxide nanoparticles were injected into the 1,000 cm long slim tube packed with sand. The iron oxide nanoparticle injection experiments were carried out using Berea sandstone. Dynamic light scattering (DLS), UV-visible spectroscopy and scanning electron microscopy were used to examine the effluent samples. To investigate the iron oxide nanoparticle transport mechanism in the absence of core materials, the nanoparticles were also injected into slim tube packed with glass beads. Further investigation to understand of the relationship between particle geometry and transport was carried out by coating the iron oxide with SiO_2 and the surfactants TEA and PVP. The iron oxide coated with surfactant (PVP) was injected into a slim tube packed with glass beads. As preliminary testing of transporting metal nanoparticles with the pores of a porous medium, silver nanoparticles injection into Berea sandstone was conducted. The concentration of silver nanoparticles in the effluent samples was measured using UV-visible spectrophotometry by measuring the nanoparticles absorption and relating it to particle concentration using a calibration curve. Finally, the Sn-Bi alloy nanoparticles were subjected to a heating test to investigate their melting behavior. This heated sample was also characterized using DLS and SEM imaging.

2.3 BEREA SANDSTONE AND SLIM TUBE CHARACTERIZATION

Prior to nanofluid injection, standard experiments to characterize the rock core as well as slim tubes packed with sand or glass beads were performed, including the pore size distribution (for core plug), porosity and permeability measurements. Core sample and slim tube dimensions, porosity, permeability, pore size distribution and pore volume calculations are summarized in Table 2.1.

2.3.1 Berea Sandstone Pore Size Distribution

The pore size distribution of the core samples was measured by mercury (Hg) intrusion method. The intrusion of mercury was performed using the AutoPore IV 9500 Mercury Porosimeter manufactured by Micromeritics. This porosimeter covers a pressure range up to 33,000 psia and pore diameter range from approximately 360 to 0.005 micrometers. The device has two low-pressure ports and one high-pressure chamber.

Prior to analysis, the sample must be weighed and all relevant sample information entered. Pressure points, at which data were collected, were then specified. Following that, the samples were loaded into a penetrometer and were ready for measurements. The analysis was conducted in two stages, low-pressure and high-pressure. Firstly, the penetrometer was loaded in the low-pressure port to evacuate all gases and then backfilled with mercury. The data were collected at pressures up to 30 psia. Secondly, the penetrometer was

removed and installed in the high-pressure chamber. The analysis was resumed and data were collected up to pressure as high as 33,000 psia. The principal idea behind the pore volume measurements was as follows. The pore volume data were generated through the calculation of the volume of mercury left in the penetrometer stem as pressure was applied. As pressure increased, mercury from the penetrometer stem was forced to enter the pores. Smaller pores require higher pressure to overcome capillarity. Mercury was the nonwetting phase, and its surface tension, contact angle and radius of curvature were used to obtain the pore diameter at a given pressure (Micromeritics, 2008).

Table 2.1: Cores and slim tube characterization data

Property	Measurement	Berea – Hematite injection	Berea – Silver injection	Slim tube packed with glass beads	Slim tube packed with sand
Dimensions (cm)	Diameter	3.8	3.8	0.4318	0.4318
	Length	4.9	4.1	30	1000
Porosity (%)	Hg intrusion	19	19	NA	NA
	Resaturation	17.1	17.1	46.8	35.5
Permeability (md)	Nitrogen perm.	152	152	-	50,200
	Apparent liq. perm.	72.2	72.2	-	40,100
	Liquid perm.	60.7	60.7	13,000	49,900
Size distribution (μm)	Largest pore	20	20	NA	NA
Pore volume (cc)	By saturation	9	8	2.39	51.9

Measurements conducted on the Berea sandstone showed the core to have pore sizes as large as 20 and 0.15 micrometers, respectively. The pore size distribution of the core sample is depicted in Figure 2.1.

2.3.2 Berea Core Characterization

The core sample tested was Berea sandstone of 3.8 cm in diameter and 4.9 cm in length. The gas and liquid permeabilities were determined. The Klinkenberg (gas slippage) effect was considered to evaluate the equivalent liquid permeability. Then, the liquid permeability for the same core sample was carried out. Porosity, permeability and pore volume results are summarized in Table 2.1. Note that the same core sample was used in iron oxide as well as the silver nanoparticle injections, except that the core sample was shortened during the latter injection (silver nanoparticle injection). So the rock properties of porosity and permeability are the same. The pore volume, however, changed from 9 cc to 8 cc.

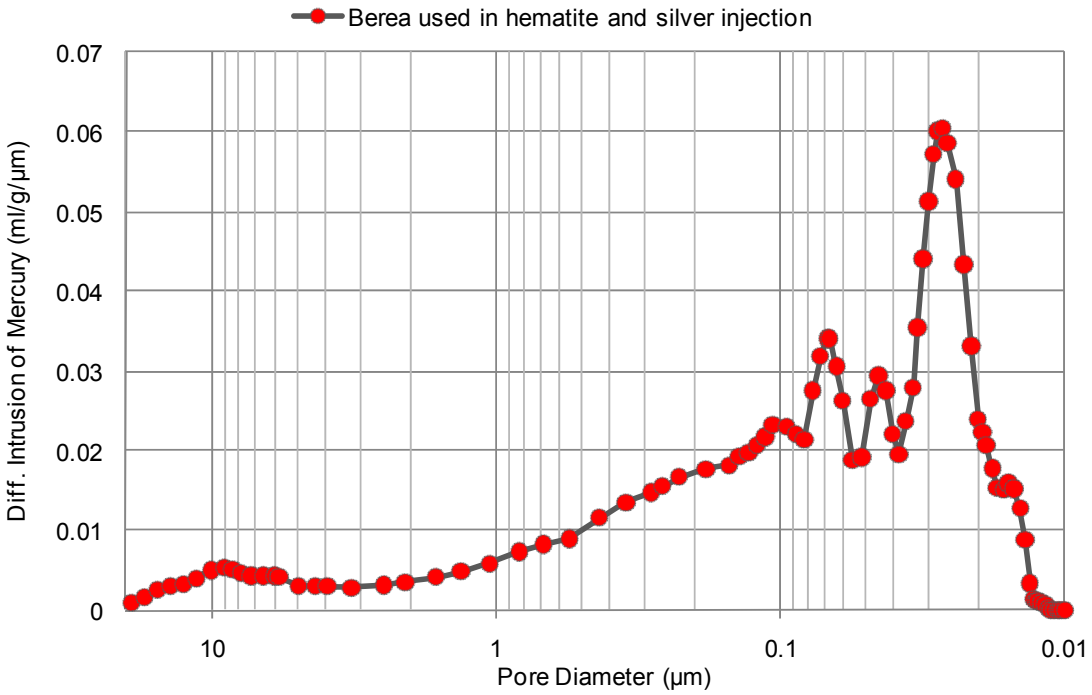

Figure 2.1: Pore size distribution of Berea sandstone core sample.

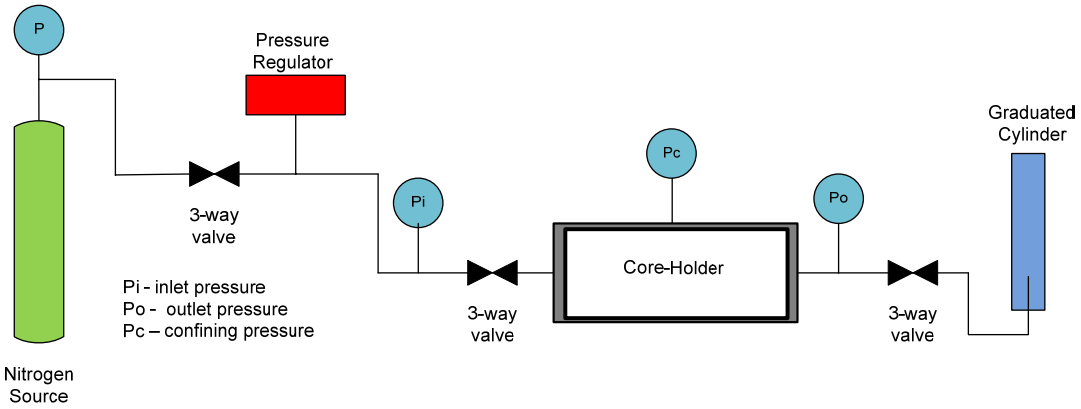

Figure 2.2: Schematic of the apparatus used for Berea sandstone gas permeability measurement.

Figure 2.2 is a schematic of the apparatus used in the measurement of gas permeability. The flow rate at the outlet was measured using a stop-watch and graduated cylinder. The pressures at the upstream (inlet) and downstream (outlet) of the core were measured using differential pressure transducers manufactured by Celesco Company. These transducers (Model DP30) have a linearity of 0.5% and a repeatability of 0.5% full scale. The diaphragms used in the inlet transducer and outlet transducers have the range from 0 to 100 psi and 0 to 25 psi, respectively. Both differential pressure transducers were calibrated using a standard pressure gauge with an accuracy of 0.1 psi. The pressure transducer calibration curves are depicted in Figures 2.3 and 2.4. The pressure calibration curves

indicate a good agreement between the standard pressure gauge and the differential pressure transducers.

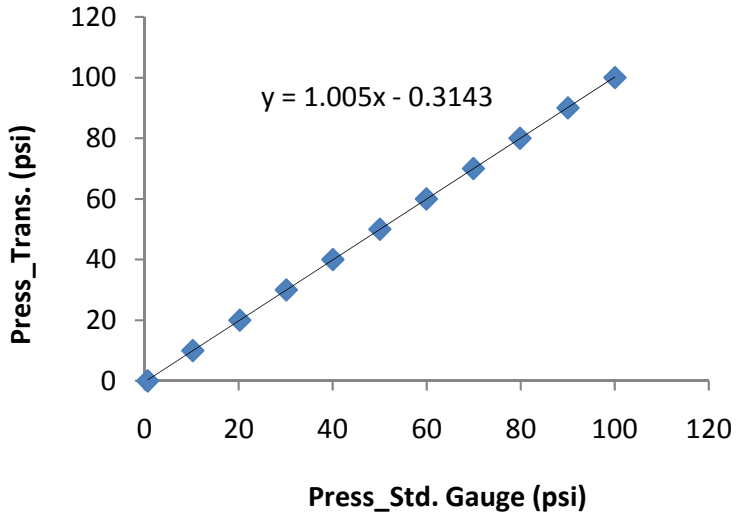

Figure 2.3: Calibration curve of the inlet pressure transducer.

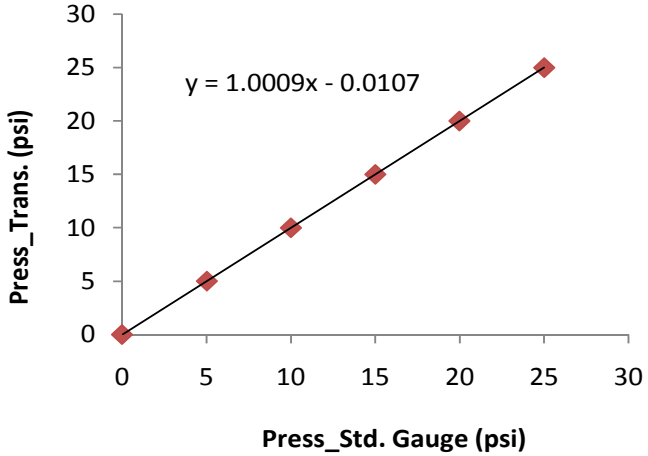

Figure 2.4: Calibration curve of the outlet pressure transducer.

The core was first dried in a furnace at 100°C under vacuum for 24 hours. After weighing the core sample, it was placed inside the core-holder under a confining pressure of 30 atm.g. The gas permeability measurement was then started by introducing nitrogen at different flow rates and inlet pressures. The average gas permeability was found to be around 152 md by applying Darcy's law for compressible fluids which is given by:

$$k_{gas} = \frac{2\mu p_{out} q_{out} L}{A(p_{in}^2 - p_{out}^2)} \tag{2.1}$$

where μ is the viscosity in centipoise, q_{tot} is outlet volumetric flow rate in cubic centimeter per second, A is the core cross-sectional area in square centimeter, L is the core length in centimeter and p_{in} and p_{out} are inlet and outlet absolute pressures in atmospheres, respectively.

The gas permeability as a function of the reciprocal of mean pressure is depicted in Figure 2.5. According to the Klinkenberg effect, extrapolating the straight line to infinite mean pressure (or zero reciprocal of mean pressure) intersects the permeability axis at a point designated as the equivalent liquid permeability (Amyx et al., 1960). In Figure 2.5, the average equivalent liquid permeability is approximately 72.2 md.

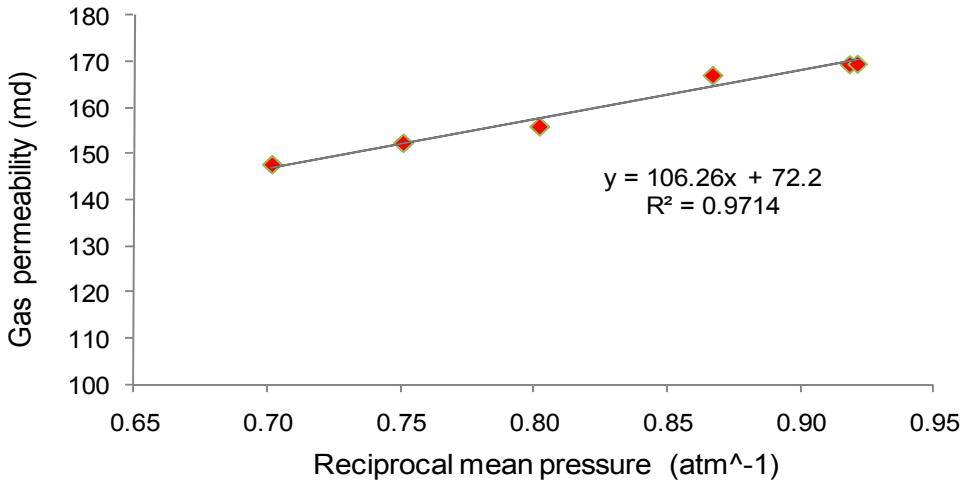

Figure 2.5: Berea core gas permeability versus the reciprocal of mean pressure.

The liquid permeability was measured on the same core sample directly. A schematic of the apparatus used in the measurement of liquid permeability is shown in Figure 2.6.

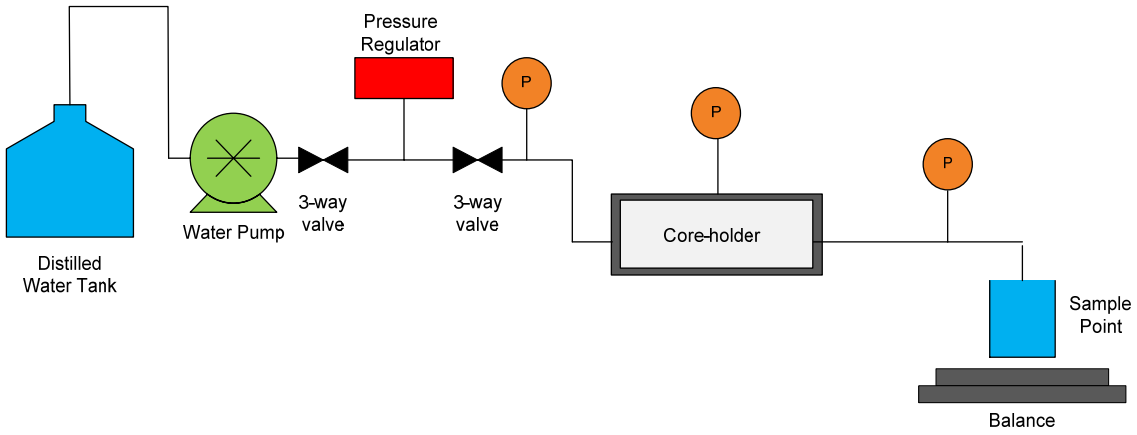

Figure 2.6: Schematic of apparatus for Berea sandstone liquid permeability measurement.

All differential pressure transducers had been calibrated previously as part of the gas permeability measurement. In addition, a water pump (Dynamax, Model SD-200) manufactured by RAININ Instrument Company was used to inject pure water. The minimum pumping rate of the pump is 0.05 ml/min with an accuracy of 0.01 ml/min. This pump is an automated constant-rate pump. The flow rates of the water pump were calibrated before the experiment using a stop-watch and a Mettler balance (Model PE 300). The accuracy of the balance is 0.01g and the range is from 0 to 300 g. The calibration curve for this pump at room temperature is shown in Figure 2.7. The measured flow rates were consistent with those specified on the pump.

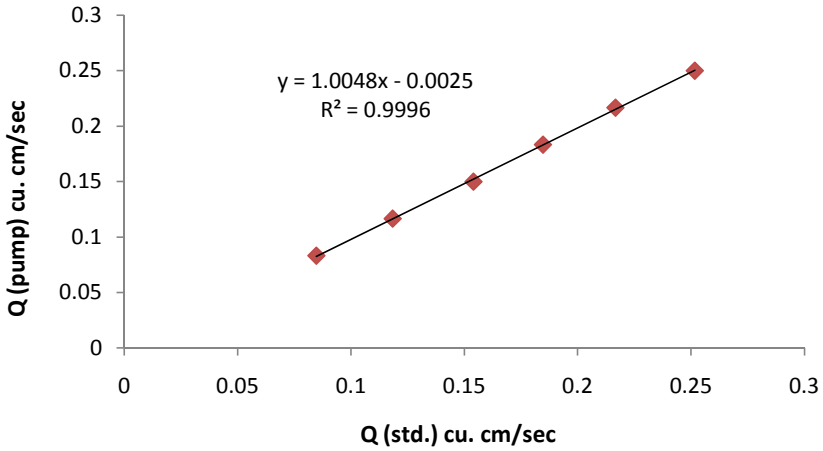

Figure 2.7: Water pump calibration curve.

The core sample was first saturated with water outside the core-holder. The core and related system were evacuated using a Welch Vacuum Pump (Model No. 8915A) for 4 hours at a vacuum pressure of about 20 millitorr to remove moisture. Pure water was introduced to completely submerge the sample. The core was then left submerged overnight and the remaining vacuum released to aid the process of saturation. After that the core was removed and wiped dry to remove excessive water on the surface. Finally, the core was weighed and hence its porosity was calculated. The core turned out to have a porosity of around 17.1 % and a pore volume of 9 cubic centimeters. During the injection of silver nanoparticles, the core was shortened by about 0.8 cm and therefore the pore volume was reduced to 8 cubic centimeters. The porosity calculation is as follows:

$$\phi = \frac{V_p}{V_B} * 100 \tag{2.2}$$

$$V_p = W_s - W_d \tag{2.3}$$

$$V_B = \pi r^2 l \tag{2.4}$$

where ϕ is the porosity in percentage, V_p and V_B are pore and bulk volumes in cubic centimeter, respectively. W_s and W_d are the weight of core after and before saturation, in

gram, respectively. r and l are the radius and length of the core in centimeter, respectively.

The average liquid permeability was found to be around 60.7 millidarcy. Darcy's law for horizontal flow was utilized to compute the permeability. Darcy's law for horizontal flow is given by:

$$k_{liq} = \frac{q\mu L}{A\Delta p} \tag{2.5}$$

where q is the volumetric flow rate in milliliter per second, μ is the viscosity in centipoise, L and A are the length and the cross-sectional area of the core in centimeter and square centimeter, respectively. Δp is the differential pressure across the core sample in atmospheres.

2.3.3 Characterization of Slim Tubes

The proof of concept of passing nanoparticles through porous media has been established for a short core but not over longer distances approaching those encountered in a subsurface reservoir. In order to investigate flow through a longer pore network, several slim tube apparatuses were designed and constructed. Initially, two 2500 cm stainless steel tubes were made and packed with sand. Once packed, the tubes were wound in coils, and sampling valves were installed at intervals along their length. The objective in choosing stainless steel was so that the slim tube can be used in an air bath for high temperature experiments. One of these stainless steel slim tubes is pictured in Figure 2.8a.

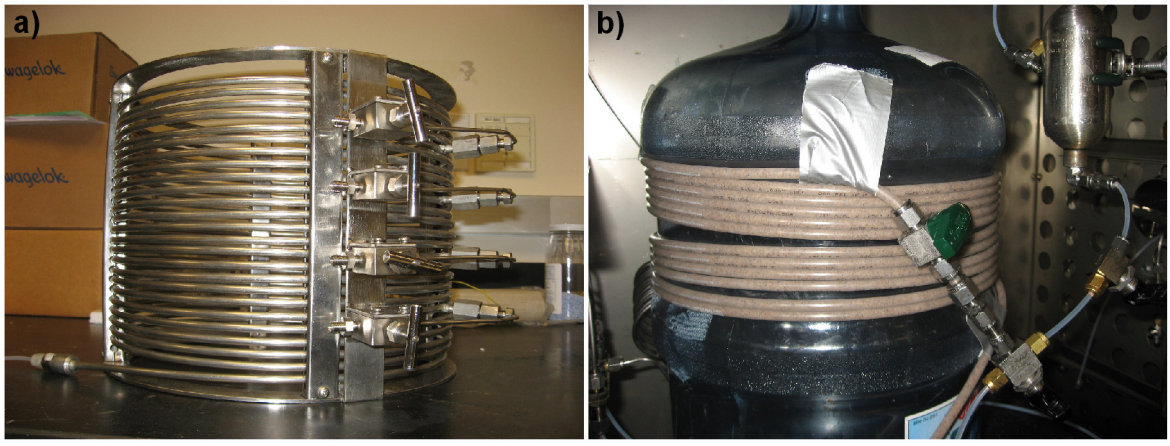

Figure 2.8: a) Stainless steel slim tube b) Polypropylene slim tube.

A 1000 cm polypropylene slim tube apparatus was also constructed for more immediate use at room temperature. The tube was packed with sand of 0.1 cm maximum diameter and fitted with filter paper, screens, and valves at each end. This polypropylene slim tube is pictured in Figure 2.8b.

2.3.3.1 Permeability measurements of stainless steel and polypropylene slim tubes packed with sand

Prior to nanofluid injection, porosity and permeability measurements were conducted. The calibration of pressure differential transducers is discussed. Measurement of the gas permeability in each stainless steel slim tube apparatus was also attempted, but could not be completed due to blockage within the tube itself. Four differential pressure transducers (Model DP15) manufactured by Validyne Engineering Corporation were calibrated for use in the slim tube packed with sand experiments. A standard pressure gauge was used to calibrate transducers with ratings of 12.5, 20, 50, and 125 psi. The signal sent by these transducers is measured in volt, and each was calibrated such that atmospheric pressure corresponds to 0 volt and its maximum pressure rating corresponds to 10 volts. The calibration plots for these transducers are shown in Figures 2.9 – 2.12.

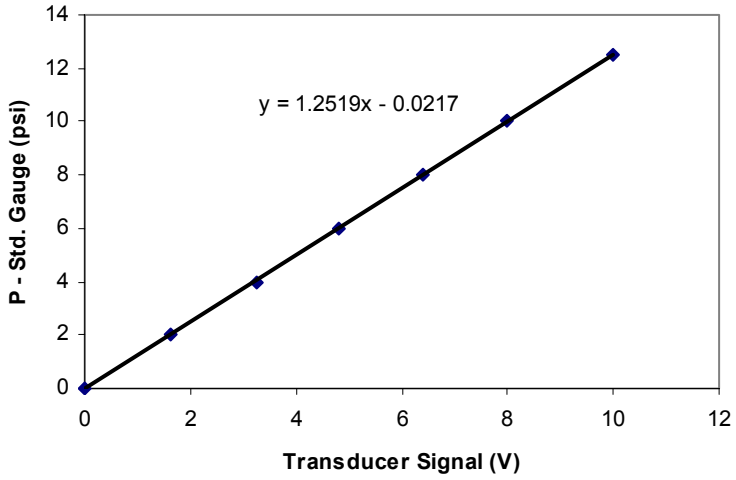

Figure 2.9: Calibration plot of 12.5 psi transducer

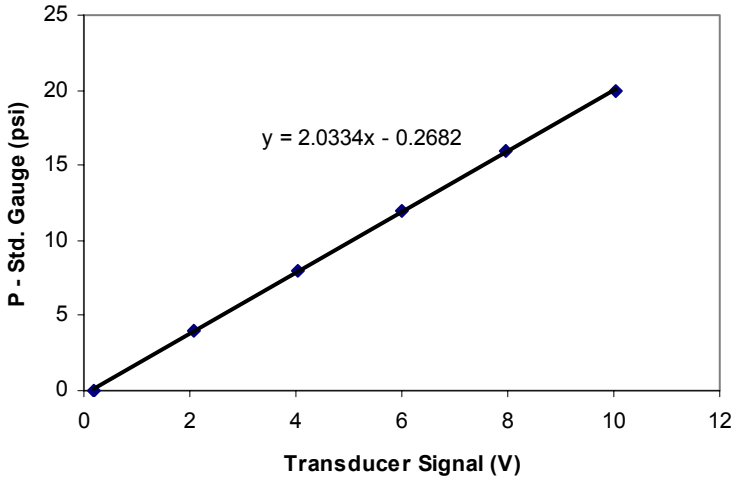

Figure 2.10: Calibration plot of 20 psi transducer

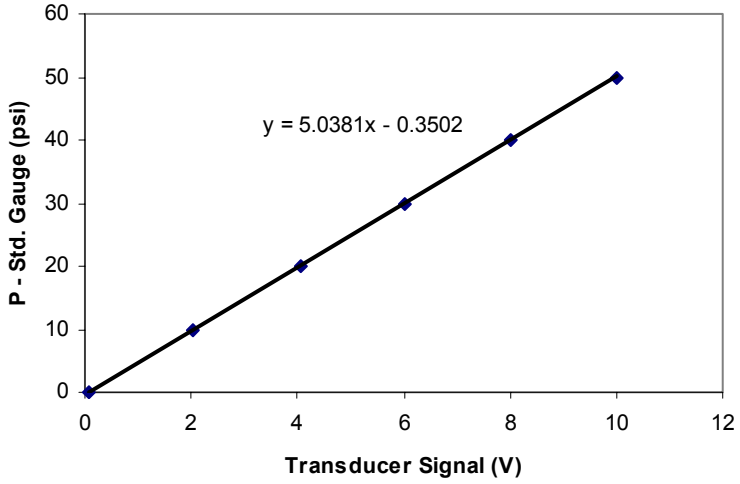

Figure 2.11: Calibration plot of 50 psi transducer

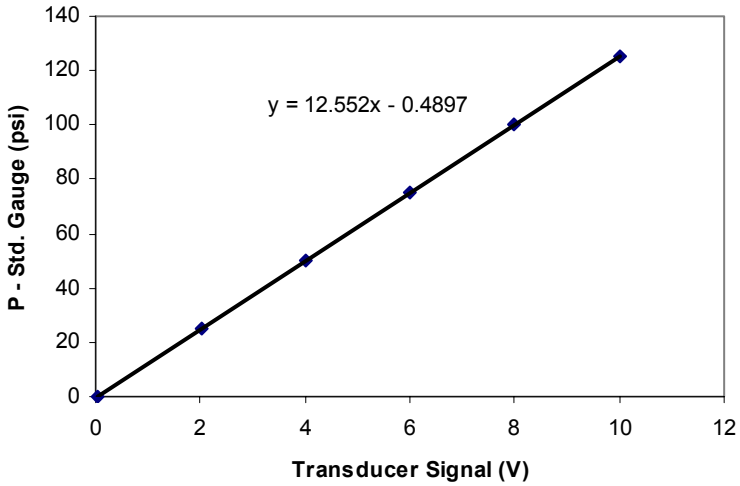

Figure 2.12: Calibration plot of 125 psi transducer

2.3.3.1.1 Permeability of stainless steel slim tube packed with sand

Gas permeability measurements in both stainless steel slim tubes were attempted using the apparatus shown in Figure 2.13. Nitrogen gas was directed to flow into the inlet of the coils. The inlet and outlet pressures were measured using differential pressure transducers of 125 and 50 psi ratings, respectively. The flow rates at the outlet were to be measured using a stop-watch and graduated cylinder (the standard method of measuring the flow rate).

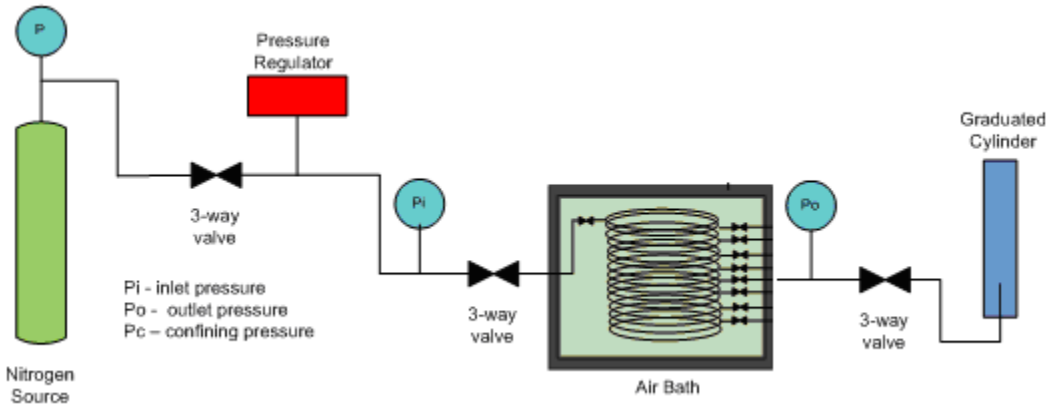

Figure 2.13: Schematic of the slim tube packed with sand apparatus for measuring gas permeability.

In order to conduct the permeability measurement, it is useful to have reasonable estimates of both the required inlet pressure and residence time corresponding to different gas flow rates. Preliminary calculations were performed using Darcy's law for compressible flow (Equation 2.1). The required inlet pressure corresponding to gas flow rate is shown in Figure 2.14 for three likely permeability values.

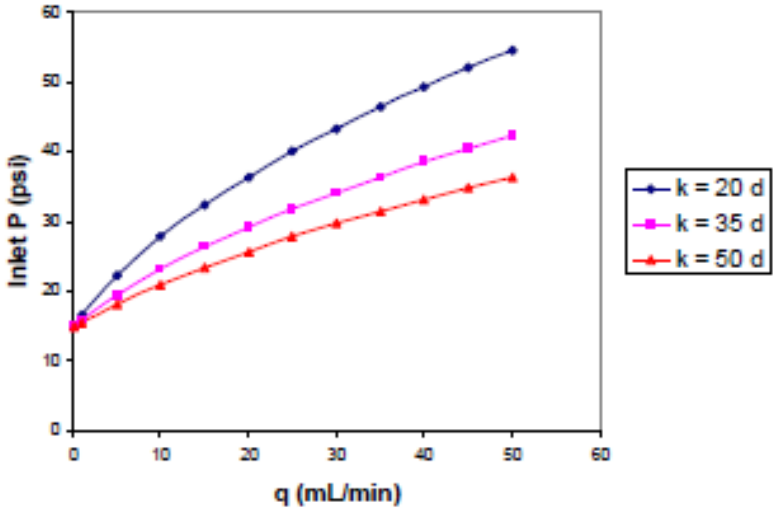

Figure 2.14: Required inlet pressure with varied gas flow rate.

The residence time corresponding to gas flow rate is shown in Figure 2.15.

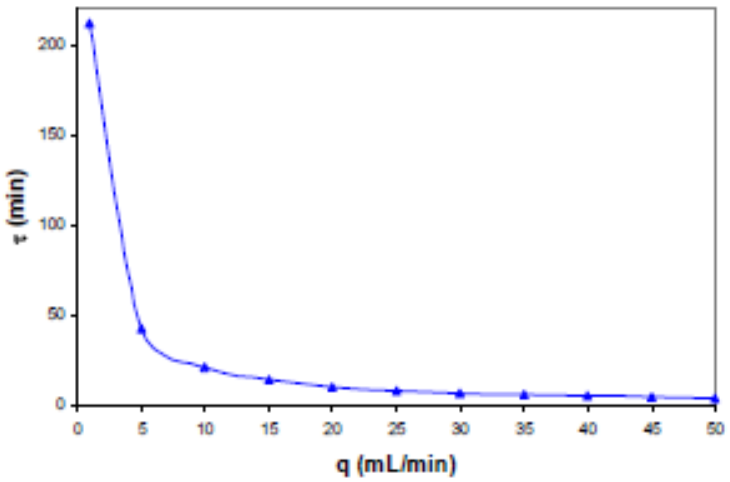

Figure 2.15: Residence time (t) with varied gas flow rate.

The permeability values of the stainless steel slim tubes could not be measured, because gas flow was not achieved at the outlet of either slim tube, even when pressures as high as 41 atm.g were applied. The effect of reversing the configuration so that the inlet was at the bottom and the outlet at the top was also investigated, with no outlet flow resulting. After checking each valve along the tube for flow, it was determined that only a 1000 cm section of one tube and a 500 cm section of the other were open to flow. Two more stainless steel slim tubes of the same length were then constructed and successfully tested for flow at the outlet. It should be noted that one of these new slim tubes was constructed without valves, as it is possible that the blockage in the first tubes was caused by the welding of the valve ports themselves.

2.3.3.1.2 Permeability of polypropylene slim tube packed with sand

The gas permeability was measured, and the Klinkenberg effect (gas slippage) was considered to evaluate the equivalent liquid permeability. The liquid permeability of the slim tube was then measured.

The apparatus used in the measurement of gas permeability was identical to the one shown in Figure 2.13 for the stainless steel slim tubes. The gas flowed in this experiment was nitrogen. The inlet and outlet pressures were measured using differential pressure transducers of 125 and 50 psi ratings, respectively. The flow rate at the outlet was measured using a stop-watch and graduated cylinder.

The gas permeability measurement was started by introducing nitrogen at different flow rates and inlet pressures. The average gas permeability was found to be around 50.2 darcy by applying Darcy's law for compressible fluids as given by Equation 2.1. The gas permeability as a function of the reciprocal of mean pressure is depicted in Figure 2.16. The average equivalent liquid permeability is 40.2 darcy.

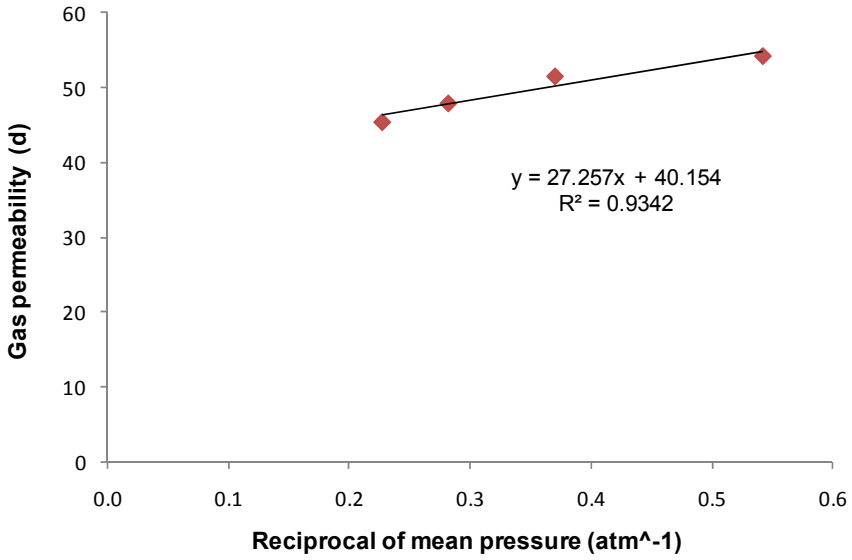

Figure 2.16: Gas permeability of the polypropylene slim tube packed with sand versus the reciprocal of mean pressure.

The liquid permeability was measured on the same tube. A schematic of the apparatus used in the measurement of liquid permeability is shown in Figure 2.17.

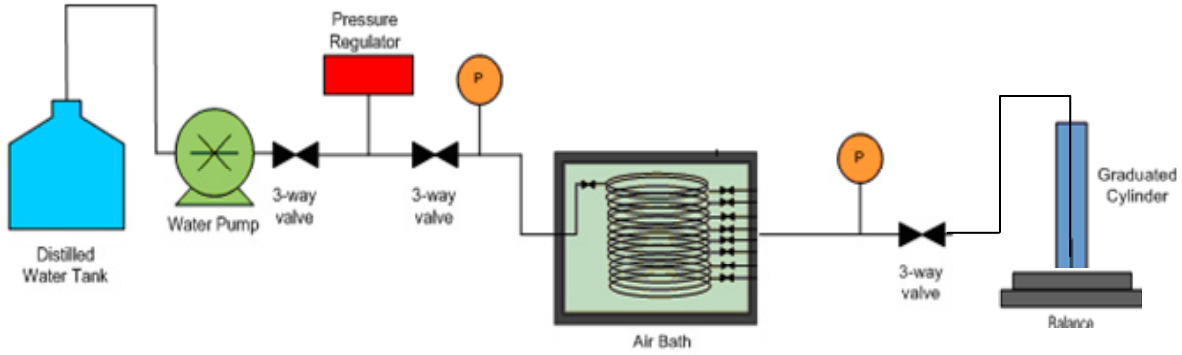

Figure 2.17: Schematic of slim tube packed with sand apparatus for liquid permeability measurement.

The slim tube packed with sand and related system were evacuated using a Welch Vacuum Pump for 4 hours at a vacuum pressure of about 25 millitorr to remove moisture. A column of pure water of known weight (W_d) was introduced to saturate the entire sand-packed and inlet tubes. The new water column weight (W_s) was then noted. The slim tube turned out to have a porosity of around 35.5% and a pore volume of 51.9 cubic centimeters. The porosity calculation is as follows:

$$\phi = \frac{V_p}{V_B} * 100 \tag{2.6}$$

$$V_{p1} = W_s - W_d \tag{2.7}$$

$$V_{p2} = \pi r_t^2 l_t \tag{2.8}$$

$$V_p = V_{p1} - V_{p2} \tag{2.9}$$

$$V_B = \pi r^2 l \tag{2.10}$$

where ϕ is the porosity in percentage, V_p and V_B are pore and bulk volumes of sand-packed tube in cubic centimeter, respectively. V_{p1} is the total of the sand-packed tube pore volume plus the inlet tubes dead volume in cubic centimeter. V_{p2} is the dead volume of inlet tubes in cubic centimeter. W_s and W_d are the weight of water column after and before saturation, in gram, respectively. r and l are the radius and length of the sand-packed tube in centimeter, respectively. r_t and l_t are the radius and length of the inlet tubes in centimeter, respectively.

Following the saturation, the liquid permeability was measured by injecting pure water using the water pump. Several flow rates were used to calculate the liquid permeability, ranging from 1 to 3 ml/min at different differential pressures. The average liquid permeability was found to be around 49.9 darcy. Darcy's law for horizontal flow was utilized to compute the permeability as given by Equation 2.5.

2.3.3.1.3 Permeability of polypropylene slim tube packed with glass beads

To investigate the mobility of nanoparticles in the absence of rock materials (such as clays), the nanoparticles were injected into a slim tube packed with glass beads. A 30 cm long polypropylene slim tube was constructed. The tube was packed with glass beads (Glasperlen 0.1 cm in diameter from B. Braun Biotech International) and fitted with screens and valves at each end. This polypropylene slim tube is pictured in Figure 2.18. The porosity was measured by the saturation method. The porosity and pore volume of the slim tube packed with glass beads were found to be approximately 46.8% and 2.39 cm^3, respectively. The permeability was estimated to be around 13 darcy.

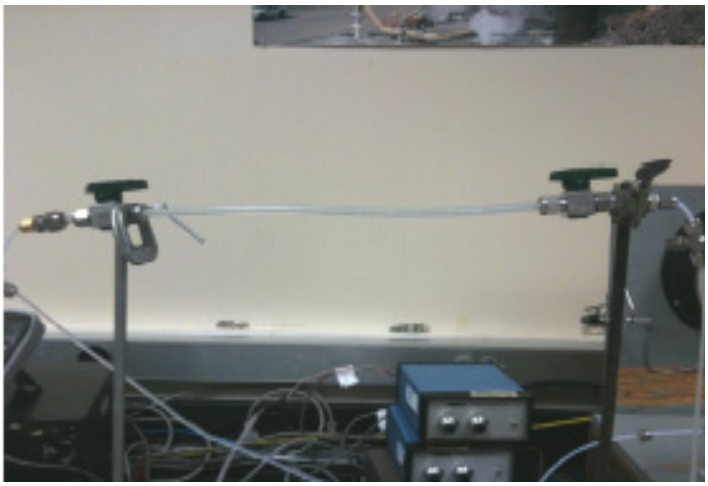

Figure 2.18: Polypropylene slim tube packed with glass beads.

2.4 NANOPARTICLES SYNTHESIS AND CHARACTERIZATION

Nanoparticles used in this study and ultimately in the reservoir need to be safe to handle and environmentally friendly. The particles should also be stable in suspension and disperse in solution. Moreover, the interaction affinity of such particles to the reservoir formation should be verified and the particles must not interact with rock matrix (Kanj et al., 2009).

The following sections provide some details of the characterization techniques used and nanoparticles synthesis.

2.4.1 Nanoparticles Characterization Techniques

In general, the quantity of the nanotracer produced at the sampling (exit point) should be sufficient to be recognizable and at concentrations above the lower detection limit of the devices used to analyze the effluent by at least factor of three. Characterization of the nanofluid prior to and after injection was carried out by various techniques. Dynamic Light Scattering (DLS) and Ultraviolet-visible Spectroscopy (UV-visible Spectroscopy) were used to detect the nanoparticles. Scanning Electron Microscopy (SEM) was also utilized to confirm the findings.

Characterization of the rock pore spaces following the injection was essential. Studying the nanoparticles morphology inside the sample was of equal importance. The objective was to understand the particle size distribution and how they arranged themselves within the porous medium (Kanj et al., 2009). To this end, SEM analyses were performed at different sections of the core samples (i.e. at the inlet, outlet and in the middle). A brief description of the characterization methods is incorporated in the following sections.

2.4.1.1 Dynamic Light Scattering (DLS)

DLS is a technique used to measure sizes of particles suspended in liquid. The technique measures the random motion of suspended particles resulting from the bombardment by surrounding solvent molecules. This movement is known as Brownian motion. When particles are illuminated with a laser, the scattered light intensity varies depending on the size of the particles (the smaller the particle, the further the distance it moves because of solvent molecule bombardment) hence their Brownian motion (Introduction to DLS, n.d.). These changes in light intensity are related to particles size using the Stockes-Einstein relationship given by:

$$d(H) = \frac{kT}{3\pi\eta D} \tag{2.11}$$

where $d(H)$ is hydrodynamic diameter, D is translational diffusion coefficient, k is Boltzmann's constant, T is absolute temperature and η is viscosity.

It should be mentioned that the particles size measured by DLS is the hydrodynamic diameter (how particles diffuse in a fluid). DLS assumes that the particles being measured have the same translational diffusion coefficient as spheres (Figure 2.19). Because the translational diffusion coefficient depends on various factors beside the particle core such as surface structure, concentration and the ion type of the medium, the reported size could be larger than the actual particle size (Introduction to DLS, n.d.). Therefore, SEM imaging was used here to confirm at least some of the measurements.

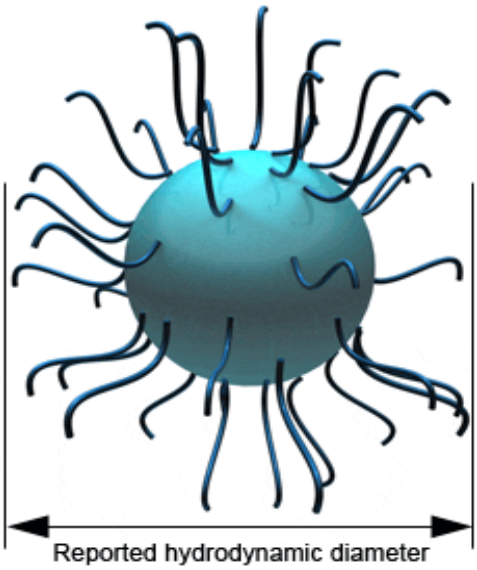

Figure 2.19: Measured hydrodynamic diameter by DLS (from malvern.com technical library).

DLS was utilized to determine the particle size and distribution of the injected nanofluid and the effluent samples. These measurements were performed using the Zetasizer Nano ZS device manufactured by Malvern instruments. This device can detect particles as small as 0.6 nanometer.

2.4.1.2 Ultraviolet -visible spectrophotometry

UV-visible spectrophotometry involves the spectroscopy of photons in the UV-visible region, which means that it deals with light in the visible, near-ultraviolet and near-infrared ranges. The spectrophotometer is the instrument used to measure the light intensity as a function of wavelength of light. The Beer-Lambert law is used to quantify the concentrations of absorbing species in solution (Wittung et al., 1994). The law states that the absorbance of a solution is directly proportional to the path length through the sample and the concentration of absorbing species in solution. The Beer-Lambert law is given by:

$$A = -\log_{10}\left(I / I_o\right) = \varepsilon c L \tag{2.12}$$

where A is the measured absorbance, I is the intensity of light passing through the sample, I_o is the intensity of light before it passes through the sample, L is path length through the sample, c is the concentration of absorbing species and ε is the molar absorptivity constant which is specific for each species and wavelength at particular temperature and pressure and has units of $AU / M * cm$.

Therefore, measuring the absorbance of the substances in solution and knowing the path length of the sample along with the absorptivity constant, the concentration of the substance can be calculated. It is worth mentioning that the Beer-Lambert law implies that there is an equal effect of the changes in concentration and path length. For example, dilution of the sample by a factor of 12 has the same effect on absorbance as reducing the path length from 12 to 1 millimeter.

Ultraviolet-visible Spectrophotometer was used to characterize the injected silver and iron oxide nanoparticles. The UV-visible absorbance spectra were measured at room temperature using a Shimadzu UV-1700 double beam spectrophotometer with a 12 mm square polystyrene cuvette. All samples had been sonicated prior to analysis to disperse the particles. Some samples were diluted with pure water before taking the spectra while others were analyzed without dilution.

2.4.1.3 Scanning Electron Microscopy (SEM)

Microscopy-based techniques provide a tool for the characterization of particle size, size distribution and morphology. A major advantage of microscopy-based technique is the capability to identify the particle shape (Jillavenkatesa et al., 2001). This is particularly important in the nanofluid injection experiments because it enables us to distinguish the injected nanoparticles from preexisting objects such as rock fines and debris. Scanning Electron Microscopy (SEM) generates images of the sample surface by scanning it with a high energy beam of electrons. Signals produced from the interaction between electrons and the sample surface provide detailed information about the sample topography. SEM enables the evaluation of the details at higher magnifications and resolutions and that makes it suitable for particle measurements in the submicron sizes.

The measurements were performed using a Philips FEI XL30 Sirion SEM instrument with Field Emission Gun source at the Stanford Nano Characterization Laboratory. As mentioned earlier, SEM imaging is useful to confirm the DLS measurements which are simpler and cheaper but do not distinguish between the particles other than by size. Moreover, SEM was used to study the location of nanoparticles inside the rock matrix and how they arrange themselves in the pore spaces. In this regard, cores used in preliminary nanofluid injection experiments were sliced at inlet, outlet and middle and prepared for SEM analysis.

2.4.2 Nanoparticle Syntheses

In this section, the syntheses of silicon dioxide (SiO_2), iron oxide (Fe_2O_3), coating of Fe_2O_3, tin-bismuth alloy nanoparticles will be discussed in detail.

2.4.2.1 Silicon dioxide (SiO_2) nanoparticles synthesis

The conditions for the preparation of monodisperse silica particles followed the study done by Bogush et al. (1988). The nanoparticle preparation was accomplished by the hydrolysis of tetraethyl orthosilicate (TEOS) in aqueous ethanol solutions containing ammonia. Initially, particle sizes in the range of 50-130 nanometers were targeted.

The correlation resulting from Bogush et al. (1988) was used as an engineering tool in the determination of single-sized particles. The expression was fitted to the experimental observations and written as:

$$d = A[H_2O]^2 \exp\left(-B[H_2O]^{1/2}\right) \tag{2.13}$$

with

$$A = [TEOS]^{1/2}\left(82 - 151[NH_3] + 1200[NH_3]^2 - 366[NH_3]^3\right) \tag{2.14}$$

and

$$B = 1.05 + 0.523[NH_3] - 0.128[NH_3]^2 \tag{2.15}$$

where d is the average diameter in nanometers and the concentrations of the reagents are in the units of mol/l (Bogush et al., 1988). Figure 2.20 shows the relationship between the particle diameter obtained from the correlation and the diameters obtained experimentally. Most of the data fall within the 20% deviation lines.

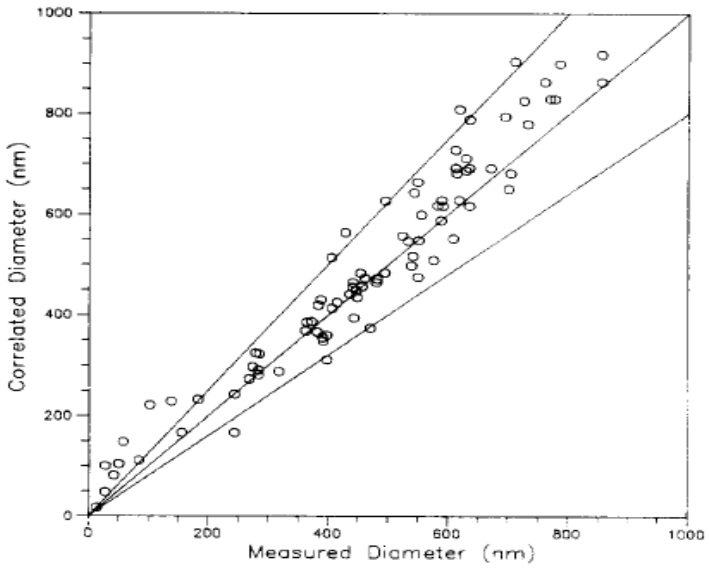

Figure 2.20: Relationship between model and experimental diameters (from Bogush et al., 1988).

The approach is to vary the concentration of water and ammonia while keeping the TEOS concentration constant. The dependence of the particle diameter calculated from the correlation between water and ammonia concentrations for a constant TEOS concentration of 0.17 mol/l is depicted in Figure 2.21.

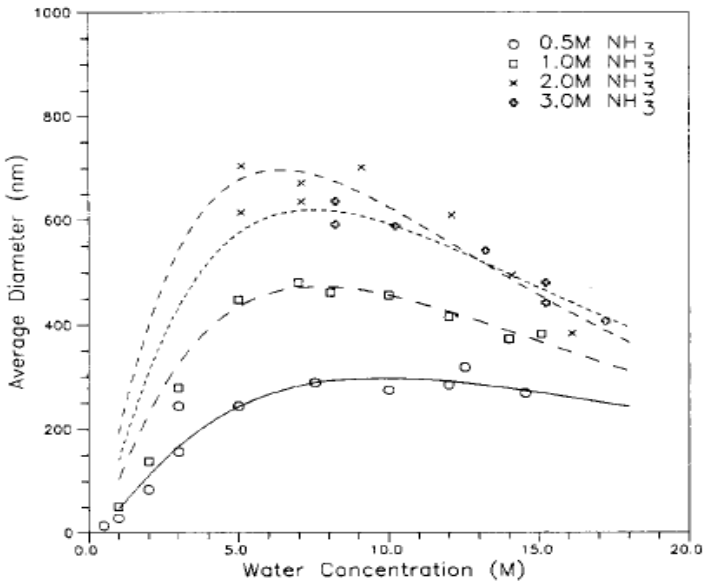

Figure 2.21: Average particle size as a function of water and ammonia concentrations with fixed TEOS concentration of 0.17 M (from Bogush et al., 1988).

2.4.2.2 Iron oxide (Fe_2O_3) nanoparticle synthesis

Iron oxide (Fe_2O_3) nanoparticles, known as hematite nanorice, were synthesized. Hematite was chosen for a number of reasons. First, it furthers the investigation of the feasibility of transporting nonspherical nanoparticles through porous media. The relatively simple synthesis process involved in making hematite nanoparticles also served as a valuable introduction to nanoparticle synthesis. Further, the surface chemistry of these nanoparticles can be modified, and there are known processes for coating hematite nanorice with other nanomaterials, which makes it a valuable candidate for temperature-sensitive applications (Connor, 2010). Hematite is also stable at reservoir conditions, and can be easily detected by its optical and magnetic signals. Finally, due to its unique rice-shaped geometry, it can be distinguished visually from natural minerals that may be present (using SEM).

Monodisperse hematite nanoparticles were synthesized using forced hydrolysis of solutions of ferric chloride, as suggested by Ozaki (1984). This hydrothermal synthesis was carried out by preparing 100 ml of aqueous solution of 2.0×10^{-2} M $FeCl_3$ and 4.0×10^{-4} M KH_2PO_4 and holding it at 100ºC for 72 hours (Wang, 2006). The precipitated nanoparticles were centrifuged and washed several times, then dispersed in 100 ml of water. These nanoparticles were found to be roughly 500 nm in length and 100 nm in diameter, resulting in an aspect ratio of 5:1.

2.4.2.3 Coating iron oxide (Fe_2O_3) nanoparticles with surfactants and silica

After early results indicated a difficulty in getting the iron oxide particles to pass through the core, it was postulated that their elongated shape caused them to have nonuniform surface potential that resulted in clustering of the particles. Because this would be a general property of rod-shaped particles, an investigation of this issue was initiated, first by coating the iron oxide nanoparticles with different materials to alter their surface charges.

Iron oxide nanoparticles were coated with SiO_2 and the surfactants triethanolamine (TEA) and polyvinylpyrrolidone (PVP) in order to modify the surface properties and determine if transport is limited by geometry or surface properties.

SiO_2 was particularly attractive as a coating because it had already been injected into a core and recovered successfully. To perform this coating, 0.3 ml of iron oxide nanofluid suspended in water was diluted with 4 ml of water and 20 ml of ethanol, a slight variation of the process suggested by Lu (2002). 0.5 ml of 30 wt % ammonia solution and tetraethyl orthosilicate (TEOS) were added while the solution was stirred magnetically, and the reaction continued for 3 hours at room temperature. The coated nanorice were separated from the reaction medium via centrifugation and suspended in water.

To coat the iron oxide nanoparticles with PVP, a 0.1 M solution of PVP in ethanol was prepared. Iron oxide nanofluid was then added, sonicated for 1 hour, and soaked overnight. The coated particles were cleaned by centrifugation three times at 6.5 krpm to remove excess surfactant. The TEA coating was identical, except a 0.1 M solution of TEA in water was used instead.

2.4.2.4 Tin-Bismuth alloy (Sn-Bi) nanoparticles synthesis

To begin investigating temperature-sensitive nanoparticles, the synthesis of Sn-Bi alloy nanoparticles was performed. The ideal geothermal temperature sensor should be nontoxic, able to pass through the reservoir, easily recovered if necessary, and should undergo an easily observable change in the temperature range of interest. One promising idea is a core-shell particle with an inert, magnetic core and a shell that undergoes decomposition or phase change. One of the reasons hematite has been investigated is because of its behavior under an applied magnetic field. This would make it an ideal material for the inert core if the transport barriers can be overcome. The shell could be a metal alloy with a low melting point (i.e. within the range of common geothermal temperatures). Sn-Bi alloys could potentially be used as sensors in the temperature range between eutectic melting point of the alloy (139°C) and the pure melting points of Bi and Sn (271°C and 232°C, respectively), as shown in Figure 2.22.

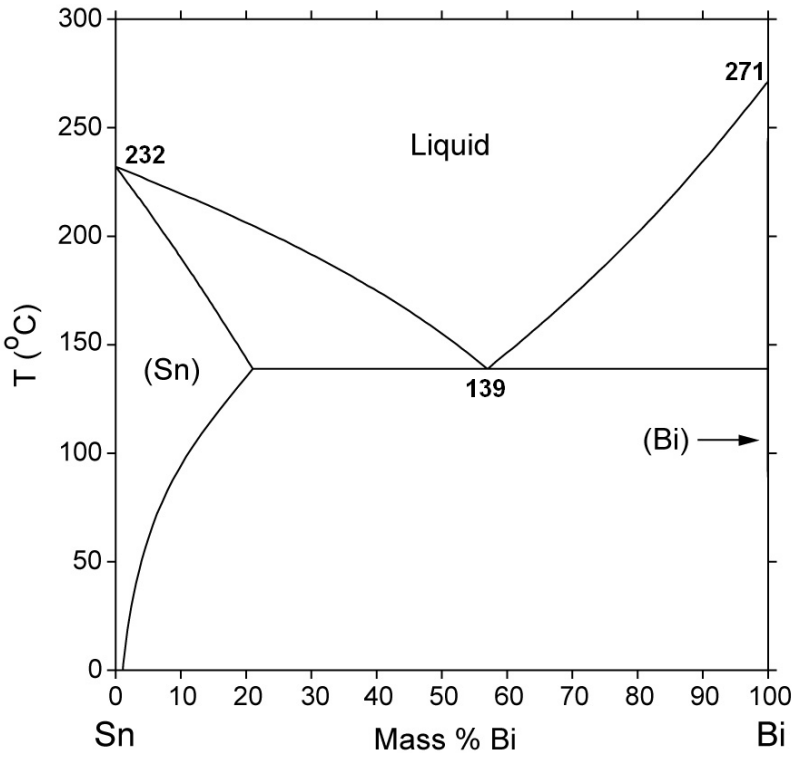

Figure 2.22: Phase diagram of Sn-Bi.
http://www.metallurgy.nist.gov/phase/solder/bisn.html

Moreover, the alloy is stable under ambient conditions and both metals are inexpensive and nontoxic in their metallic states (Connor, 2010). Finally, there are known processes for depositing Sn-Bi coatings, particularly on hematite core particles (Connor, 2010). The synthesis of Sn-Bi alloy nanoparticles is considered a preliminary in the creation of the envisioned core-shell nanosensors.

To perform the synthesis, Sn and Bi were melted together at the eutectic composition (~60 wt % Bi and ~40 wt % Sn). After it was cooled to room temperature, 100 mg of the alloy was sonicated in 10 ml of mineral oil, a slight variation of the sonochemical method suggested by Chen (2005). The VC-505 ultrasonic processor manufactured by Sonics and Materials, Inc. with a 0.5 in. replaceable tip was used. The sonicator was operated at 100 W (20% power) with a pulse setting of 1 s on, 10 s off. The sonicator is capable of operating at 500 W, but was not operated as such due to concerns that the organic solvent would break the replaceable tip. The mixture was cooled to room temperature and centrifuged. The alloy particles were washed several times with ethanol, and suspended in a solution of 100 mM PVP in ethanol.

An attempt was made to characterize the alloy particles using dynamic light scattering, but this was unsuccessful due to the presence of large particulates in the sample. This is most likely due to the low power setting used for the sonicator as a precaution. In order to

operate at higher powers in organic solvents, a solid probe was required, so a VC-505 with a 0.75 in solid probe was purchased. This ultrasonic processor is pictured in Figure 2.23. The synthesis will be repeated using this equipment at higher power.

Figure 2.23: VC-505 ultrasonic processor (Sonics and Materials, Inc.).
http://www.sonics.com/liquid-new-sheet/VC505-750.pdf

2.5 NANOPARTICLE INJECTION EXPERIMENTS AND RESULTS

Six main experiments were conducted. They serve as preliminary testing of the injection of various nanoparticles materials of different shapes through one or multiple porous media such as sandstone core samples and slim tubes packed with sand or glass beads. The following sections provide the details of the injection of silicon dioxide nanoparticles into slim tube packed with sand, iron oxide nanoparticles into Berea sandstone and slim tube packed with glass beads, iron oxide nanoparticles coated with surfactant into slim tube packed with glass beads and sliver nanoparticles into Berea sandstone. The heating experiment of the Sn-Bi alloy will also be visited. The characterization of each nanoparticle will also be discussed.

2.5.1 Silicon Dioxide Nanoparticle Injection into Slim Tube Packed with Sand

This section outlines the details of the injection of silicon dioxide nanoparticles into the long slim tube packed with sand (Figure 2.24). The objective of this experiment was to

investigate the transport and recovery of nanoparticles through a longer flow path. This is to approach actual field distances such as in interwell tracer testing. For that, the 1000 cm slim tube sand-packed flow apparatus was constructed. A schematic of the apparatus is shown in Figure 2.25. Nanofluid solution was contained in a pressure vessel downstream of the water pump. The nanofluid is injected into the slim tube with the aid of nitrogen pressure. The configuration also allows for injection of particle-free water, without interrupting the flow. This experiment did not consider the temperature effect, so was conducted at room temperature.

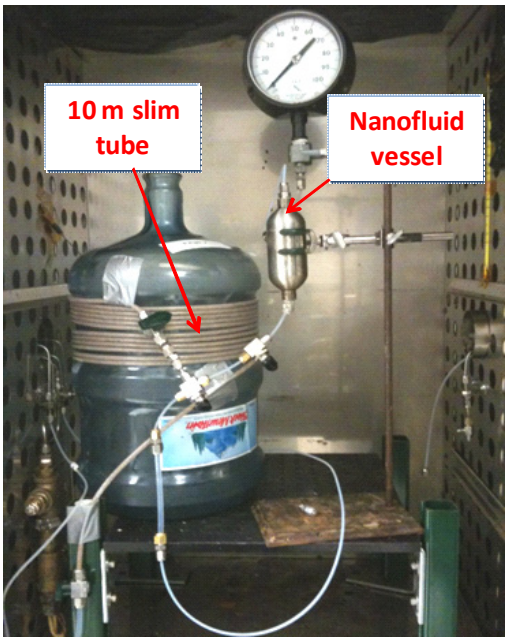

Figure 2.24: Polypropylene 10 meter slim tube.

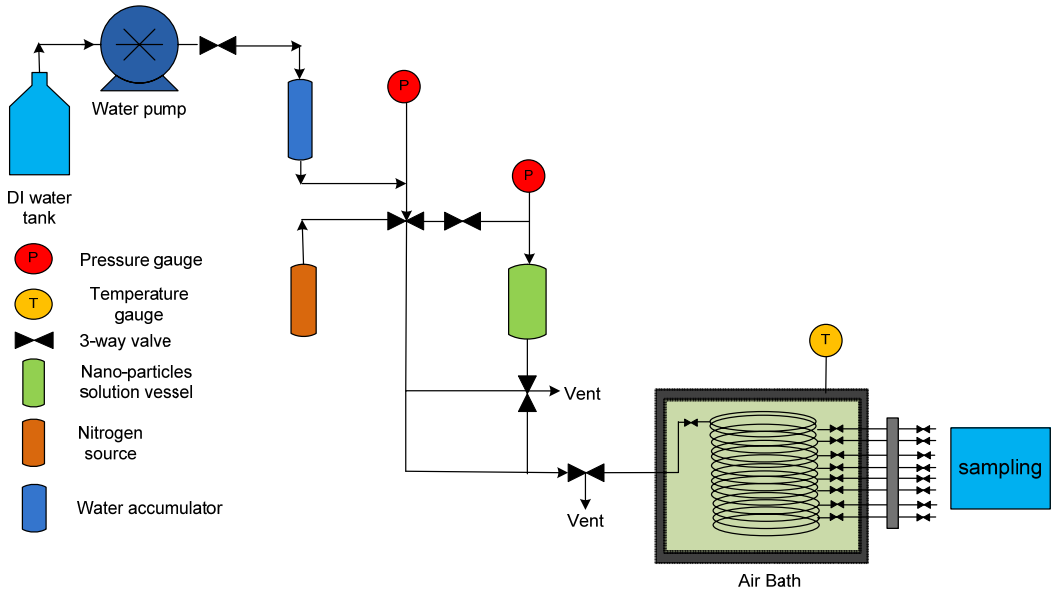

Figure 2.25: Experimental apparatus for nanofluid injection into sand-packed tube.

The silicon dioxide nanoparticles were detected at the effluent, confirming their transport (Figure 2.26). The permeability was unaltered during and after the injection of the nanofluid with minimal change of about ± 4 darcy. This can be seen in a plot of the permeability as function of pore volumes injected (Figure 2.27). Notice the high frequency of measurement points at the beginning of the post injection of pure water to capture any change in concentration of nanoparticles as more water was injected.

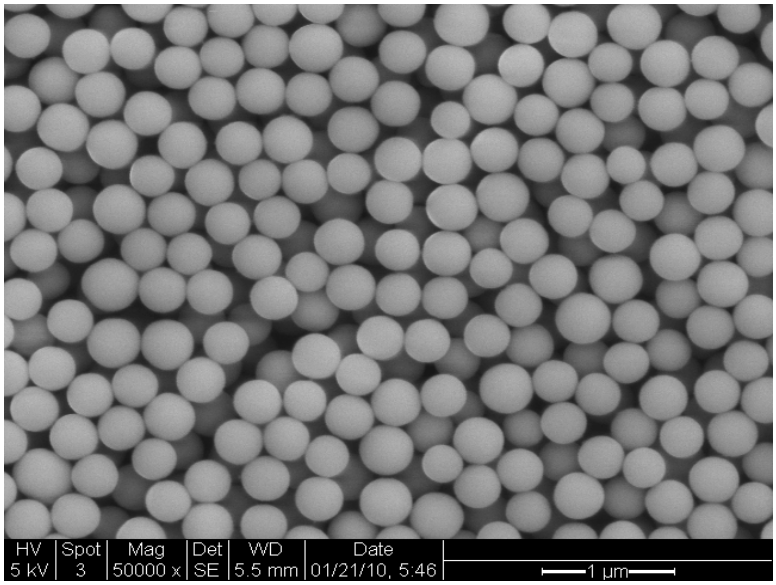

Figure 2.26: Effluent sample containing SiO_2 nanoparticles.

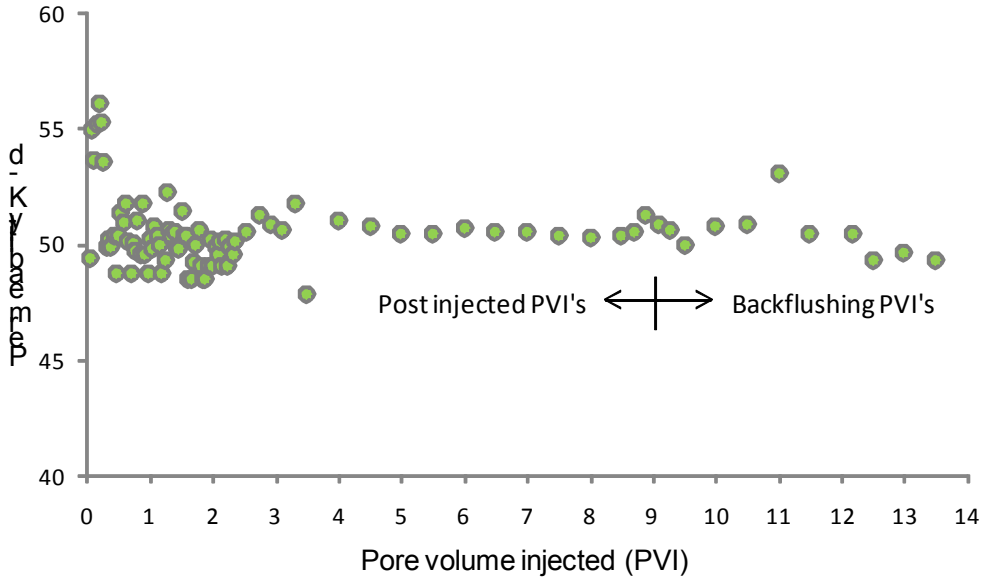

Figure 2.27: Permeability measurements during, after as well as during backflushing of the slim tube.

The SiO_2 nanoparticles injected had an average particle size of approximately 350 nanometers as demonstrated in Figures 2.28 and 2.29 by light scattering and scanning electron microscopy, respectively.

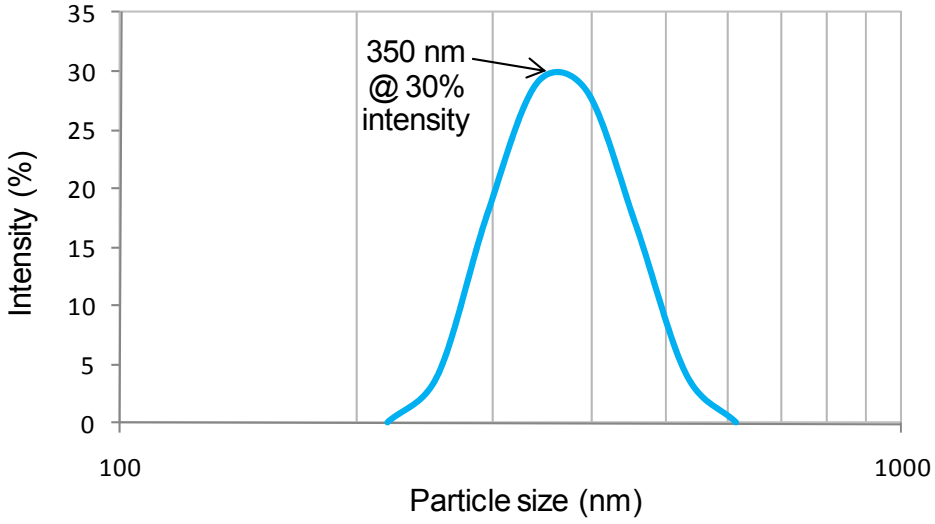

Figure 2.28: Particle size distribution by light intensity percentage of the influent injected.

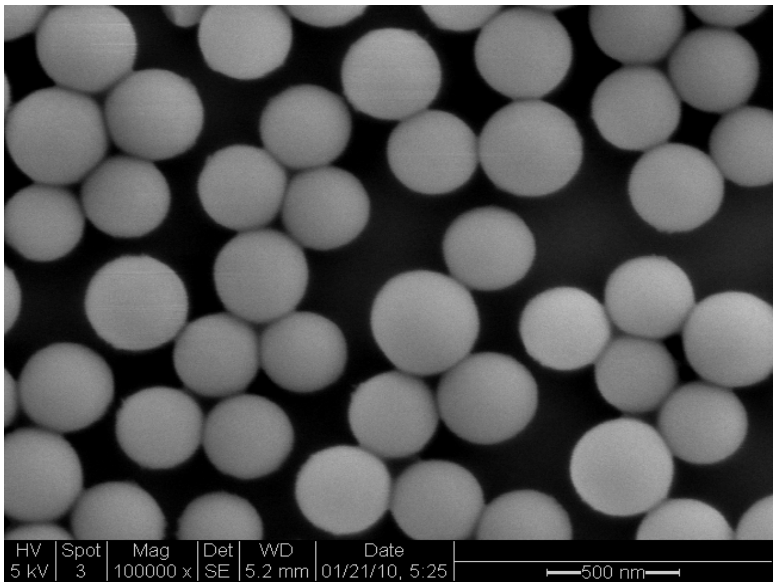

Figure 2.29: Monodisperse SiO_2 nanospheres of the influent with an average size of 350 nm.

Based on the light scattering measurements, the intensity of the incident light should remain unchanged for every particle size regardless of the sample concentration. In this case, the intensity of around 30% was measured at particle size of 350 nanometers of the original nanofluid injected (Figure 2.28). Therefore, effluent samples collected during post injection of pure water that contain any nanoparticle concentrations within the detection limits of the instrument used should have the same intensity for that particular particle size. The light intensity of effluent samples is plotted against post injected pore volumes (PVI) in Figure 2.30.

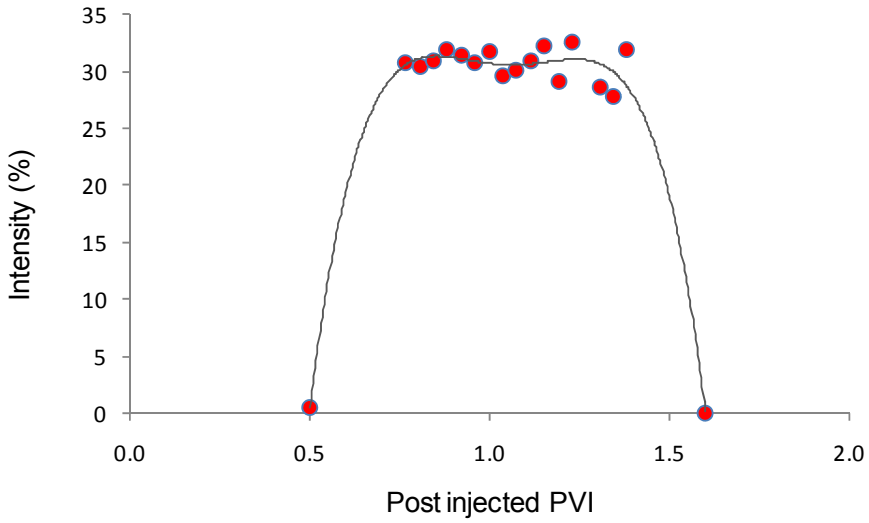

Figure 2.30: Intensity measurements of effluent samples.

It is evident from Figure 2.30 that the nanoparticles exist in the effluent samples with same intensity of the original silicon dioxide nanofluid influent (i.e. 30%) as depicted in Figure 2.28. The nanoparticles were identified following the post injection of about half of one pore volume of pure water and produced continuously until the bulk of these particles were displaced through the second pore volume. The increasing content of nanoparticles within that pore volume can be observed visually, as shown in Figure 2.31. Cloudy samples are more highly concentrated with SiO_2 nanoparticles compared to more transparent samples.

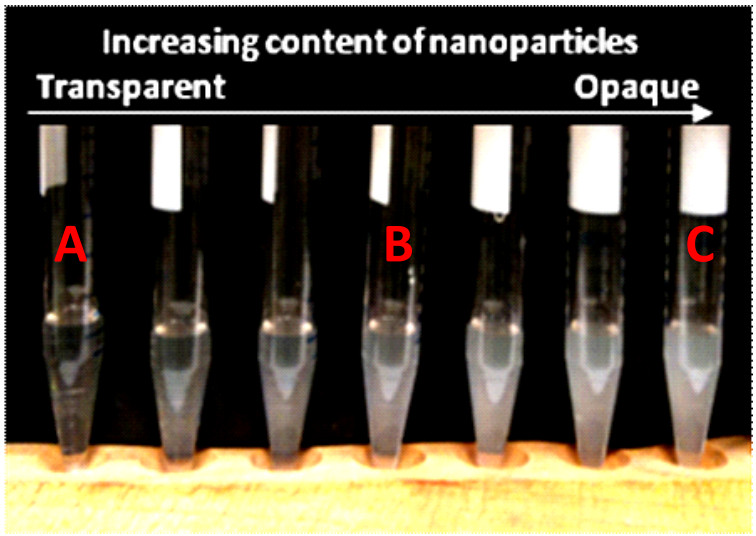

Figure 2.31: Visual characterization of effluent samples for their SiO_2 nanoparticles content based on color.

Scanning electron imaging confirmed the variation in the particle concentrations. A series of SEM images (Figure 2.32) were taken for samples A, B and C of Figure 2.31. These images show the difference in particle count or concentration clearly. Note that the volume of each sample was identical and micrographs were taken at the same magnification.

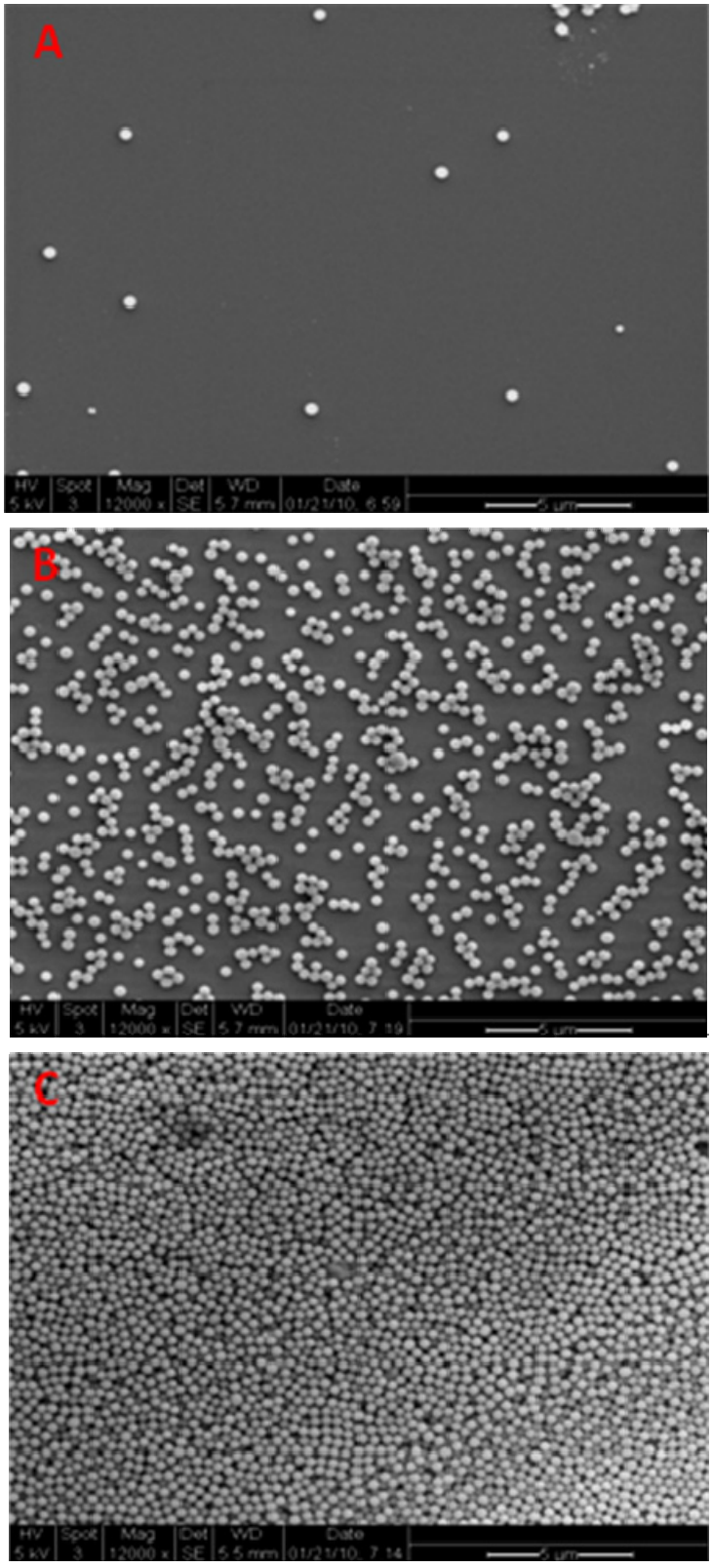

Figure 2.32: SEM images at sample A, B and C of Figure 2.31.

It is worth mentioning that not all SiO_2 nanoparticles were recovered following the second pore volume injected. A method to measure nanoparticle concentration has not been identified at this time. However, scanning electron imaging of selective samples within later pore volumes produced can indicate if they still exist. For instance, an effluent sample at the middle of the third post injected pore volume contained traces of the silicon dioxide nanoparticles, as opposed to another sample at the eighth pore volume, which was found to be free of any nanoparticles (Figure 2.33).

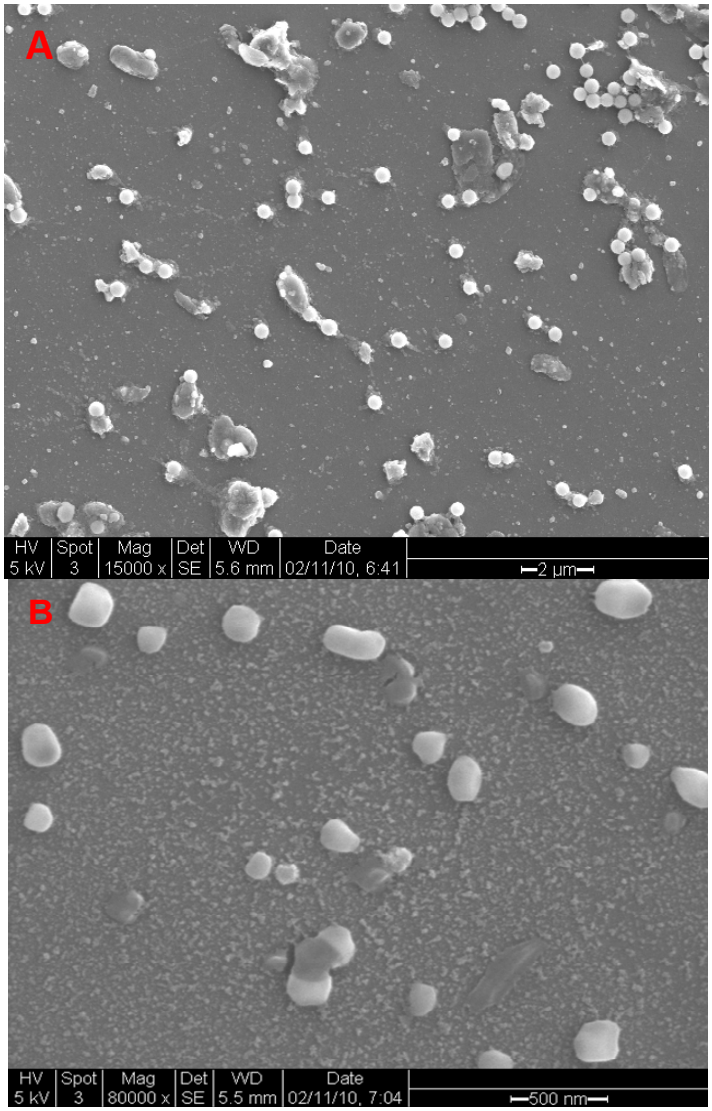

Figure 2.33: SEM image of effluent sample at the (A) third and (B) eighth post injected pore volumes.

It was realized that this finding did not imply the full recovery of all injected particles (but at least the mobile ones). The sand-packed slim tube was backflushed with few pore volumes in an attempt to determine whether there were any trapped nanoparticles, especially at the inlet side. An SEM image of the effluent from the first backflushed pore

volume is shown in Figure 2.34, where the spherical silicon dioxide nanoparticles can be seen clearly.

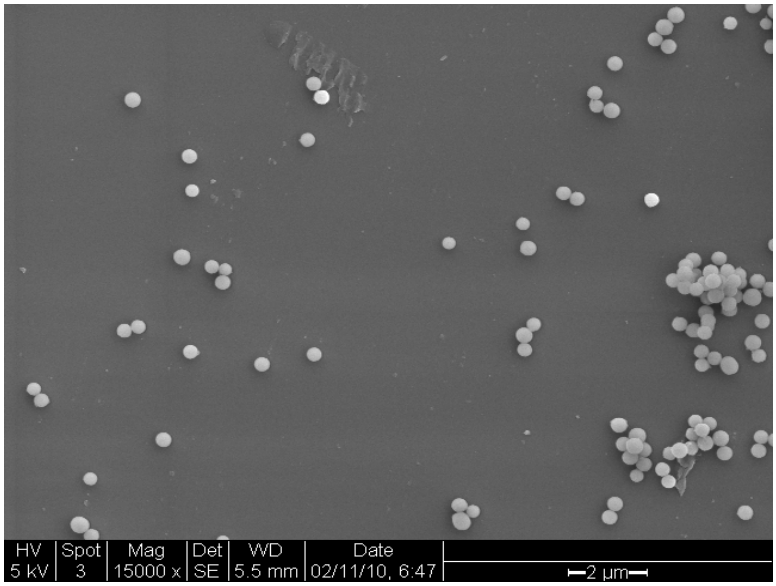

Figure 2.34: SEM image of effluent sample at the first backflushed pore volume.

Thus, it has been demonstrated that the spherically-shaped nanoparticles can be recovered following their injection, not only through short core plugs, but also through a longer flow path. In the experiments, the nanoparticles were transported without being trapped within the flow conduits.

2.5.2 Iron oxide (Fe_2O_3) nanoparticle injection into Berea sandstone and slim tube packed with glass beads

Two main experiments were conducted to serve as preliminary testing of the injection of nonspherical nanoparticles into Berea sandstone and into the slim tube packed with glass beads. The injection process and sampling strategies in both experiments were similar; however, they differ in some aspects such as total Pore Volume Injected (PVI), flow rates and sampling frequency. The following sections provide the specifics of each experiment.

2.5.2.1 Iron oxide (Fe_2O_3) nanoparticle injection into Berea sandstone

Injection of hematite (iron oxide Fe_2O_3) nanorice was conducted to investigate their flow through the pores of Berea sandstone. A schematic of the apparatus is shown in Figure 2.35. Nanofluid solution was contained in a pressure vessel downstream of the water pump. The hematite nanorice was injected with the aid of nitrogen gas.

This experiment did not consider the temperature effect, so it was conducted at room temperature. The nanofluid contained hematite nanoparticles of the size of 500 nm in length and 100 nm in diameter.

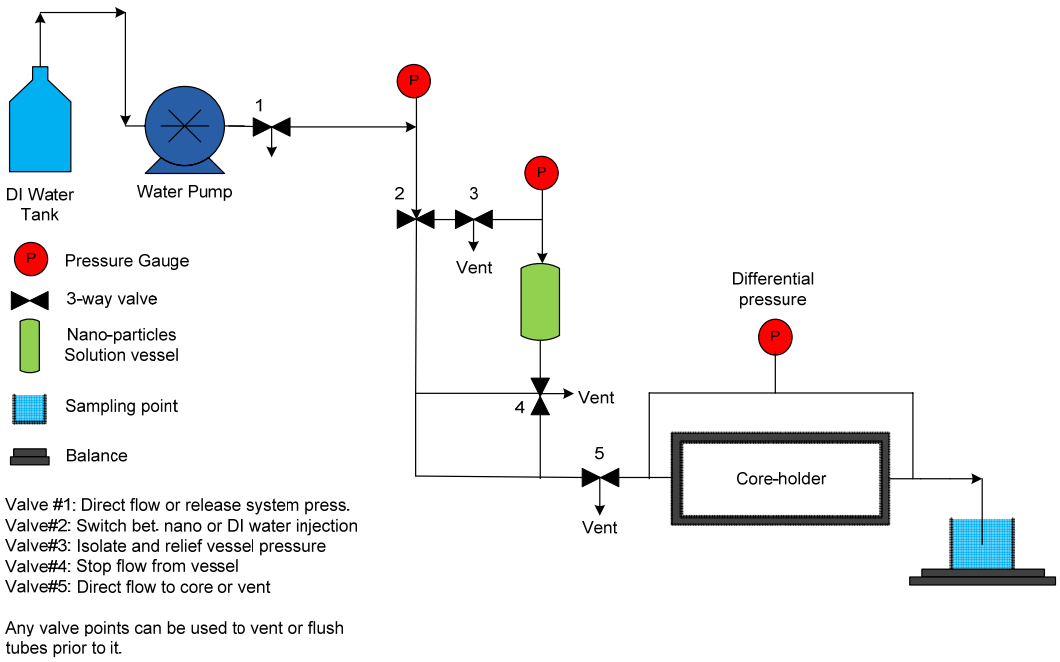

Figure 2.35: Experimental apparatus for nanofluid injection into Berea sandstone.

Prior to the injection of the nanofluid, the core was preflushed with pure water to displace as much rock fines and debris as possible. The nanofluid injection sequence was similar to the process suggested by Kanj et al. (2009). The sequence involved the injection of a specified volume of nanofluid followed by a continuous injection of pure water. In particular, 40% of the pore volume was injected. The hematite nanofluid was diluted 1:10 (i.e. 1 part hematite to 10 parts pure water).

Subsequent to the injection of the nanofluid, a continuous flow of pure water (post injection) was introduced. Specifically, 8 pore volumes of pure water were injected while the effluent samples were collected. The total time of the experiment was approximately 40 minutes. The injection was at the rate of 2 milliliter per minute at a differential pressure of about 6 psig. A total of 17 effluent samples were collected at the rate of 3 milliliter per sample. Not all these samples were analyzed but rather a selection was made to reduce the analysis time. In that regard, samples from the second and fourth post injected pore volume where analyzed by SEM.

2.5.2.2 Iron oxide (Fe_2O_3) nanoparticle injection into slim tube packed with glass beads

The hematite nanorice was also injected into slim tube packed with glass beads. The same experiment configuration (Figure 2.35) was used except that the coreflooding apparatus was replaced with a 30 cm long, 0.635 cm diameter polypropylene slim tube packed with spherical glass beads. The same hematite sample injected into the Berea sandstone was used in the glass beads injection experiment.

The slim tube was initially preflushed with several pore volumes using pure water. Then, three different injections of hematite nanofluid, each followed with continuous injection of

pure water (post injection) were conducted. In each experiment, the volume of hematite injected was about 40% of the pore volume (or 1 ml nanofluid). During the first injection, the hematite nanofluid was diluted (1 part of hematite to 10 parts pure water). In the second and third injections, the hematite nanofluid was not diluted. However, it was observed that the paper filters fitted at the tube inlet and outlet had clogged with the nanorice (Figure 2.36) and therefore the filters were removed prior to the third injection.

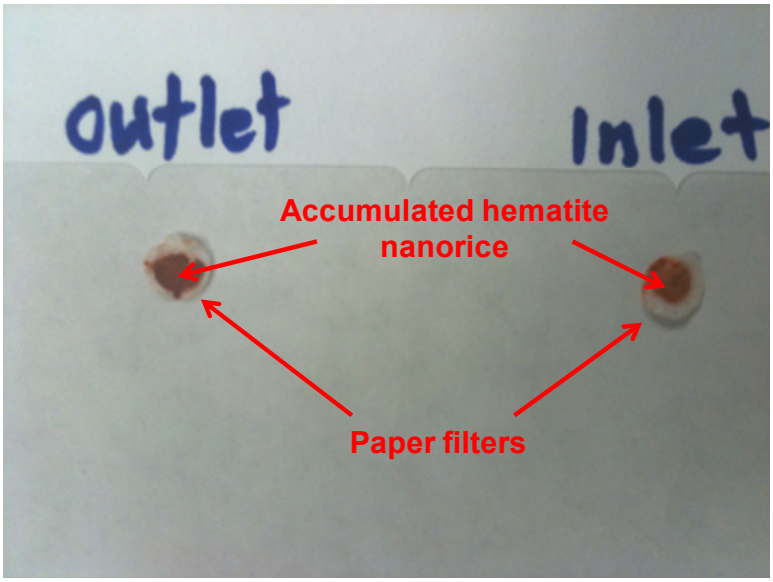

Figure 2.36: Paper filters fitted to inlet and outlet valves during hematite injection experiment. They were removed prior to the third injection of hematite.

2.5.3 Iron oxide (Fe_2O_3) nanoparticle injection results

Injection of hematite (iron oxide Fe_2O_3) nanorice was conducted to investigate their mobility within the pore spaces of Berea sandstone. The purpose was to investigate constraints imposed by the geometry and aggregation of the rod-like nanoparticles. The nanoparticles were found to be roughly 500 nm in length and 100 nm in diameter, resulting in an aspect ratio of 5:1 (Figure 2.37). By comparison, the hematite nanorice was at least an order of magnitude shorter than the silver nanowires injected previously. Thus, the nanorice was used to test the hypothesis made regarding the entrapment of the silver nanowires due to their geometry (length). Hematite nanorice was not identified in effluent collected during the injection into Berea sandstone. Light scattering, UV-visible spectroscopy and scanning electron microscopy were used to examine the effluent samples, in which no nanoparticles were detected. The hematite nanorice was, however, observed within the pores at the inlet side of the core as illustrated by SEM micrographs in Figure 2.38.

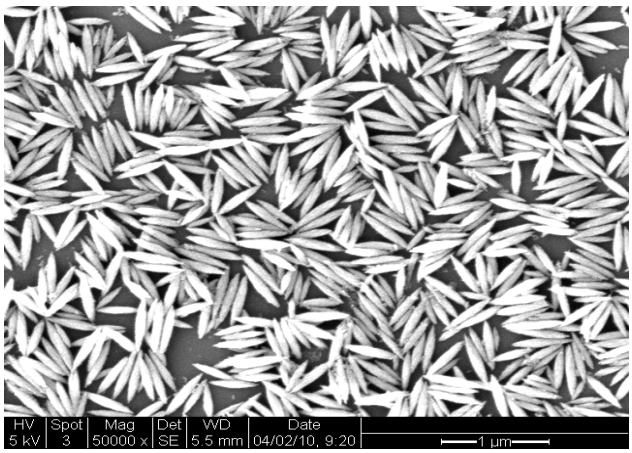

Figure 2.37: SEM image of hematite nanorice influent.

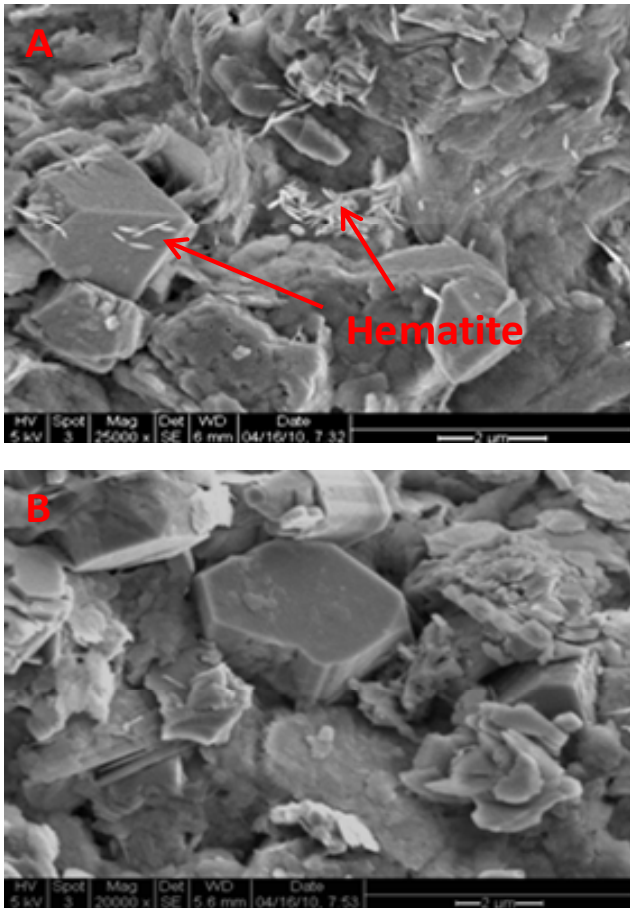

Figure 2.38: SEM imaging of Berea sandstone at (A) front side, (B) back side of the slice.

Similar to the analysis done for the silver nanowire injection, a thin slice of the core at the inlet was cut and SEM imaging was performed on both sides. Hematite nanorice was observed on the front face but not on the back face. Poulton and Raiswell (2005) reported that the natural spherical iron oxides nanoparticles (10-20 nm) in sediments tend to aggregate at the edges of clay grains, most likely because of their surface charge characteristics. Tipping (1981) and Tipping and Cooke (1982) observed that iron oxides

were negatively charged in fresh water while the edge of clay has positive charge which may explain the particle aggregation at that location. The micrographs in Figure 2.38 do not provide conclusive evidence of this interaction between the sandstone clays and the hematite nanorice. Nevertheless, this result suggested that there may be interaction between hematite nanorice and the sandstone core itself and/or among the nanorice in the form of particle aggregation. To investigate these two separate issues independently, the hematite was injected into the tube packed with glass beads. Spherical glass beads with a diameter of 0.1 cm were packed into a polypropylene slim tube with a diameter of 0.635 cm and a length of 30 cm.

Lecoanet et al. (2004) studied the mobility of several nanochemistry particulates in a column of tightly packed glass beads. Although all particles and the glass beads were negatively charged, the mobility of evaluated materials differed substantially from one another. For instance, 95% of injected fullerol particles were recovered rapidly as opposed to C_{60}, where less than 50% of the influent concentration was recovered.

In the case of hematite nanorice injection, both the glass beads and the hematite were negatively charged. A low particle count was observed using SEM imagery of several effluent samples at different post-injected pore volumes, as shown in Figure 2.39. The absorption of nanoparticles using UV-visible spectroscopy could not be measured due to their low concentrations, and thus the concentration of iron oxide nanoparticles in the effluent relative to the concentration in the influent also could not be determined. However, it was determined that in the absence of the clays and despite the fact that the porous medium and nanorice were carrying the same charge, the nanorice exhibited very low mobility.

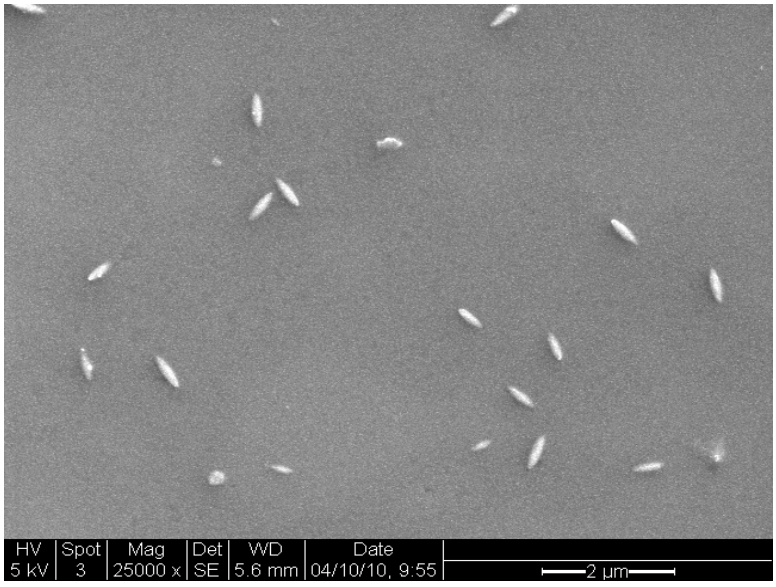

Figure 2.39: SEM image of effluent sample from the hematite injection through glass beads.

The actual glass beads from the inlet and outlet were also examined under SEM (Figure 2.40). Although the hematite nanorice recovery and/or mobility were low, they were able

to flow to the outlet (about 30 cm distance). The particles were also found aggregated on the surface or within the surface defects of the glass beads themselves.

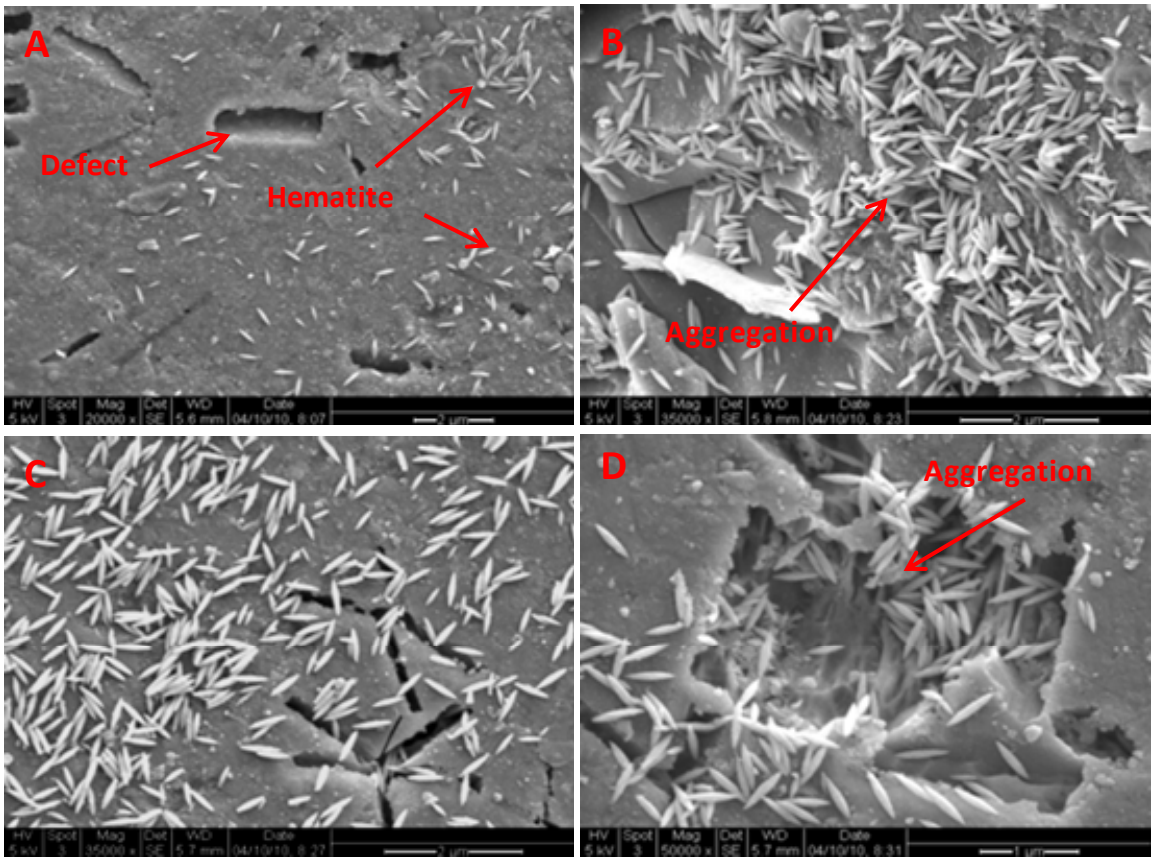

Figure 2.40: Hematite nanorice aggregation on the surface of glass beads at (A) and (B) inlet and (C) and (D) outlet side of the flow apparatus.

As can be observed in Figure 2.40, the anisotropic hematite particles have a tendency to aggregate in clusters. Lu et al. (2002) reported that iron oxide nanoparticles often aggregate in large clusters as a result of anisotropic dipolar forces. This aggregation could cause problems during transport through pore networks, such as bridging of the pores.

2.5.4 Coated iron oxide nanoparticles characterization and injection into slim tube packed with glass beads

In three different experiments, the iron oxide nanorice was coated with silica (SiO_2), the surfactants polyvinylpyrrolidone (PVP) and triethanolamine (TEA). The details of coating the iron oxide with the surfactants (PVP, TEA) or SiO_2 can be found in the Section 2.4.2.3 of this report. The uncoated nanorice exhibited very low mobility during their injection through the slim tube packed with glass beads which may be attributed to their geometry and/or surface characteristics. To further investigate if the surface charge was limiting their flow, the nanorice was coated with the surfactants or silica to modify their surface charge.

2.5.4.1 Characterization of coated iron oxide

Coated iron oxide particles were characterized in terms of size, surface charge (zeta potential) and pH using SEM imaging, zeta potential analysis and pH meter, respectively. The original iron oxide nanoparticles were 500 nm in length and 100 nm in diameter. Surface charge and pH measurements are summarized in Table 2.2. The reported zeta potentials are the average of three sets of measurement with standard deviation less than 2.

Table 2.2: Zeta potential and pH level for original and coated iron oxide nanoparticles.

Sample	**Average zeta potential (mV)**	**pH**
Original Hematite	+59.3	3.3
Hematite-SiO_2	-32.4	5.56
Hematite-PVP	-9.5	4.82
Hematite-TEA	+18.9	4.5

Note that there were three identical iron oxide samples each coated with different material. It was evident from the surface charge measurements that the coating materials altered the surface charge of the original iron oxide nanorice. The original (uncoated) iron oxide nanorice carries a high positive charge of 59.3 mV with low pH of 3.3 compared to the samples coated with silica (negative 32.4 mV and 5.56 pH) and PVP surfactant (negative 9.5 mV and 4.82 pH). The iron oxide coated with TEA surfactant resulted in moderately positive charge of about 18.9 mV. The zeta potential distribution of original and coated iron oxide nanoparticles can be depicted in Figure 2.41.

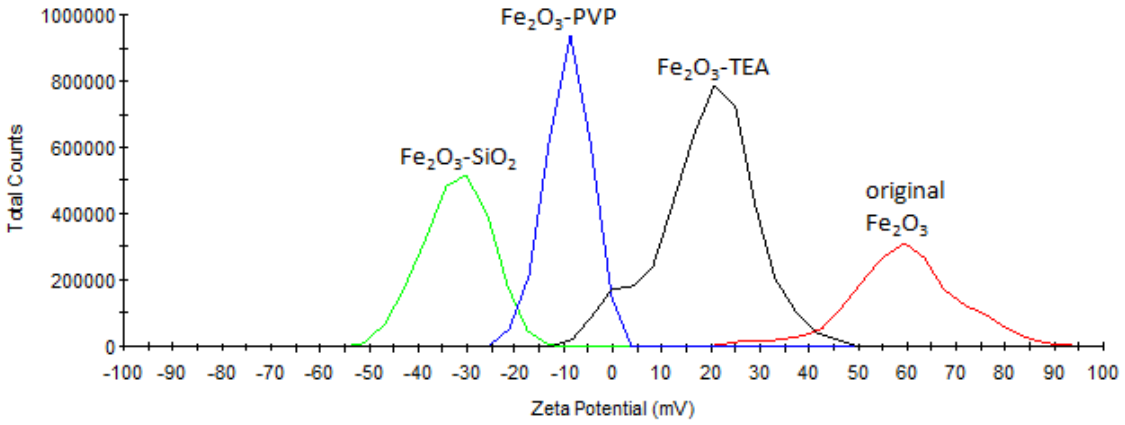

Figure 2.41: Zeta potential distribution of coated and uncoated iron oxide nanoparticles.

The glass beads used as the porous medium carry a negative charge. So it is of interest to inject particles that carry the same type of charge (i.e. negative charge), as similar charges repel and should prevent particle attachment to the glass beads. Based on this, the iron oxide nanoparticles coated with TEA surfactant were not selected for injection.

From the surface charge point of view, the iron oxide nanoparticles coated with SiO_2 were a very attractive candidate. They carry the highest negative surface charge among the three samples. Figure 2.42 shows the zeta potential distribution of silicon dioxide, iron oxides and silicon coated iron oxides. The peak of the distribution of the coated iron oxide nanorice is positioned between the peaks of the silicon dioxide and iron oxide.

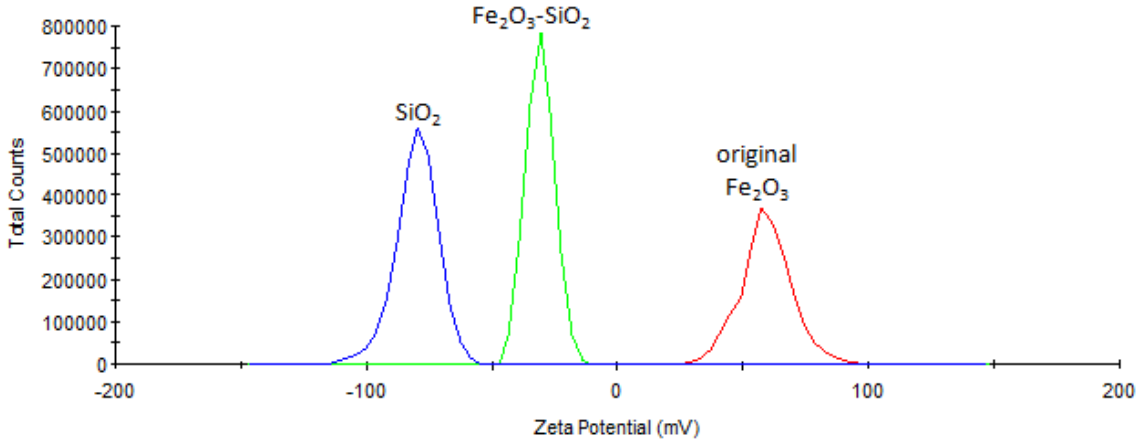

Figure 2.42: Zeta potential distribution of silicon only, iron oxide only and iron oxide nanoparticles coated with silica.

SEM imaging (Figure 2.43) showed that the coated iron oxide nanorice have a uniform SiO_2 coating of about 50 nm. As a result, the size of the iron oxide nanorices changed from 500 nm and 100 nm to 600 nm and 200 nm in length and diameter, respectively. It was also observed that the nanorice did not retain their original spindle-like shape with sharp edges (Figure 2.43 B).

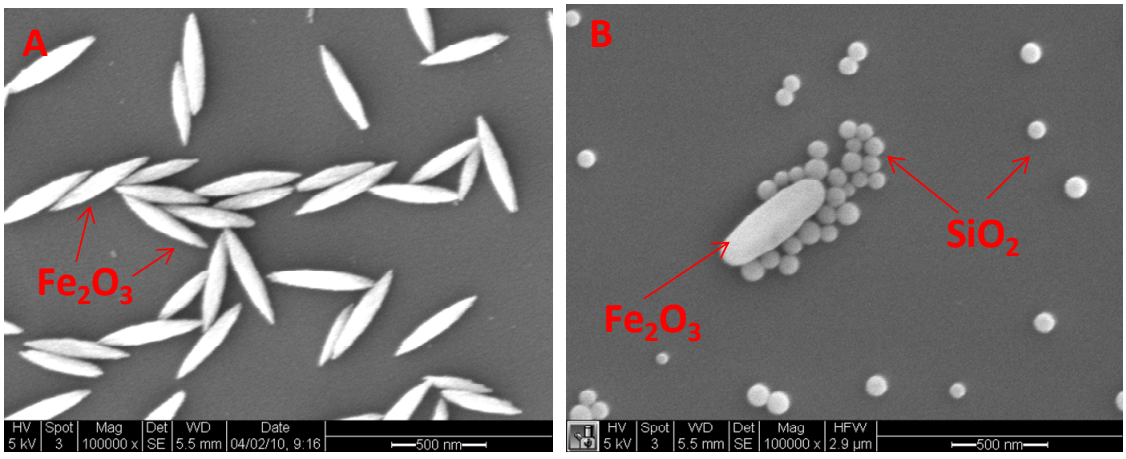

Figure 2.43: Iron oxide nanoparticles (A) before SiO_2 coating, (B) after coating with SiO_2. Coated sample did not retain its spindle-like shape as a result of the 50 nm SiO_2 coat.

Further evaluation of the nanorice coated with silica showed that the SiO_2 nanoparticles (about 100 nm in diameter) were dominating the sample. There were more SiO_2 nanoparticles than Fe_2O_3. The existence of excess SiO_2 nanoparticles resulted from the coating process. SEM image in Figure 2.44 is an example. Attempts to separate the silicon dioxide nanoparticles have not been successful and thus this nanofluid sample was not injected into the glass beads packed tube.

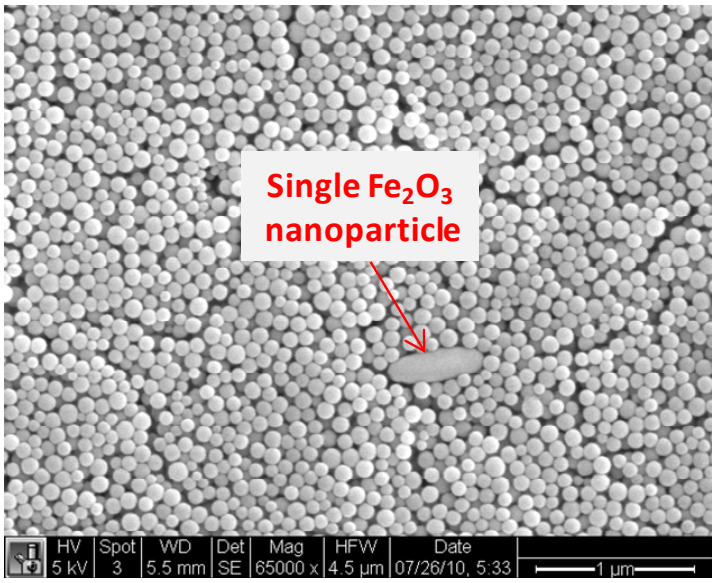

Figure 2.44: SEM image showing single hematite nanorice among the dominating silicon dioxide nanoparticles.

It was concluded that the iron oxide nanoparticles coated with SiO_2 and surfactant TEA were inappropriate for injection. However, iron oxide coated with surfactant PVP retained suitable characteristics in that it carried negative surface charge of 9.5 mV (Table 2.2). To coat the iron oxide with PVP, a 0.1 M solution of PVP in ethanol was prepared. Iron oxide nanofluid was then added, sonicated for 1 hour, and soaked overnight. The coated particles were cleaned by centrifugation three times at 6.5 krpm to remove excess surfactant.

2.5.4.2 Iron oxide (Fe_2O_3) nanoparticles coated with surfactant (PVP) injection and results

The iron oxide nanorice coated with PVP surfactant was injected into the slim tube packed with glass beads. A schematic of the apparatus used is depicted in Figure 2.45.

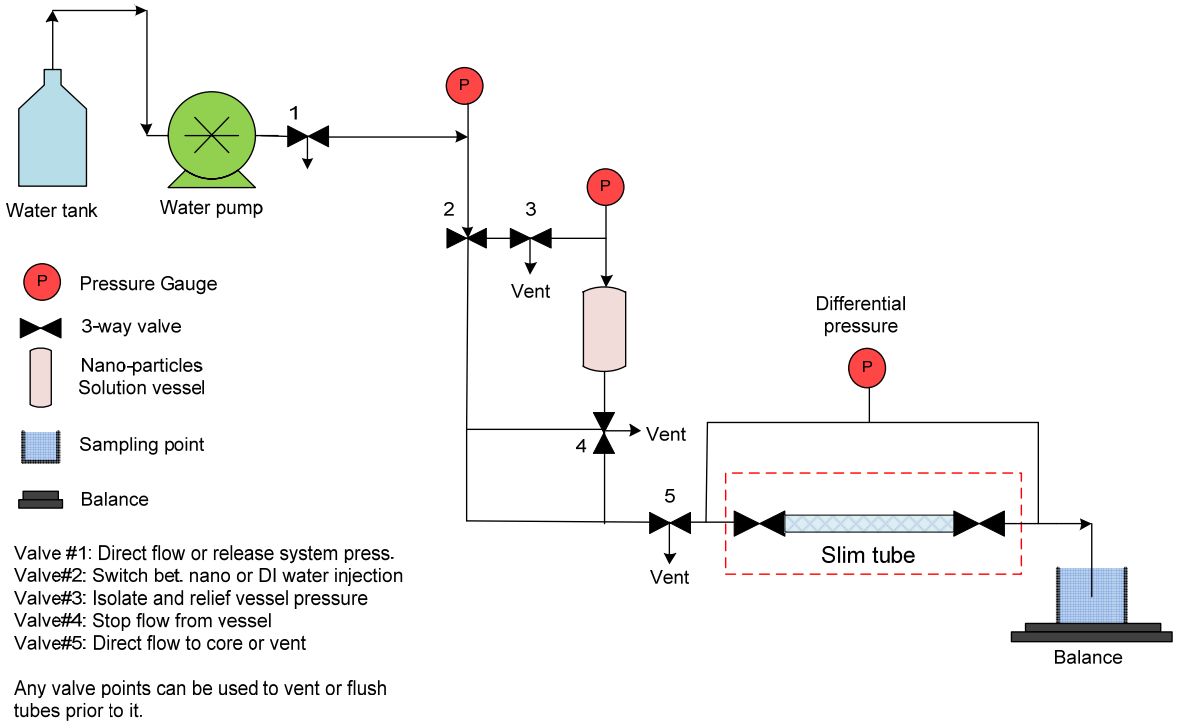

Figure 2.45: Experimental apparatus for nanofluid injection into glass beads packed tube.

The slim tube was initially preflushed with several pore volumes using pure water. Then, one pore volume of the iron oxide nanofluid was injected at differential pressure of about 0.14 atm. Following the nanofluid injection, 10 pore volumes of pure water was post injected at rate of 0.5 ml/min and eight effluent samples were collected. The permeability was not altered during or after the injection of the iron oxide.

In order to determine whether the transport of hematite nanorice was limited by their surface characteristics, hematite was coated with SiO_2 and the surfactants TEA and PVP to modify its surface properties. Among all, hematite coated with PVP was selected for injection as outlined in Section 2.5.4.1. Effluent samples at the first and second pore volume injected as well as the actual glass beads from the inlet and outlet were examined under SEM. The coated hematite was neither detected at the effluent samples nor at the glass beads. The sample injected was diluted and perhaps there were not sufficient nanorice. Therefore, this injection will be repeated with a more concentrated sample to further evaluate this finding.

2.5.5 Spherical silver nanoparticles characterization and injection results

The objective of this experiment was to investigate the transport and recovery of spherical silver nanoparticles through the pores of Berea sandstone. Initial testing with silver nanomaterial was conducted with the injection of silver nanowires into Berea sandstone. The goal was to investigate the transport of a wire-like nanoparticle and investigate experimentally if nanoparticles shape would cause any complication to the flow of

particles. The silver nanowires were not detected in the effluent and were found trapped at the inlet face within the pore spaces of the core rock. To test if the transport was limited by their material or shape, spherical silver nanoparticles were injected. In addition, the spherical silver nanoparticles injection serves as a preliminary testing of spherically shaped metal alloy (Tin-Bismuth) particles which might be used as temperature sensors in geothermal reservoirs.

2.5.5.1 Characterization of silver nanoparticles

Silver nanoparticles were characterized in terms of size, surface charge (zeta potential), light absorption and pH levels using SEM imaging, zeta potential analysis, UV-visible spectrophotometry and pH meter, respectively. The particle size was around 40 nm ±10 (Figure 2.46). The silver nanoparticles synthesis is a protocol adapted from Kim et al. (2006).

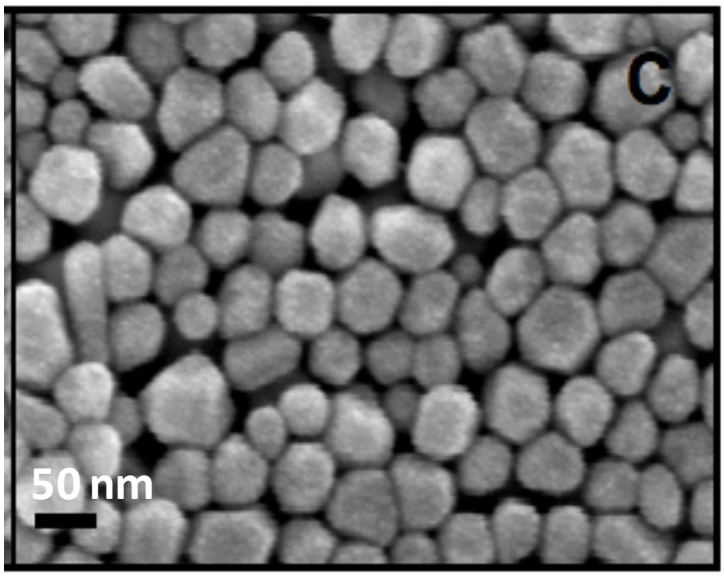

Figure 2.46 : SEM image of the silver nanoparticles.(Levard, personal communication)

The silver nanofluid sample volume was 20 ml with concentration of 1 g/l. the sample was sonicated for about 10 minutes using a Branson 2510 Sonicator prior to dilution. Then the nanofluid was diluted one part of silver nanofluid into two parts of pure water. The final concentration used in the injection experiment was 0.5 g/l.

The average zeta potential of the diluted silver nanoparticles sample was measured and found to be approximately negative 17 mV with standard deviation less than 2. The pH level was around 7.9. The zeta potential distribution of the silver nanoparticles is illustrated in Figure 2.47.

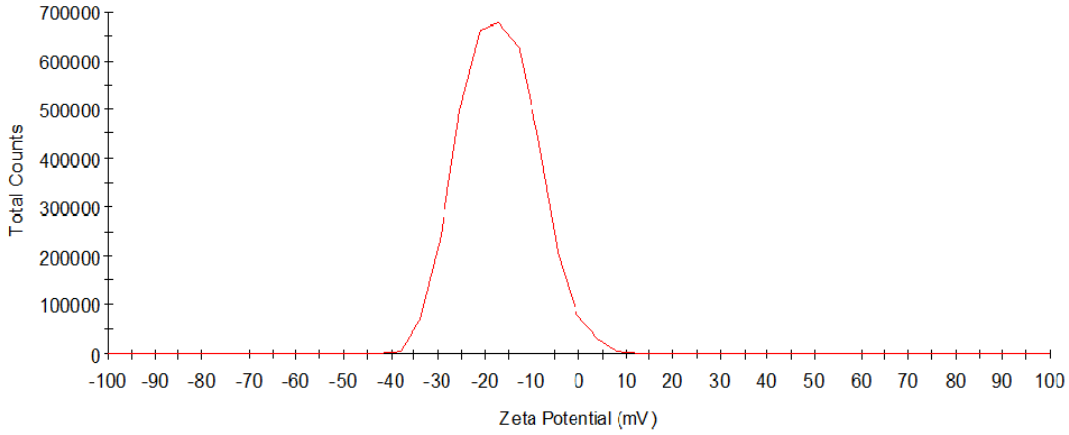

Figure 2.47: Zeta potential distribution of the silver nanoparticles.

UV-visible spectrophotometry was used to measure the absorption of the silver nanoparticles in effluent samples and hence their concentrations. This is an essential step as it enables us to construct the tracer return curve of concentrations verses volume injected.

Therefore, measuring the absorbance of the substance in solution and knowing the path length of the sample along with the absorptivity constant, the concentration of that substance can be calculated. Due to the difficulty in obtaining the absorptivity constant, it is common to determine the concentrations by constructing a calibration curve. This avoids having to rely on a value of the absorptivity or the reliability of Beer's Law. The calibration curve is accomplished by making few dilutions, each with accurately known concentration. It is important to ensure that those concentrations bracket the unknown concentrations under investigation. For each dilution, the absorbance is measured and plotted against the sample concentration. This is the calibration curve.

The original silver nanofluid was diluted one part of nanofluid to 100, 150, 200, 250, 300, 400 and 500 parts of pure water. Then, the absorbance spectra were measured at room temperature using a Shimadzu UV-1700 double beam spectrophotometer with a 12 mm square polystyrene cuvette. All samples had been sonicated prior to analysis to disperse the particles. The optical (absorbance) signatures of the diluted silver nanofluid samples are shown in Figure 2.48.

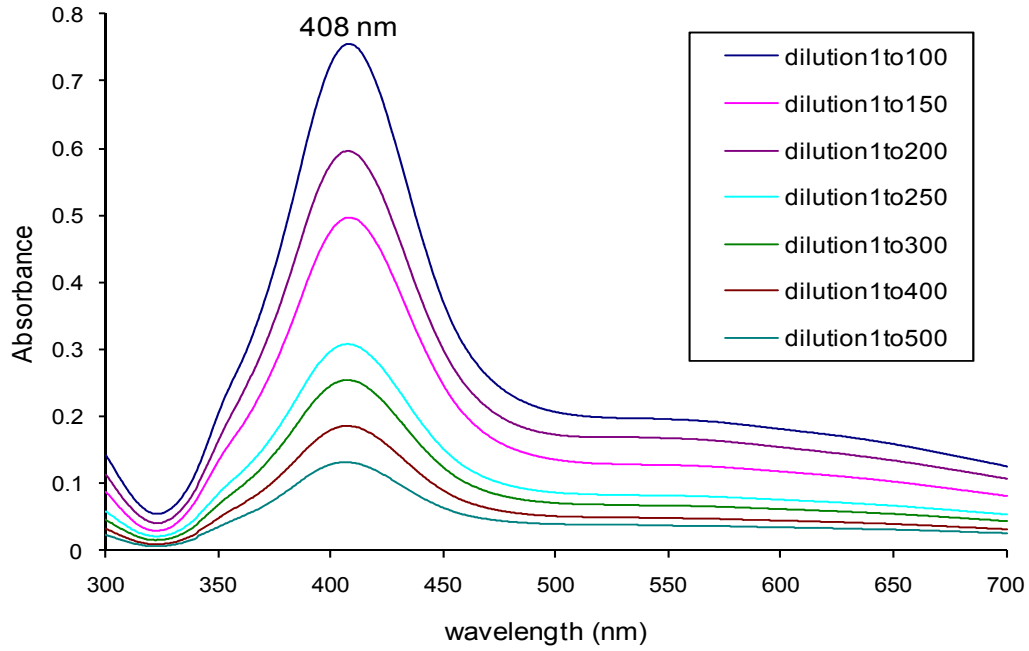

Figure 2.48: Absorbance of diluted silver nanofluids of known concentrations.

The absorbance readings were all taken at a wavelength of 408 nm, which is the wavelength at which the strongest (maximum) absorption occurs. The diluted sample concentrations and corresponding absorbance were used to construct the calibration curve (Figure 2.49). The calibration curve was used to determine the concentration of effluent samples using their absorbance.

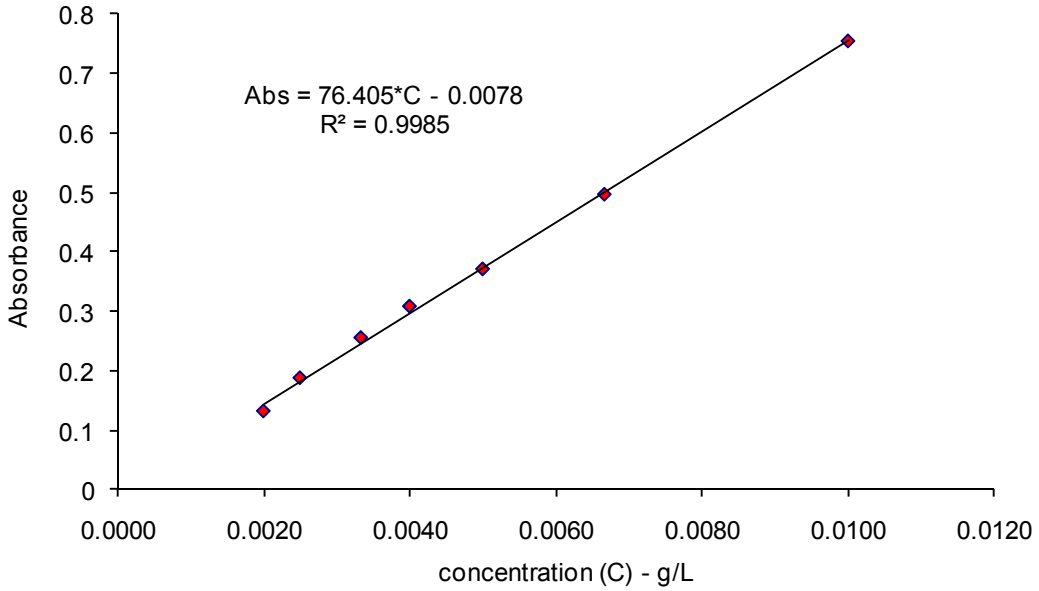

Figure 2.49: Calibration curve of silver nanofluid prepared for injection into Berea sandstone.

2.5.5.2 Silver nanoparticle injection and results

Silver nanoparticles injection was conducted to investigate their flow through the pores of Berea sandstone. The apparatus used was the same as the one used earlier in the hematite nanorice injection into Berea sandstone (Figure 2.35). Nanofluid solution was contained in a pressure vessel downstream of the water pump. The silver nanoparticles were injected with the aid of nitrogen gas. The silver nanoparticles were of an average size of 40 nm in diameter.

Prior to the injection of the nanofluid, the core was preflushed with pure water to displace as much rock fines and debris as possible. About 25% (2 ml of nanofluid) of the pore volume was injected. The silver nanofluid was diluted one part silver to two parts of pure water.

Subsequent to the injection of the nanofluid, a continuous flow of pure water (post injection) was introduced. Specifically, four pore volumes of pure water were injected while the effluent samples were collected. The total time of the experiment was approximately 30 minutes. The injection was at the rate of 1 milliliter per minute at a differential pressure of about 0.425 atm. A total of 12 effluent samples were collected at the rate of 2.5 milliliter per sample. All these samples were analyzed using UV-visible spectrophotometry. Samples from the first and third pore volumes were analyzed using SEM.

The silver nanoparticles were transported through the pore space of the rock and were detected in the effluents. SEM imaging has confirmed the transport of the nanoparticles as shown in Figure 2.50.

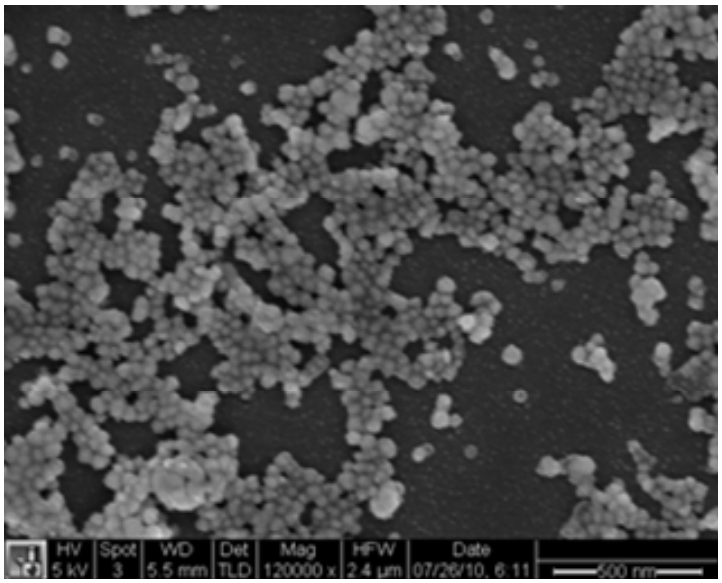

Figure 2.50: SEM image of effluent sample taken from the third post injected pore volume.

The recovery of the silver nanoparticles can be observed visually, as shown in Figure 2.51. Cloudy samples are highly concentrated with silver nanoparticles compared to transparent

samples. It could also be seen visually that the nanoparticles were recovered following the post injection of about 60% of the first pore volume of pure water and produced continuously until the bulk of these particles were displaced through the second pore volume.

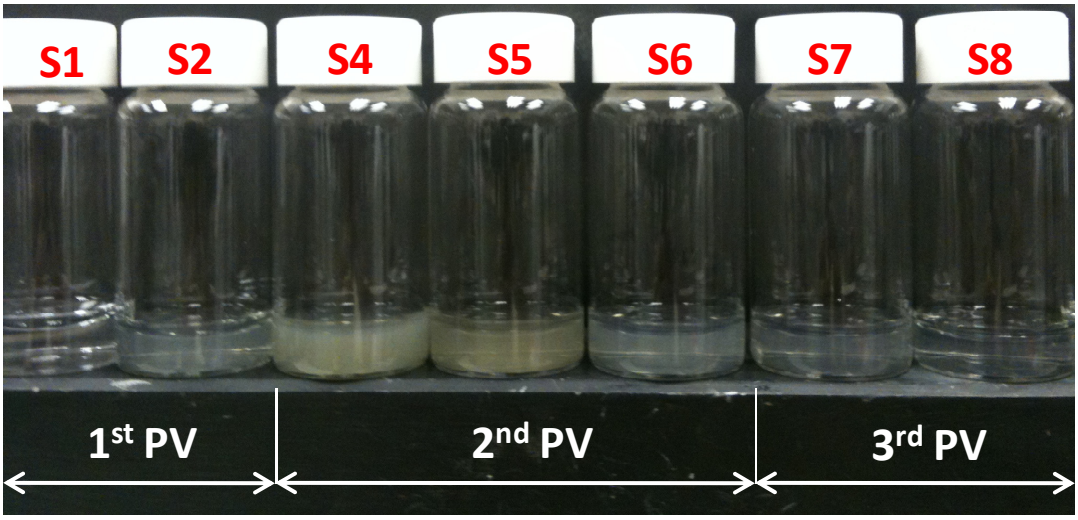

Figure 2.51: Visual characterization of effluent samples for their silver nanoparticles content based on color.

The concentration of the effluent samples was determined by measuring their absorbance using the UV-visible spectrophotometry. The absorption spectra for all effluent samples are depicted in Figure 2.52.

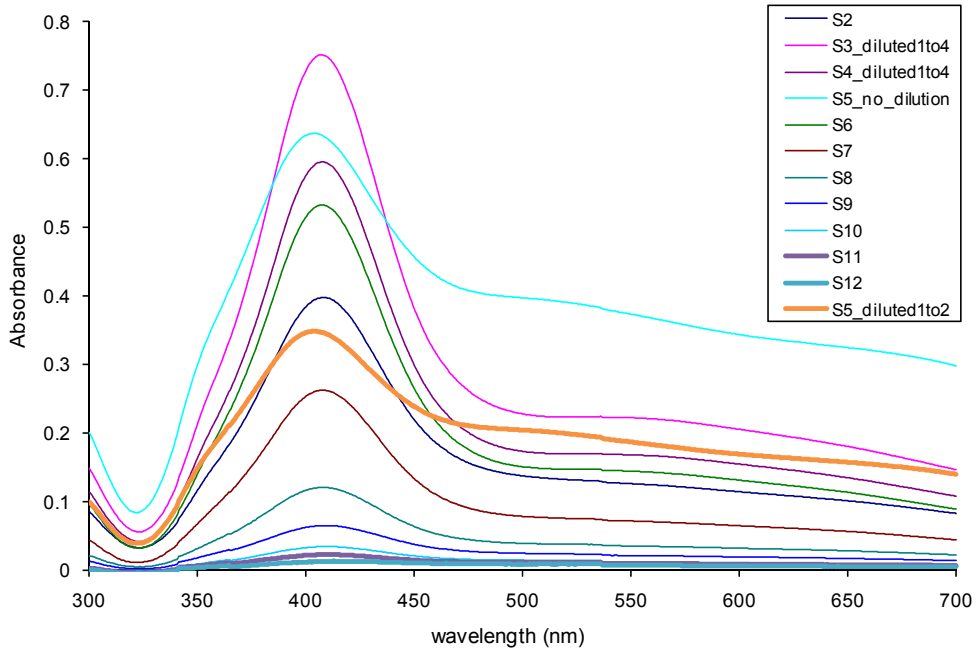

Figure 2.52: Absorbance of all effluent samples collected during silver nanoparticles injection experiment.

Most absorbance spectra have identical signature, except for sample S5 collected during the second post injected pore volume of water. Its spectrum was measured once at its original concentration and again after diluting it with two parts of pure water. Both measurements (spectra) exhibited very similar signature but still different than the rest of the samples (Figure 2.52). Also note that samples (S3 and S4) collected during the second post injected pore volume were highly concentrated and therefore their absorbance spectra could not be measured directly. There were both diluted one part to four parts of pure water. The reported absorbance spectra (Figure 2.52) were for those diluted samples. The calibration curve was then used to obtain the corresponding concentrations for all samples (S2 to S12). Diluted samples (S3 and S4) concentration were calculated back using the following linear relationship.

$$C_1 V_1 = C_2 V_2 \tag{2.16}$$

where C_1 and C_2 are concentrations before and after dilution, respectively. V_1 and V_2 are sample volumes before and after dilutions, respectively.

Following the determination of the effluent samples concentration, the production history curve of the silver nanoparticles was estimated (Figure 2.53).

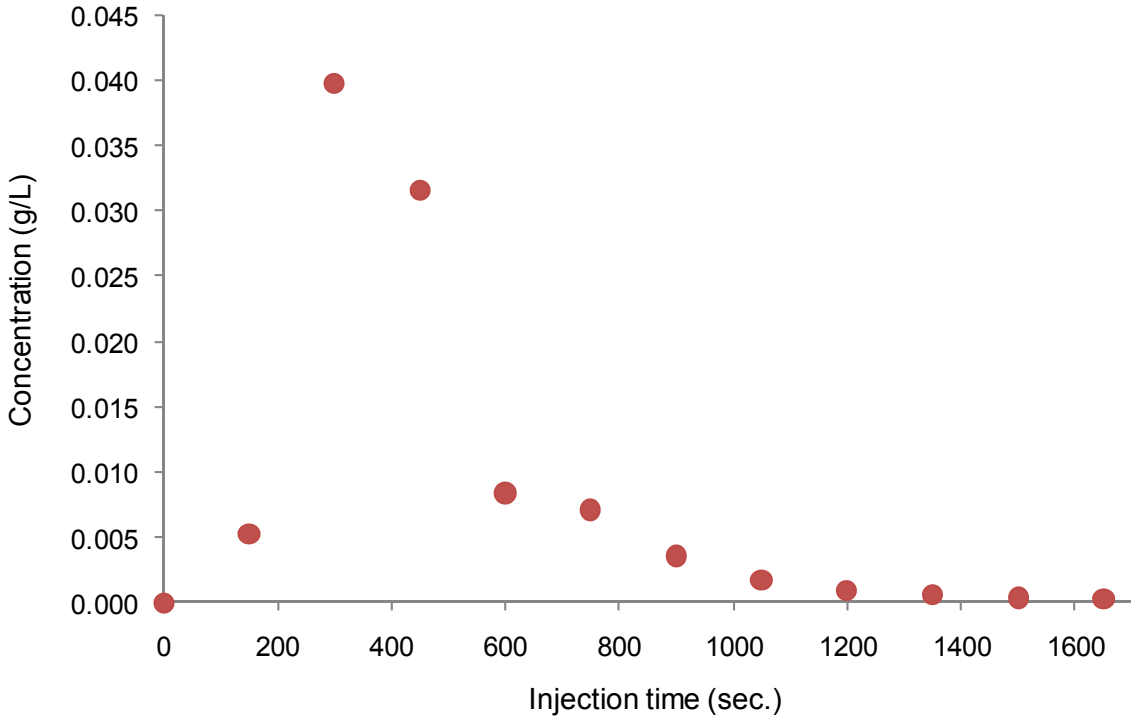

Figure 2.53: Production history (return curve) of silver nanoparticles.

The quantity of nanoparticles recovered can be calculated by integrating the area under the return curve. A rough estimate has indicated that less than 25% of injected nanoparticles were recovered.

2.5.6 Characterization of tin-bismuth alloy nanoparticles

The tin-bismuth alloy nanoparticles were characterized in terms of size and shape using DLS and SEM imaging. It was determined from three consecutive DLS measurements that there was a wide distribution of the particle hydrodynamic diameter, as shown in Figure 2.54.

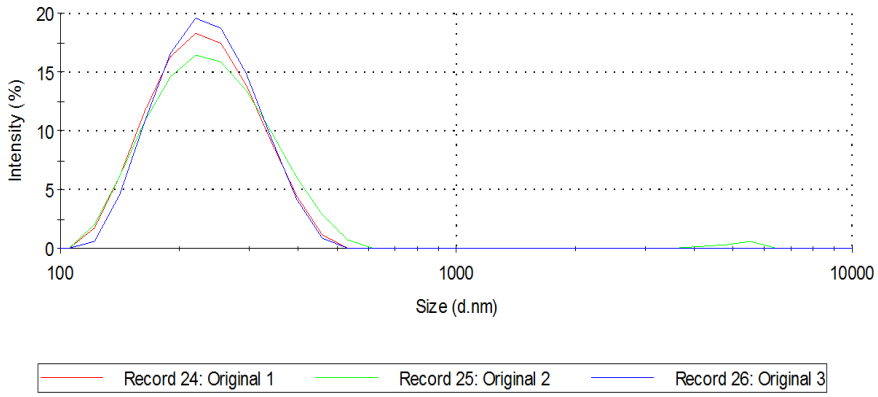

Figure 2.54: Logarithmic particle size distribution based on hydrodynamic diameter for original Sn-Bi nanoparticle sample.

It is believed that the improved washing technique (using a mixture of hexane and acetone instead of ethanol) allowed the particles to be well dispersed in ethanol, which in turn allowed successful DLS measurements. The three measurements are in relatively close agreement, with a standard deviation of about ±2 nm and an average modal value of 235 nm. The hydrodynamic diameter ranged from ~100 nm to ~600 nm, with Run 2 showing a small peak at ~5500 nm. This indicates that there may have been large particles in the sample, either due to aggregation or from the original synthesis. The SEM images of the sample show good agreement with the DLS measurements, as shown in Figures 2.55 and 2.56.

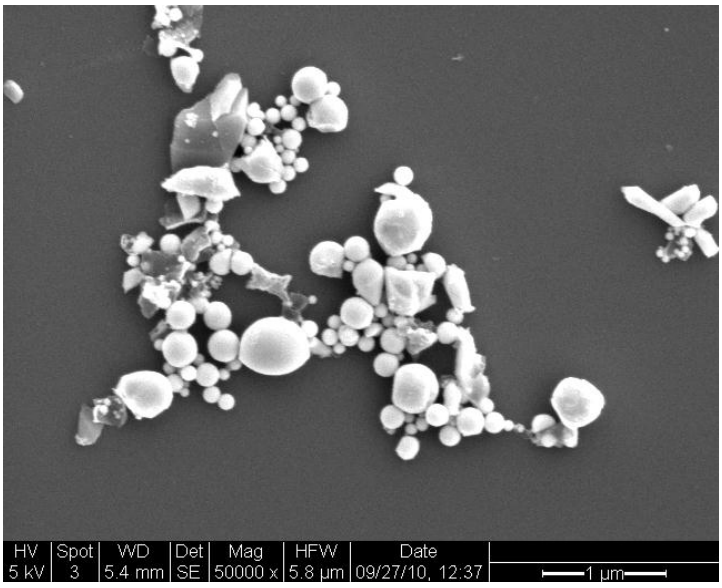

Figure 2.55: SEM image showing the wide range of Sn-Bi nanoparticle sizes.

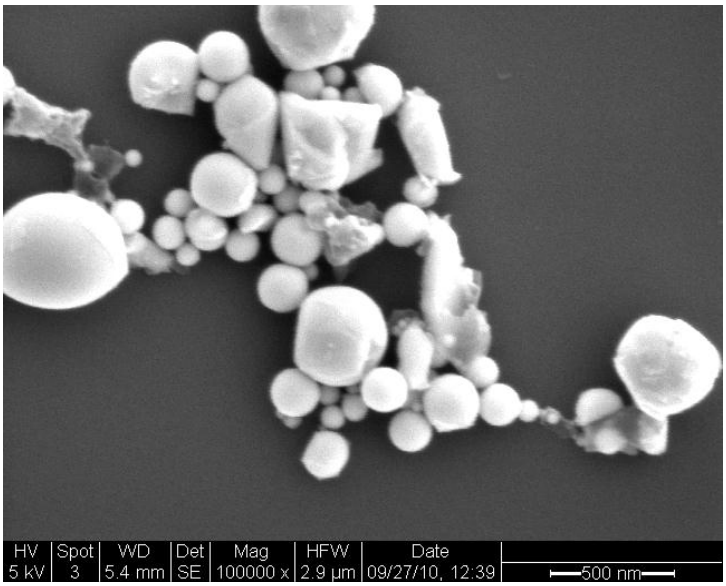

Figure 2.56: SEM image of Sn-Bi nanoparticles showing the same area of the sample at higher magnification.

It is apparent from Figures 2.55 and 2.56 that the "bare" Sn-Bi nanoparticles range from <100 nm to >500 nm. Furthermore, although many of the nanoparticles seem to be spherical as expected, the presence of nonspherical crystalline structures indicates that the sonochemical synthesis did not reach completion. Aggregation on the substrate is observed in both figures, but it is unclear whether this aggregation occurs in solution or upon drying on the substrate. The DLS results suggest that the latter may be the case.

2.5.6.1 Tin-bismuth (Sn-Bi) nanoparticles heating experiment

To begin investigating particle melting and cooling behavior within the temperature range of interest, a sample of the nanofluid (Sn-Bi in mineral oil) from the synthesis described in Section 2.4.2.4 was subjected to a preliminary heating experiment. Although we are ultimately interested in the melting behavior of the Sn-Bi nanoparticles in water, the heating experiments were performed in oil due to the complications associated with the boiling of water at experimental conditions. As shown in the phase diagram Figure 2.22, at the eutectic composition, the Sn-Bi alloy melts at 139°C. In fact, the nanoparticles probably melt at a slightly lower temperature than this due to melting point depression.

The experiment used to heat the sample included a heating mantle connected to a temperature controller with a feedback thermometer as shown in Figure 2.57.

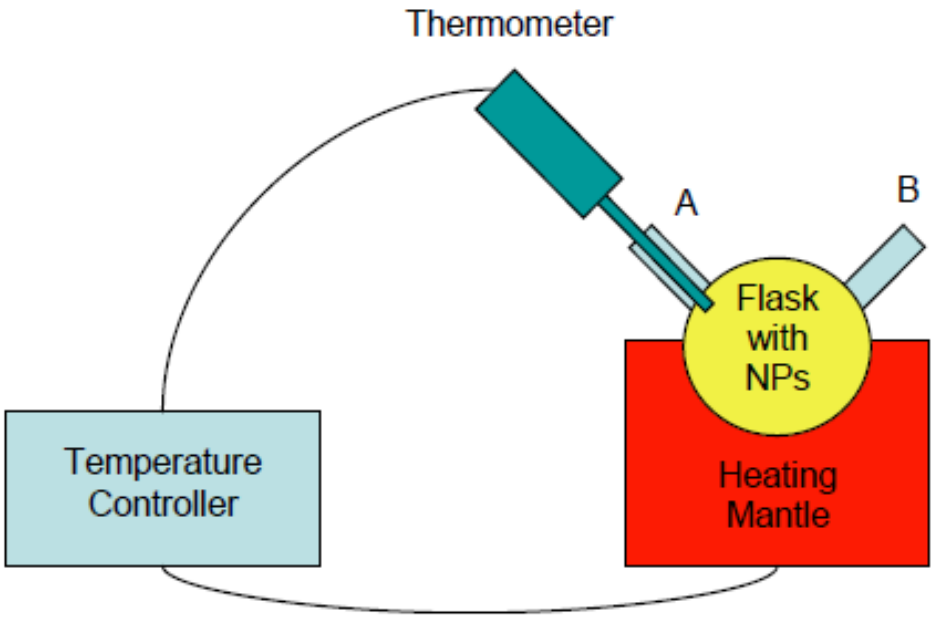

Figure 2.57: Experimental apparatus for Sn-Bi heating experiment

The flask containing the Sn-Bi nanoparticles in oil was placed in the heating mantle, which was connected to the temperature controller. The temperature controller was also connected to a thermometer, the feedback from which affected whether the mantle was heated, cooled, or maintained and the rate at which this was done. The thermometer was positioned in port A.

The sample was heated in steps to the expected melting point of 139°C. The sample was monitored for a color change near the expected melting point, and when none occurred, the sample was heated in steps to 210°C. No color change ever occurred, but the heating was stopped to prevent the mineral oil from burning. Also, it was assumed that melting had probably occurred regardless of the absence of color change. Finally, when the apparatus was at room temperature, the sample was removed from the flask. Then the sample was washed and centrifuged several times with a 1:1 mixture of hexane and acetone, rinsed in a solution of 0.1 M PVP in ethanol, and finally suspended in ethanol. The centrifuge setting was 6000 rpm for 15 minutes each time. This sample was then characterized using DLS and SEM imaging.

The final experiment to begin investigating the melting and cooling behavior of the Sn-Bi nanoparticles had inconclusive results due to the wide particle size distribution of the original sample. The DLS results of the sample subjected to heating are shown in Figure 2.58.

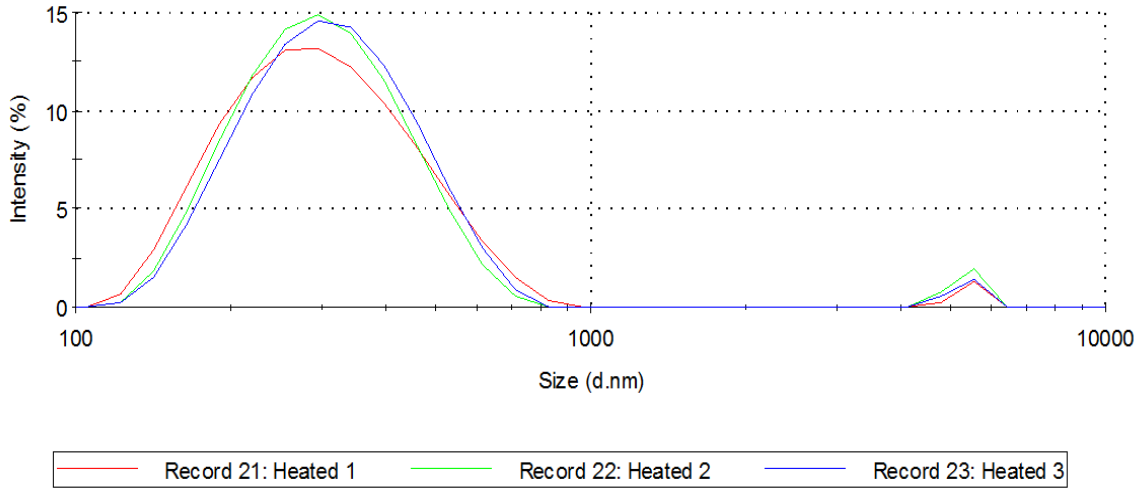

Figure 2.58: Logarithmic particle size distribution based on hydrodynamic diameter for heated Sn-Bi nanoparticle sample.

The three measurements are in relatively close agreement, with a standard deviation of about ±2 nm and an average modal value of 321 nm. The hydrodynamic diameter ranged from ~100 nm to ~1000 nm. Appreciable secondary peaks in the range of ~4100 nm to ~6400 nm are observed for all runs. This indicates that there are large particles in the sample, most likely do to aggregation and fusion of the particles during cooling. Selected particle size distribution curves for comparison of the original and heated samples are shown in Figure 2.59.

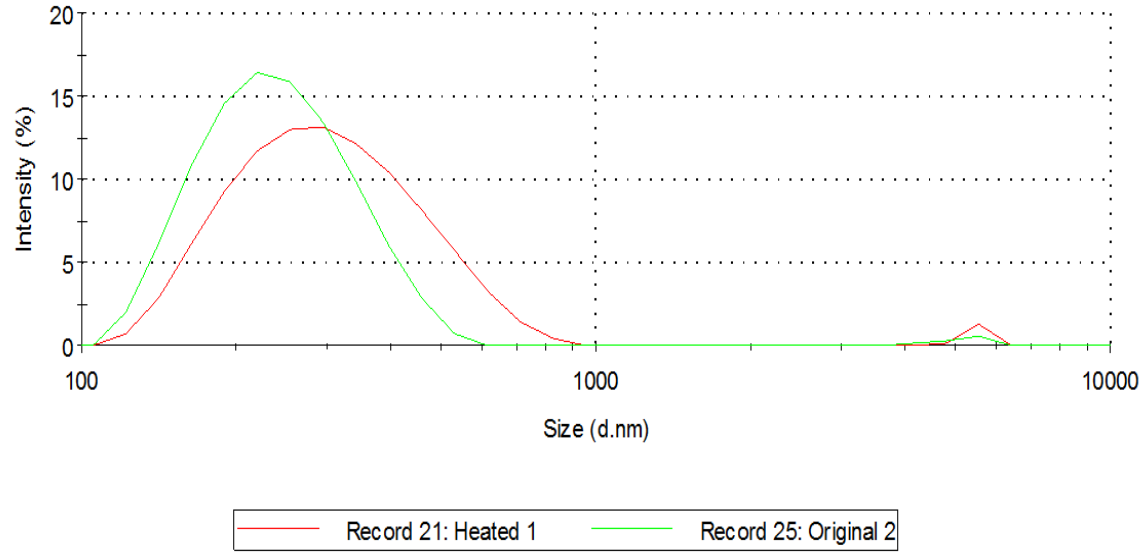

Figure 2.59: Comparison of logarithmic particle size distribution based on hydrodynamic diameter for original and heated Sn-Bi nanoparticle samples.

As shown in the figure, there is an appreciable difference in the particle size distribution upon heating, with a large standard deviation of ±61 nm. The heated sample has a wider distribution and exhibits larger particle sizes. Also, the second secondary peak in the micron scale is noticeably larger, indicating that there are more large aggregates. SEM images of the heated sample are shown in Figures 2.60 and 2.61.

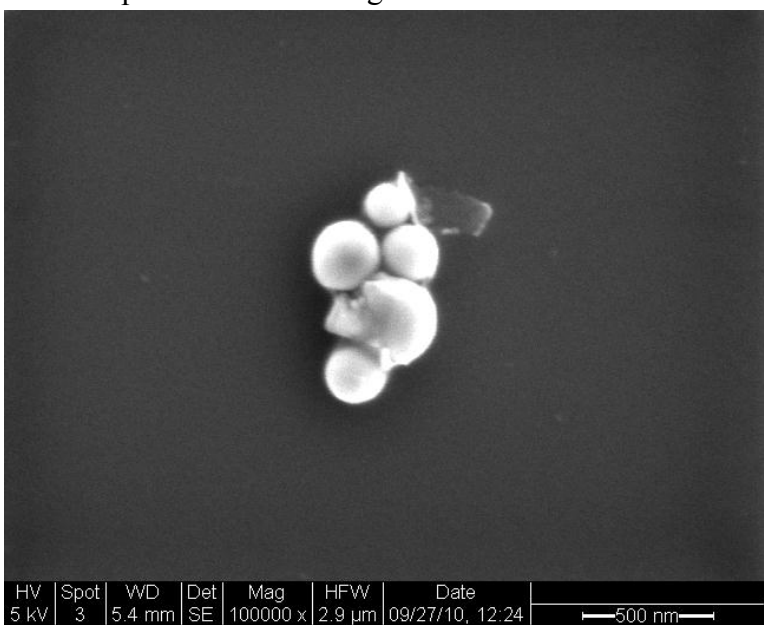

Figure 2.60: SEM image showing heated Sn-Bi nanoparticles.

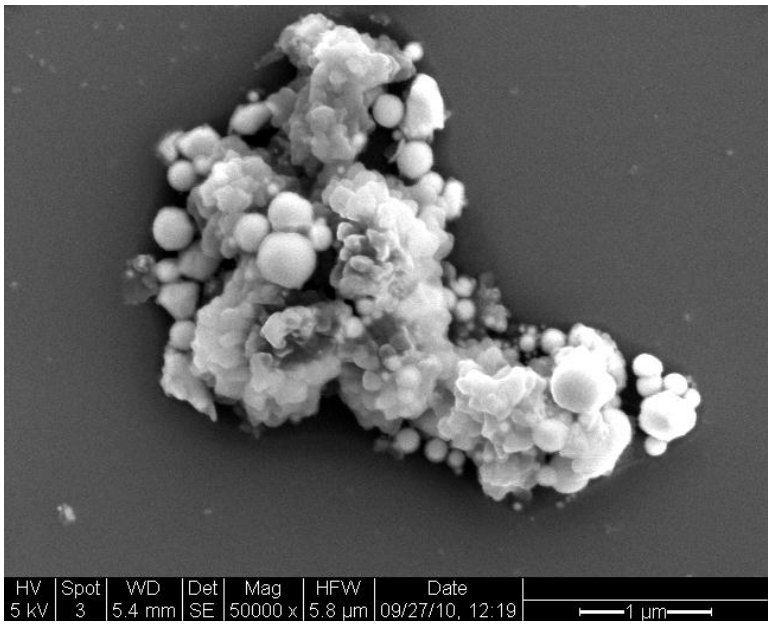

Figure 2.61: SEM image showing large aggregate of heated Sn-Bi nanoparticles.

Fusion of melted particles can be observed in both figures, and the sizes of both particles and large aggregates are within the range suggested by DLS results. While the fusion of melted particles could account for the shift in particle size distribution, it is difficult to

come to any definite conclusions from the SEM results due to the very wide particle size distributions of both the heated and unheated samples.

2.6 FUTURE WORK

The next stage will be to inject pure water into the Berea core at higher flow rate in attempt to displace mobile silver nanoparticles. Also, the core will be backflushed with pure water to try to remobilize nanoparticles that might have been trapped at the inlet. The effluent samples will be characterized using UV-visible spectrophotometry as well as scanning electron microscopy. In addition, the experimental data will be fitted to an appropriate one-dimensional advection-dispersion model. The Sn-Bi synthesis will be repeated at a higher ultrasonic power with the goal of obtaining a more monodisperse and uniform sample, and they will be subject to more investigation, including flow and heating experiments. Finally, more advanced sensitive particles will be synthesized and their transport and recovery will be investigated.

3. FRACTURE CHARACTERIZATION USING RESISTIVITY

This research project is being conducted by Research Assistant Lilja Magnusdottir, Senior Research Engineer Kewen Li and Professor Roland Horne. The objective of this project is to investigate ways to use resistivity to infer fracture properties in geothermal reservoirs.

3.1 SUMMARY

The aim of this part of the project is to use resistivity measurements and modeling to characterize fracture properties in geothermal fields. The resistivity distribution in the field can be estimated by measuring potential differences between various points and the resistivity data can be used to infer fracture properties due to the large contrast in resistivity between water and rock.

In the first part, a two-dimensional model was made to calculate a potential field due to point sources of excitation for a uniform rectangular grid. The model takes into account heterogeneity by solving the potential field for inhomogeneous resistivity. Fractures are modeled as areas with resistivity different from the rock, to investigate the changes in the potential field around them.

In the second part of the project, the model was used to investigate the possibility of using potential difference between only two points in a reservoir to infer at what angle a straight fracture, between the points, was aligned. Various fracture patterns were also examined in order to study the correspondence between potential differences and fracture patterns. In the third quarter, the model was improved to solve the potential field for a nonuniform rectangular grid. The fracture elements could therefore be modeled smaller than the elements for the rest of the reservoir, in order to decrease the total number of elements. The possibility of using conductive fluid to enhance the contrast between fracture and rock resistivity was also explored and the use of conductive fluid with time dependent resistivity measurements. A flow simulation was performed where the distribution of a conductive tracer through a fracture network was observed.

In the fourth quarter, a program that reads the flow simulation output into the resistivity model was made. The changes of the potential field at different time steps were calculated as the tracer transfers through the fractures in the reservoir. Those results have shown that the resistivity model has promising possibilities in fracture characterization.

The main goal of future work is to use the resistivity model and flow simulations with inverse modeling to estimate the dimensions and topology of a fracture network based on the potential differences measured between geothermal wells. Other aspects will be explored as well, for example minimum number of wells needed, different electrode layouts, feasibility of expanding the resistivity model to three dimensions and ways to improve the reliability of this method.

3.2 INTRODUCTION

The designing of optimal production wells in geothermal reservoirs requires knowledge of the resource's connectivity and heat intensity for energy extraction. Drilling and construction of wells are expensive and the energy content from a well depends highly on

the fractures it intersects. Fracture characterization is therefore important to increase the reliability of geothermal wells and thereby the overall productivity of geothermal power plants.

In this project, the goal is to find ways to use Electrical Resistivity Tomography (ERT) to characterize fractures in geothermal reservoirs. ERT is a technique for imaging the resistivity of a subsurface from electrical measurements. Pritchett (2004) concluded based on a theoretical study that hidden geothermal resources can be explored by electrical resistivity surveys since geothermal reservoirs are usually characterized by substantially reduced electrical resistivity relative to their surroundings. Electrical current moving through the reservoir passes mainly through fluid-filled fractures and pore spaces because the rock itself is normally a good insulator. In those surveys, a direct current is sent into the ground through electrodes and the voltage differences between them are recorded. The input current and measured voltage difference give information about the subsurface resistivity, which can then be used to infer fracture locations.

Resistivity measurements have been widely used in the medical industry to image the internal conductivity of the human body, for example to monitor epilepsy, strokes and lung functions as discussed by Holder (2005). In Iceland, electrical resistivity tomography methods have been used to map geothermal reservoirs. Arnarson (2001) describes how different resistivity measurements have been efficiently used there to locate high temperature fields by using electrodes located on the ground's surface. Stacey et al. (2006) investigated the feasibility of using resistivity to measure geothermal core saturation. A direct current pulse was applied through electrodes attached in rings around a sandstone core and it resulted in data that could be used to infer the resistivity distribution and thereby the saturation distribution in the core. It was also concluded by Wang and Horne (2000) that resistivity data has high resolution power in depth direction and is capable of sensing the areal heterogeneity.

In the approach considered in this project, electrodes are placed inside geothermal wells and the resistivity anomalies studied between them to locate fractures and infer their properties by resistivity modeling. Due to the lack of measurement points, i.e. limited number of test wells, we will endeavor to find ways to ease the process of characterizing fractures from limited resistivity data. To enhance the contrast in resistivity between the rock and fracture zones, conductive fluid is injected into the reservoir and future work involves studying further the relationship between fracture patterns and the potential difference between the wells as a conductive tracer flows through the fracture network. It also involves studying the possibility of using inverse modeling to characterize fractures where the output parameters are the potential differences as a function of time while conductive tracer is being injected. This report first describes the resistivity model that has been made to calculate a potential field due to point sources of excitation and how various fracture patterns have been examined in order to study the correspondence between potential differences and fracture patterns. Next, it discusses a flow simulation made to study how a conductive tracer distributes through a simple fracture network and finally how the potential difference between the injection well and the production well is

measured at each time step, while the tracer is injected, to see whether the resulting graph can be used to infer the fracture properties.

3.3 RESISTIVITY MODELING

One of the main problems in resistivity modeling is to solve the Poisson's equation that describes the potential field and to efficiently complete the inversion iteration. That governing equation can be derived from some basic electrical relationships as described by Dey and Morrison (1979). Ohm's Law defines the relationship between current density, J, conductivity of the medium, σ, and the electric field, E, as

$$J = \sigma E \tag{3.1}$$

The stationary electric fields are conservative, so the electric field at a point is equal to the negative gradient of the electric potential there, i.e.

$$E = -\nabla \phi \tag{3.2}$$

where ϕ is the scalar field representing the electric potential at the given point. Hence,

$$J = -\sigma \nabla \phi \tag{3.3}$$

Current density is the movement of charge density, so according to the continuity equation, the divergence of the current density is equal to the rate of change of charge density,

$$\nabla J = \frac{\partial Q(x,y,z)}{\partial t} = q(x,y,z) \tag{3.4}$$

where q is the current density in amp m^{-3}. Combining equations (3.3) and (3.4) gives the following Poisson's equation which describes the potential distribution due to a point source of excitation,

$$\nabla[\sigma \nabla \phi] = -q(x,y,z) \tag{3.5}$$

The conductivity σ is in mhos m^{-1} and the electric potential is in volts. This partial differential equation can then be solved numerically for the resistivity problem.

3.3.1 Finite Difference Equations in Two Dimensions

Finite difference method is used to approximate the solution to the partial differential equation (3.5) using a point-discretization of the subsurface (Mufti, 1976). The computational domain is discretized into $Nx \times Ny$ blocks and the distance between two adjacent points on each block is h in x-direction and l in y-direction, as shown in Figure 3.1.

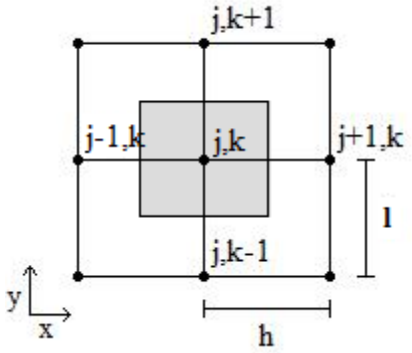

Figure 3.1: Computational domain, discretized into blocks.

Taylor series expansion is used to approximate the derivatives of equation (3.5) about a point (j,k) on the grid,

$$\left.\frac{\partial}{\partial x}\left(\sigma\frac{\partial\phi}{\partial x}\right)\right|_{(j,k)} \approx \frac{\left[\begin{array}{l}\phi(j+1,k)\sigma\left(j+\frac{1}{2},k\right)+\phi(j-1,k)\sigma\left(j-\frac{1}{2},k\right)\\ -\left[\sigma\left(j+\frac{1}{2},k\right)\sigma\left(j-\frac{1}{2},k\right)\right]\phi(j,k)\end{array}\right]}{h^2} \tag{3.6}$$

$$\left.\frac{\partial}{\partial y}\left(\sigma\frac{\partial\phi}{\partial y}\right)\right|_{(j,k)} \approx \frac{\left[\begin{array}{l}\phi(j,k+1)\sigma\left(j,k+\frac{1}{2}\right)+\phi(j,k-1)\sigma\left(j,k-\frac{1}{2}\right)\\ -\left[\sigma\left(j,k+\frac{1}{2}\right)\sigma\left(j,k-\frac{1}{2}\right)\right]\phi(j,k)\end{array}\right]}{l^2} \tag{3.7}$$

The point (j,k) represents the shaded area in Figure 3.1 (area = hl) so the current density due to an electrode at that point is given by,

$$q(j,k)=\frac{I}{hl} \tag{3.8}$$

where I [amp] is the current injected at point (j,k) Combining Equations (3.5)-(3.8) and solving for the electric potential ϕ at point (j,k) gives,

$$\phi(j,k)=\frac{\left[Ihl+\phi(j+1,k)c_1l^2+\phi(j-1,k)c_2l^2+\phi(j,k+1)c_3h^2+\phi(j,k-1)c_4h^2\right]}{\left[c_1+c_2\right]l^2+\left[c_3+c_4\right]h^2} \tag{3.9}$$

The parameters c_i represent the conductivity averaged between two adjacent blocks, i.e.

$$c_1=\frac{2}{\rho(j,k)+\rho(j+1,k)} \tag{3.10}$$

$$c_2=\frac{2}{\rho(j,k)+\rho(j-1,k)} \tag{3.11}$$

$$c_3=\frac{2}{\rho(j,k)+\rho(j,k+1)} \tag{3.12}$$

$$c_4=\frac{2}{\rho(j,k)+\rho(j,k-1)} \tag{3.13}$$

where $\rho(j,k)$ is the resistivity [ohm-m] of the node at grid coordinates j,k.

3.3.2 Iteration method

In order to solve Equation (3.9) numerically and obtain the results for electrical potential ϕ at each point on the grid, the iteration method called Successive Over-Relaxation is used (Spencer and Ware, 2009). At first, a guess is made for $\phi(j,k)$ across the whole grid, for example $\phi(j,k)=$ for all j,k. That guess is then used to calculate the right hand side of Equation (3.9) (Rhs) for each point and the new set of values for $\phi(j,k)$ is calculated using the following iteration scheme,

$$\phi_{n+1}=\omega Rhs+(1-\omega)\phi_n \tag{3.14}$$

The multiplier ω is used to shift the eigenvalues so the iteration converges better than simple relaxation. The number ω is between 1 and 2, and when the computing region is rectangular the following equation can be used to get a reasonable good value for ω,

$$\omega = \frac{2}{1+\sqrt{1-R^2}} \tag{3.15}$$

where

$$R = \frac{\left(\cos\left(\frac{\pi}{Nx}\right)+\cos\left(\frac{\pi}{Ny}\right)\right)}{2} \tag{3.16}$$

The natural Neumann boundary condition is used on the outer boundaries, i.e. $\frac{\partial \phi}{\partial n} = 0$.

3.4 RESULTS

The resistivity model was first tested for a 160 × 160 m field with homogeneous resistivity as 1 Ωm. A current is set equal to 1 A at a point in the upper left corner, and as -1 A at the lower right corner. The potential distribution can be seen in Figure 3.2.

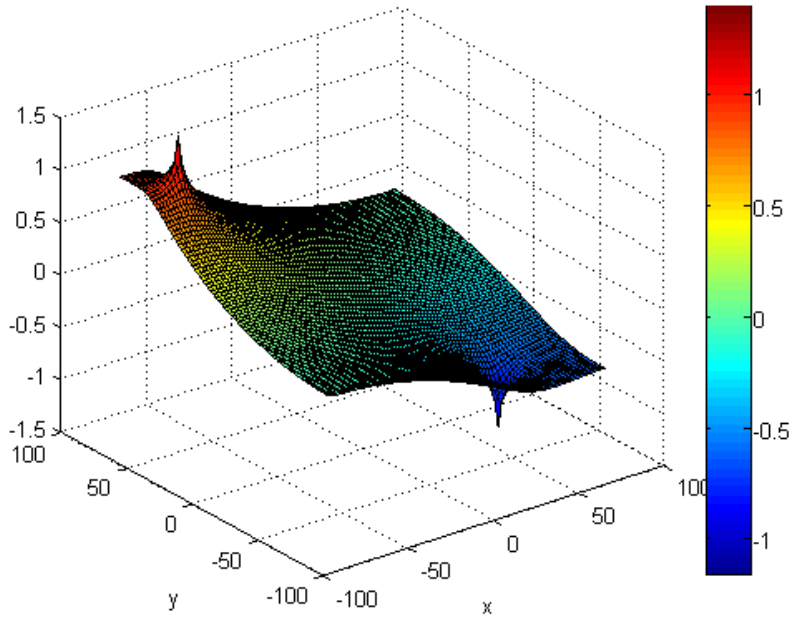

Figure 3.2: Potential distribution [V] for a homogeneous resistivity field.

The model was compared to the Partial Differential Equation (PDE) Toolbox in Matlab, which gives similar results as can be seen by comparing Figures 3.3 and 3.4.

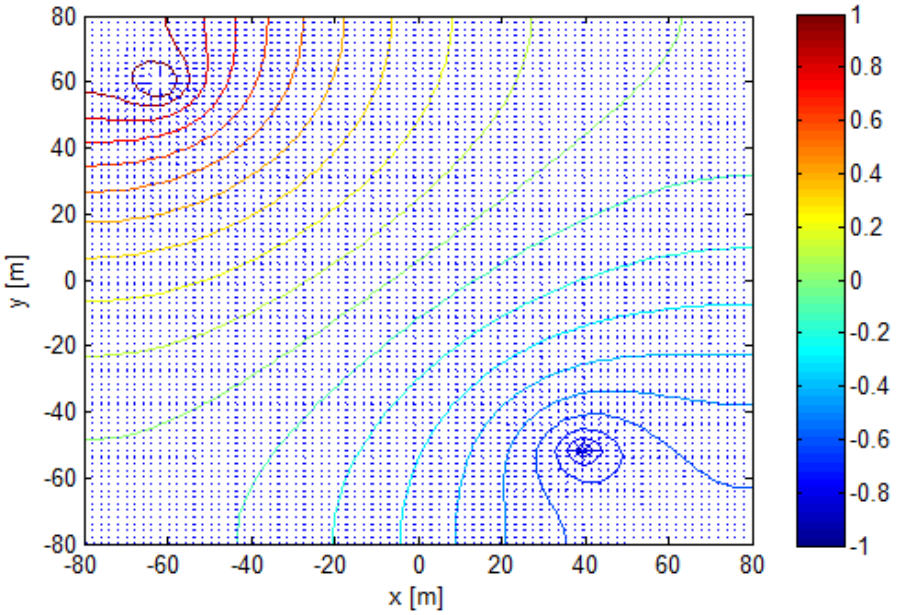

Figure 3.3: Potential distribution [V] for a homogeneous resistivity field, calculated using the program made in this project.

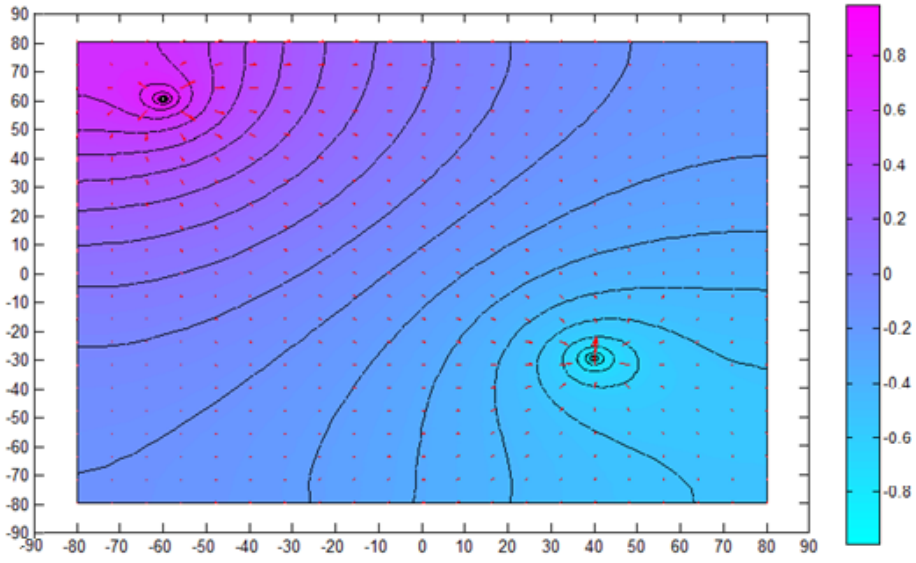

Figure 3.4: Potential distribution for a homogeneous resistivity field, calculated using PDE Toolbox in Matlab.

The Partial Differential Equation Toolbox in Matlab contains tools to preprocess, solve and postprocess partial differential equations in two dimensions (The MathWorks, 2003). However, it does not solve a potential field for inhomogeneous resistivity. In order to use the potential differences to distinguish between the rock and fractures, the model calculating the potential field must be able to take into account heterogeneity, as the program in this project does. Figure 3.5 shows the potential field where the points on a line between the current points have resistivity 10,000 Ωm, while the rest of the field has

resistivity 1 Ωm. The field is 160 × 160 m as before, and a current equal to 1 A is injected in the upper left corner and -1 A in the lower right corner.

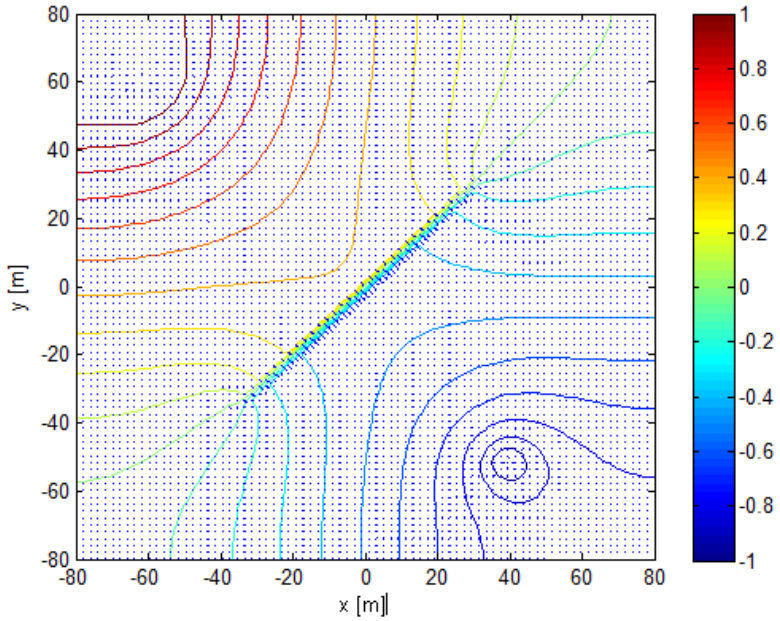

Figure 3.5: Potential distribution for an inhomogeneous resistivity field.

The potential field is higher than for the field with homogeneous resistivity (see Figure 3.3) and the electric field is higher at the high resistivity zone, as expected.

Next, the resistivity model is used to study the possibility of using potential difference between those two wells to infer at what angle a straight fracture between the wells is placed. The field is of the same size and resistivity as before, 160 x 160 m, with resistivity as 1 m, and the fracture is about 60 m with resistivity 10,000 m. Figure 3.6 shows the fracture (grey blocks) modeled with angle θ to the horizontal, and two wells (black blocks) modeled at points (-50,50) and (50,-50).

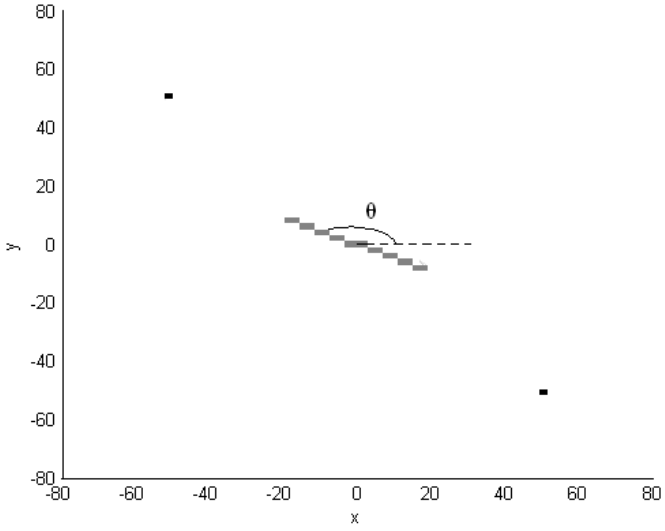

Figure 3.6: Two wells (black blocks) and a fracture (grey blocks) modeled.

A current is set equal to 1 A at the well block in the upper left corner, and as -1 A at the well block in the lower right corner, and the potential distribution is calculated for different angles, θ. The potential difference is lower for a fracture parallel to a straight line between the two wells (i.e. θ = 135°) than for a fracture perpendicular to that line (i.e. θ = 45°), since the fracture is modeled with lower conductivity than the reservoir. Only one, relatively small fracture is modeled so the difference between the two configurations is low, or 2.4112 V for θ = 135° and 2.4182 V for θ = 45°. Figure 3.7 shows the results for various angles.

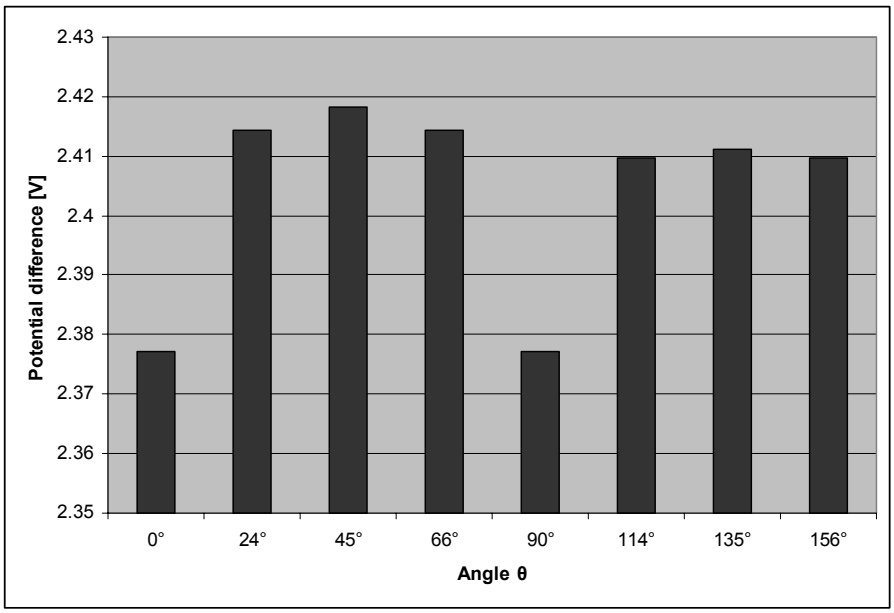

Figure 3.7: Potential difference for various well alignments.

A fracture placed with angle 0° to the horizontal gives the same potential difference as a fracture placed with angle 90°, as expected, since those fractures are symmetric to each other with respect to a straight line between the wells. Knowing the potential difference between those two wells is therefore not enough to distinguish between those two alignments of fractures. The same goes for the other symmetric angles tested, i.e. angles θ = 24° and θ = 66° and angles θ = 114° and θ = 156°.

The resistivity model was next used to calculate the potential difference for a large number of fracture patterns to investigate whether the results could be used to imply a fracture pattern for an unknown field. After defining the number of fractures, the model created horizontal and vertical fractures of random sizes and at random locations. Figure 3.8 shows the results for two different fracture patterns, where the potential difference is calculated between the two wells at points (-50,50) m and (50,-50) m. This time the fractures were assumed to be filled with water so their resistivity was lower (0.001 Ωm) than for the reservoir (1 Ωm).

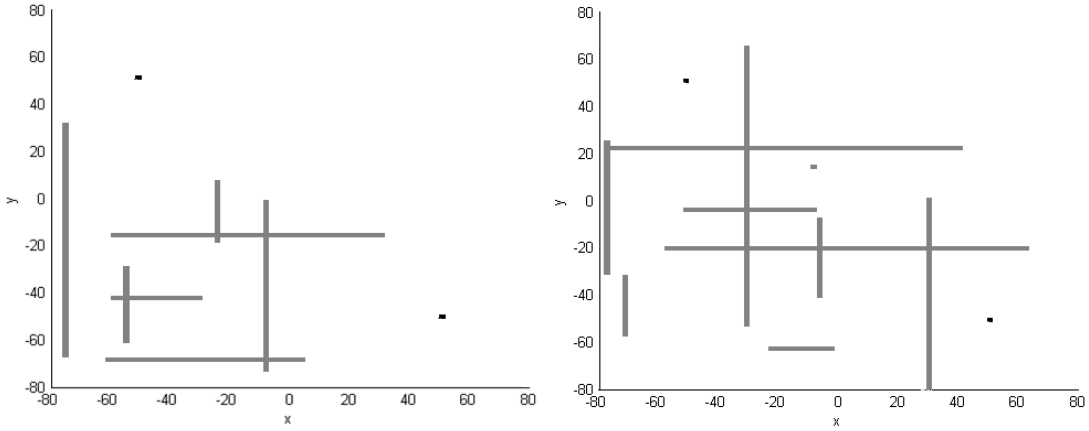

Figure 3.8: Two different fracture patterns modeled (grey blocks).

A current is set equal to 1 A at the well block (black) in the upper left corner of each field, and as -1 A at the well block (black) in the lower right corner, and the potential distribution is calculated. The potential difference between the two wells for the fracture pattern to the left of Figure 3.8 is 2.047 V while the difference is 1.548 V for the pattern to the right. The conductivity of water filled fractures is higher than the conductivity of the rest of the reservoir so higher potential differences between the two wells indicate lower conductivity between them, i.e. fewer fractures. That corresponds to the results for those two fracture patterns; the pattern to the left has higher potential difference and therefore fewer fractures than the one to the right which has lower potential difference. Knowing the potential difference between the wells can therefore help in eliminating a great amount of possible fracture patterns.

However, some different fracture patterns give similar potential difference, as the patterns shown in Figure 3.9. The potential difference between the wells is 1.327 V for the fracture pattern to the left and 1.310 V for the pattern to the right. So the difference between the patterns is small even though the patterns are quite different. It is therefore necessary to investigate other ways to facilitate fracture characterization, though the variation in potential distribution for various patterns can be helpful in suggesting some of the fracture properties.

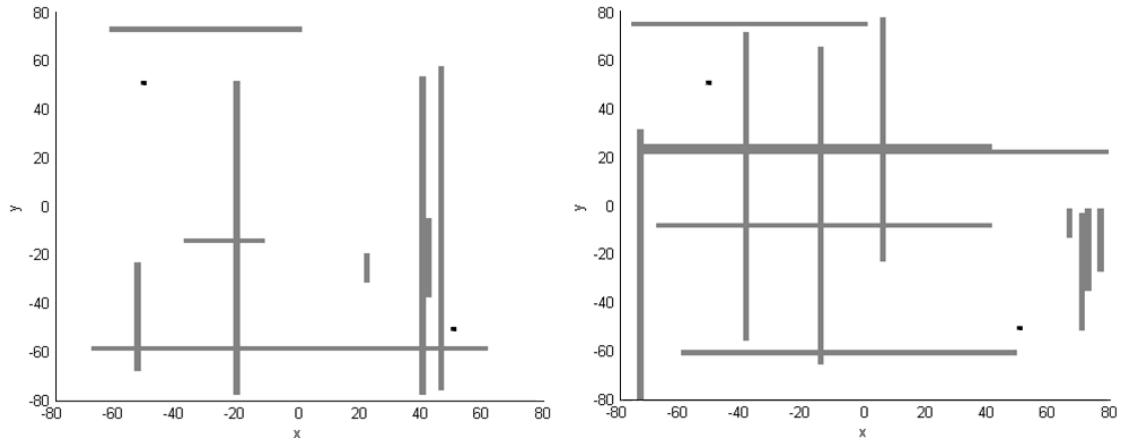

Figure 3.9: Two fracture patterns (grey blocks) that give similar potential difference between two wells (black blocks).

As different fracture patterns can give similar results for the potential difference between the wells, the possibility of using conductive tracer to infer the fracture properties is examined.

A flow simulation is performed using TOUGH2 reservoir simulator to see how a tracer, which increases the conductivity of the fluid, distributes after being injected into the reservoir. The simulation was carried out on a two-dimensional grid with dimensions 1000 x 1000 x 10 m^3. The fracture network can be seen in Figure 3.10, where the green blocks represent the fractures and wells are located at the upper left and lower right corner of the network.

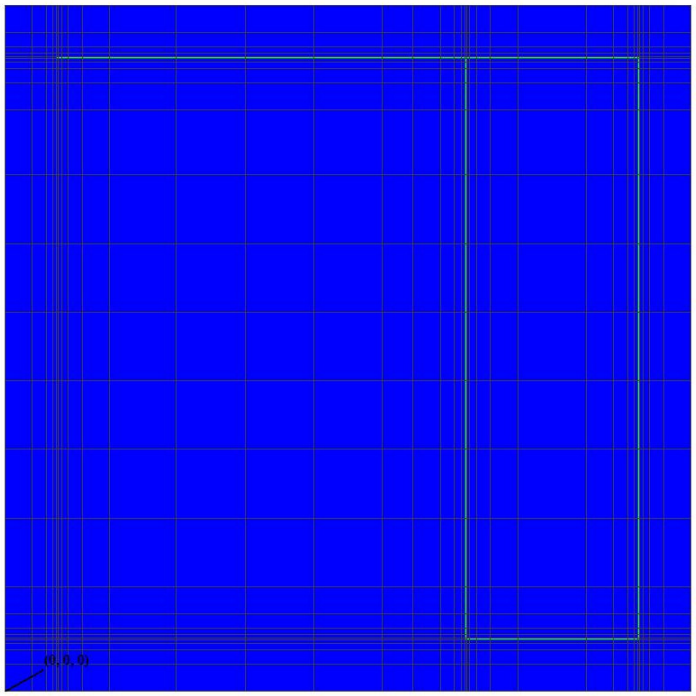

Figure 3.10: Fracture network.

The fracture blocks are given a porosity value of 0.65 and permeability value of $5 \cdot 10^{11}$ md ($5 \cdot 10^{-4}$ m^2) and the rest of the blocks are set to porosity 0.1 and permeability 1 md (10^{-15} m^2). Closed or no-flow boundary conditions are used and one injector at upper left corner, at (76, 924) m, is modeled to inject water at 100 kg/sec with enthalpy 100 kJ/kg, and a tracer at 0.01 kg/s with enthalpy 100 kJ/kg. One production well at lower right corner, at (924, 76) m, is configured to produce at 100 kg/s.

The initial pressure is set to 10.13 MPa (100.13 bar), temperature to 150°C and initial tracer mass fraction is set to 10^{-9} because the simulator could not solve the problem with zero initial tracer mass fraction. Figure 3.11 illustrates how the tracer transfers through the fractures from the injector to the producer. After four days the tracer has distributed through the whole fracture network.

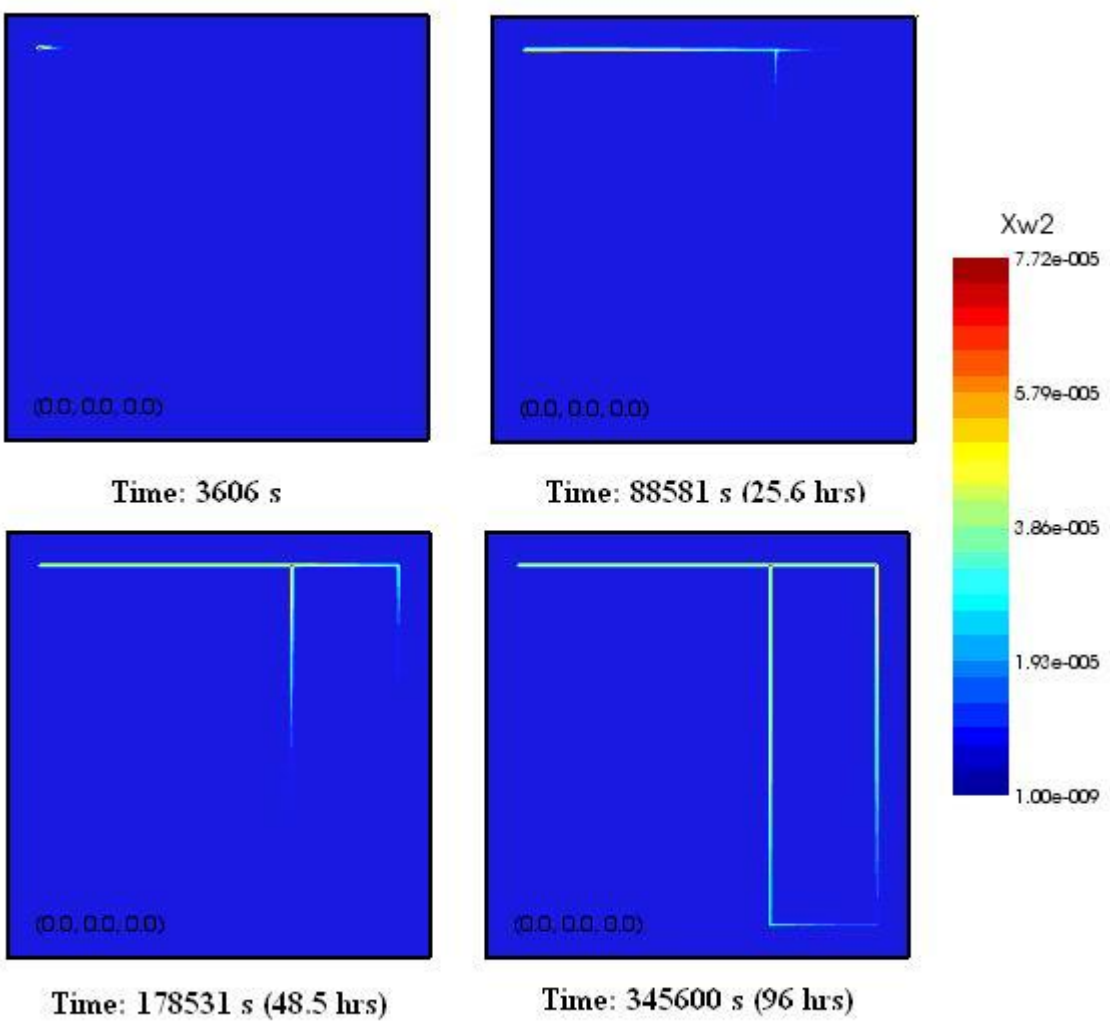

Figure 3.11: Flow simulation's results for tracer concentration.

The resistivity model is modified so it has the same grid as the flow model and a program is made to read the results from the flow simulation and into the resistivity model, so that the right conductivity values can be assigned for the reservoir. The conductivity value of each block depends on the tracer concentration in that block, and it is assumed that the tracer decreases the conductivity, like for example a saline tracer. Table 1 shows how the conductivity values are assigned to different tracer concentration, X_2.

Table 3.1: Tracer concentration and corresponding conductivity values.

Tracer concentration	Conductivity $[(\text{ohm-m})^{-1}]$
$X_2 <= 1 \cdot 10^{-9}$	2.4
$1 \cdot 10^{-9} < X_2 <= 1 \cdot 10^{-8}$	15
$1 \cdot 10^{-8} < X_2 <= 1 \cdot 10^{-7}$	20
$1 \cdot 10^{-7} < X_2 <= 1 \cdot 10^{-6}$	25
$1 \cdot 10^{-6} < X_2 <= 1 \cdot 10^{-5}$	30
$X_2 >= 1 \cdot 10^{-5}$	35

The flow simulation calculates the tracer concentration at 97 time steps and for each step the potential field is calculated using the resistivity model. Figure 3.12 shows the potential field for the four time steps shown in Figure 3.11.

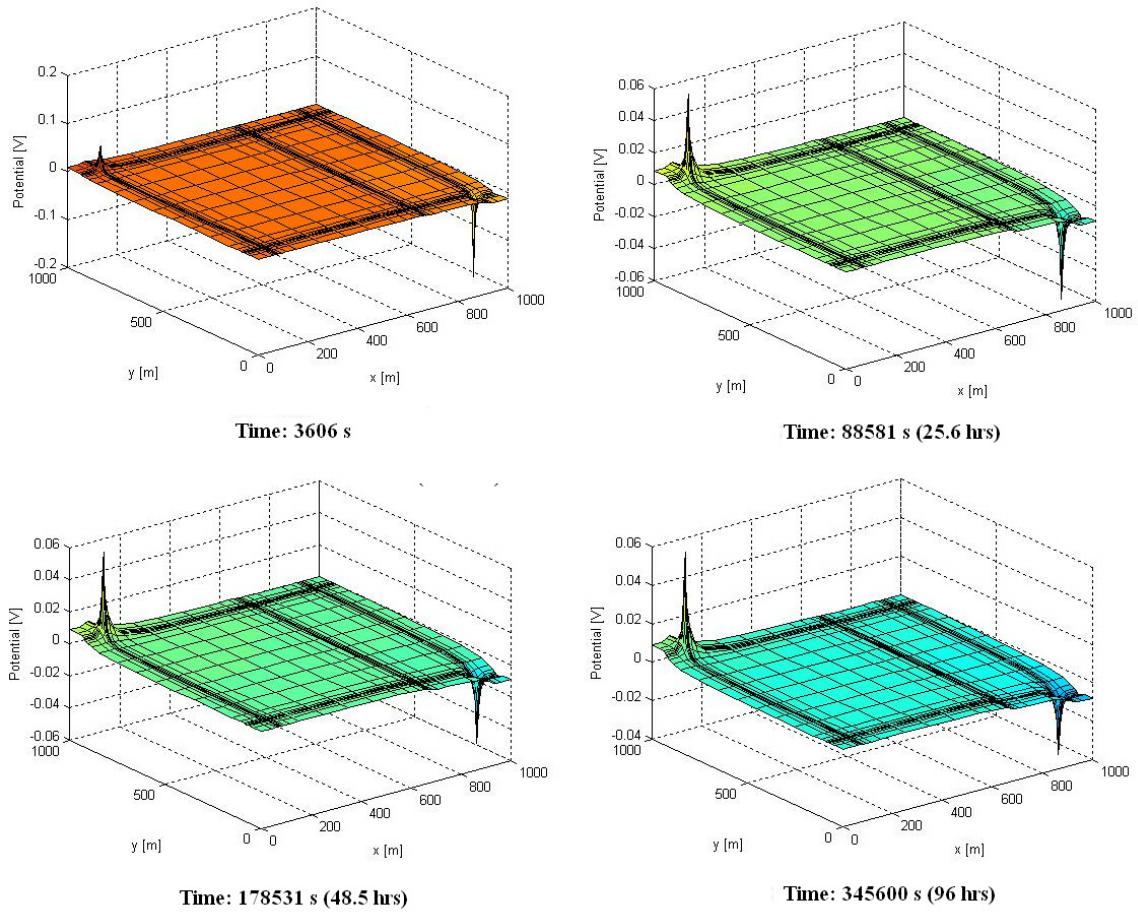

Figure 3.12: Potential field at four different time steps.

First, the tracer has only started flowing through the fracture from the injection well, but not reached the production well or the main fracture between them, so the potential difference is large between the wells. The potential is larger at the production well, because it distributes over a larger area near the injection well due to the tracer. Next, the tracer has gone through the middle fracture, which decreases the potential difference enormously. After that the tracer keeps flowing through the fractures, but the changes in the potential difference are much less.

The potential difference between the injection well and the production well at each time step is shown in Figure 3.13.

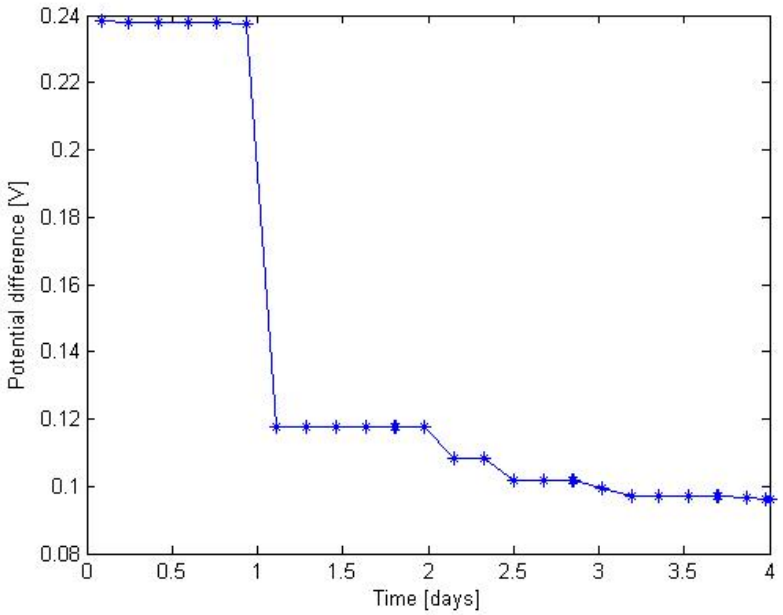

Figure 3.13: Potential difference between two wells at different time steps.

The potential difference between the wells decreases as more of the conductive tracer is injected into the reservoir. The difference changes dramatically between 0.938 days and 1.112 days, but at 1.112 days the whole middle fracture gets a tracer concentration of more than $1 \cdot 10^{-9}$. Another jump can be seen in the potential difference after approximately two days, but at that time the whole fracture network gets a tracer concentration of more than $1 \cdot 10^{-9}$. The graph of the potential differences corresponds in that way to the fracture network, so by measuring the potential differences between two wells while injecting conductive tracer, some information about the network can be gained.

3.5 FUTURE WORK

One of the next steps is to calculate the potential difference, while injecting conductive tracer, for different fracture patterns to study the correspondence between the potential difference and the fracture network. Other future goals are to use inverse modeling to estimate the fracture network from the potential difference measured between the wells. It will first be studied by using many wells at different locations, but then the number of wells will be decreased to see if it is possible to infer the fracture properties using only two wells.

Different electrode layouts will be tested to find the optimum layout that minimizes the number of wells needed. The feasibility of expanding the resistivity model to three dimensions will be explored as well. The focus of this study will also be set on testing the reliability of the resistivity model as well as of the whole inverse modeling process. Ways to improve the reliability of this method will be explored too, for example by studying the possibility of injecting varying tracer concentrations while measuring the potential field. Using an alternating current instead of a direct current when measuring the potential difference is also a topic of interest, to study if it influences the potential field in a way that could facilitate fracture characterization.

4. REFERENCES

Amyx, J. W., Bass, D. M. Jr., and Whiting, R. L. (1960), Petroleum Reservoir Engineering, Physical Properties. McGraw-Hill Book Co.

Arnason, K.: Viðnámsmælingar í Jarðhitarannsóknum á Íslandi, Orkustofnun, Orkuþing (2001).

Bear, J., Dynamics of fluids in porous media, *Dover*, (1972), pp. 1-764.

Bodvarsson, G., and Pruess, K., Thermal effects of reinjection in geothermal reservoirs with major vertical fractures, *Journal of Petroleum Technology*, **36**, (1984), 1567–1578.

Cao, H., Development of techniques for general purpose simulators, Ph.D. Thesis, Stanford University. Stanford, CA, (2002).

Chen, Hongjie, Li, Zhiwei, Wu, Zhishen and Zhang, Zhijun: "A novel route to prepare and characterize Sn-Bi nanoparticles," Journal of Alloys and Compounds. 2005, 394, 282-285.

Connor, Steve. <stconnor1@gmail.com> (2010, March 11). [Personal email].

Den Iseger, P., Numerical transform inversion using Gaussian quadrature. *Probability in the Engineering and Informational Sciences*, **20(01)**, (2005), 1–44.

Dey, A. and Morrison, H.F.: Resistivity Modelling for Arbitararily Shaped Two-Dimensional Structures, Geophysical Prospecting 27, I06-I36, University of California, Berkeley, CA (1979).

Digital image. Phase Diagrams and Computational Thermodynamics. The National Institute of Standards and Technology. Web. 7 July 2010. <http://www.metallurgy.nist.gov/phase/solder/bisn.html>.

Digital image. VC505-750. Sonics and Materials, Inc. Web. 7 July 2010. <http://www.sonics.com/liquid-new-sheet/VC505-750.pdf>.

Gong, B., Effective models of fractured systems, Ph.D Thesis, Stanford University, Stanford, CA, (2007).

Gringarten, A.C., Witherspoon, P.A., and Ohnishi, Y.: Theory of heat extraction from Fractured Hot Dry Rock. *Journal of Geopysical Research*, **80(08)**, (1975), 1120-1124.

Holder, D.S.: Electrical Impedance Tomography: Methods, History and Applications, IOP, UK (2004).

Horne, R., and Rodriguez, F., Dispersion in tracer flow in fractured geothermal systems, *Proceedings of Seventh Workshop on Geothermal Reservoir Engineering*, Stanford University, Stanford, CA, (1983), 103-107.

Horne, R., and Szucs, P., Inferring Well-to-Well Connectivity Using Nonparametric Regression on Well Histories, *Proceedings of Thirty-Second Workshop on Geothermal Reservoir Engineering*, Stanford University, Stanford, CA, (2007).

Juliusson, E. and Horne, R., Study and Simulation of Tracer and Thermal Transport in Fractured Reservoirs, *Thirty-Fifth Workshop on Geothermal Reservoir Engineering,* Stanford University, Stanford, California, (2010).

Kanj, M., Funk, J., and Al-Yousif, Z.: "Nanofluid Coreflood Experiments in the Arab-D," SPE paper 126161, presented at the 2009 SPE Saudi Arabia Technical Symposium and Exhibition held in Saudi Arabia, Alkhobar, May 09-11.

Karimi-Fard, M., Durlofsky, L. and Aziz, K., An Efficient Discrete Fracture Model Applicable for General Purpose Reservoir Simulators, *Proceedings of SPE Reservoir Simulation Symposium*, (2003), 1-11.

Kim, D., Jeong, S. and Moon, J.: " Synthesis of sliver nanoparticles using the polyol process and the influence of precursor injection," Nanotechnology 17 (2006), 4019-4024

Lange, A., Bousian, J. and B. Bourbiaux., Tracer-Test Simulation on Discrete Fracture Network Models for the Characterization of Fractured Reservoirs, *SPE Europec/EAGE Annual Conference,* (2005), 1-10.

Lauwerier, H.A.., The transport of heat in an oil layer caused by the injection of hot fluid, *Applied Scientific Research,* **5**, (1955) 145-150.

Lecoanet, H.F., Bottero, Jean-Yves and Wiesner, M.R. Laboratory Assessment of the Mobility of Nanomaterials in Porous Media. Environ. Sci. Technol. 2004, 38, 5164-5169.

Levard, Clement. <clevard@stanford.edu (2010, July 8)>. [Personal email].

Levitan, M., Deconvolution of multiwell test data. In *SPE Annual Technical Conference and Exhibition,* (2006), 24-27.

Lovekin, J. and Horne, R., Optimization of injection scheduling in geothermal fields, Conference, *Proceedings of the Geothermal Program Review VII*, (1989), 45-52.

Lu, Yu, Yin, Yadong, Mayers, Brian T., and Xia, Younan: "Modifying the Surface Properties of Superparamagnetic Iron Oxide Nanoparticles through a Sol-Gel Approach," Nano Letters. 2002, 2, 182-186.

Mufti, I.R.: Finite-Difference Resistivity Modeling for Arbitrarily Shaped Two-Dimensional Structures, *Geophysics*, **41**, (1976), 62-78.

Ozaki, M., Kratohvil, S., Matijevic, E. (1984), J. Colloid Interface Sci., 102, 146-151.

Poulton, S., Raiswell, R., 2005. Chemical and physical characteristics of iron oxides in riverine and glacial meltwater sediments. Chem. Geol. 218, 203–221.

Pritchett, J.W.: Finding Hidden Geothermal Resources in the Basin and Range Using Electrical Survey Techniques. A Computational Feasibility Study (2004).

Schroeter, T. v., and Gringarten, A., Superposition Principle and Reciprocity for Pressure-Rate Deconvolution of Data From Interfering Wells. *SPE Annual Technical Conference*, (2007).

Shewchuk, J., Triangle: Engineering a 2D quality mesh generator and Delaunay triangulator, *Lecture Notes in Computer Science*, **1148**, (1996), 203–222.

Spencer, R.L. and Ware, M.: Computational Physics 430, Partial Differential Equations, Department of Physics and Astronomy, Brigham Young University (2009).

Stacey, R.W., Li, K. and Horne, R.N.: Electrical Impedance Tomography (EIT) Method for Saturation Determination, *Proceedings*, 31st Workshop on Geothermal Reservoir Engineering, Stanford University, Stanford, CA (2006).

Stehfest, H., Numerical inversion of Laplace transforms. *Communications of the ACM*, **13(1)**, (1970), 47-49.

Sullera, M., and Horne, R., Inferring injection returns from chloride monitoring data, *Geothermics*, **30**, (2001), 591–616.

Suzuki, S., Caumon, G., and Caers J., Dynamic data integration for structural modeling: model screening approach using a distance-based model parameterization. *Computational Geosciences,* **12,** (2008) 105-119..

Suzuki, S., and Caers J., A Distance-based Prior Model Parameterization for Constraining Solutions of Spatial Inverse Problems, *Mathematical Geosciences*, **40**, (2008), 445-469.

Takahashi, H., Watanabe, K., and Hashida, T., Future target for geothermal development - Fractal fracture mechanics and its application to conceptual HDR reservoir design, *Proceedings of Twentieth Workshop on Geothermal Reservoir Engineering*, Stanford University, Stanford, CA, (1995) 167-174.

The MathWorks: Partial Differential Equation Toolbox 1, The MathWorks^{TM}, Inc. (2003).

Tipping, E., 1981. The adsorption of aquatic humic substances by iron oxides. Geochim. Cosmochim. Acta 45, 191–199.

Tipping, E., Cooke, D., 1982. The effects of adsorbed humic substances on the surface charge of goethite (a-FeOOH) in reshwaters. Geochim. Cosmochim. Acta 46, 75–80.

Urbino, E. G., and Horne, R., Optimizing reinjection strategy at Palinpinon, Philippines, based on chloride data, *Proceedings of Sixteenth Workshop on Geothermal Reservoir Engineering*, Stanford University, Stanford, CA, (1991).

Voskov, D., Description of the Thermal GPRS, Technical Report, Department of Energy Resources Engineering, Stanford University, (2006).

Wang, P. and Horne, R.N.: Integrating Resistivity Data with Production Data for Improved Reservoir Modelling, SPE 59425, SPE Asia Pacific Conference, Yokohama, Japan (2000).

Wang, Hui, et al. (2006), "Nanorice: A Hybrid Plasmonic Nanostructure," Nano Letters, 6.4, 827-32.

Watanabe, K., and Takahashi, H., Fractal geometry characterization of geothermal reservoir fracture networks. *Journal of Geophysical Research-Solid Earth*, **100(B1)**, (1995).

Wittung, P., Kajanus, J., Kubista, M., and Malmström, Bo G. (1994). "Absorption flattening in the optical spectra of liposome-entrapped substances," FEBS Letter 352, 37-40.

Wu, Y., Numerical simulation of nonisothermal multiphase tracer transport in heterogeneous fractured porous media, *Advances in Water Resources*, **23**, (2000), 699-723.

Wu, Y. and Forsyth, P.A., Efficient Schemes for Reducing Numerical Dispersion in Modeling Multiphase Transport through Heterogeneous Geological Media, *Vadose Zone Journal*, **7**, (2008), 340-349.